Fabrication of Polymer–Metal Nanohybrids

—

Routes Towards Functional Materials

Dissertation

zur Erlangung des mathematisch–naturwissenschaftlichen Doktorgrades

"Doctor rerum naturalium"

der Georg-August-Universität Göttingen

im Promotionsstudiengang Chemie

der Georg-August-University School of Science (GAUSS)

vorgelegt von

Darius Rohleder

aus Bremerhaven

Göttingen, 2021

Betreuungsausschuss

Prof. Dr. Philipp Vana, MBA	Institut für Physikalische Chemie Georg-August Universität Göttingen
Prof. Dr. Alec Wodtke	Institut für Physikalische Chemie Georg-August Universität Göttingen
Dr. Florian Ehlers	Institut für Physikalische Chemie Georg-August Universität Göttingen

Prüfungskommission

Referent

Prof. Dr. Philipp Vana, MBA	Institut für Physikalische Chemie Georg-August Universität Göttingen

Co-Referent

Prof. Dr. Alec Wodtke	Institut für Physikalische Chemie Georg-August Universität Göttingen

Weitere Mitglieder

Prof. Dr. Michael Buback	Institut für Physikalische Chemie Georg-August Universität Göttingen
Prof. Dr. Burkhard Geil	Institut für Physikalische Chemie Georg-August Universität Göttingen
Prof. Dr. Dietmar Stalke	Institut für Anorganische Chemie Georg-August Universität Göttingen
Prof. Dr. Thomas Zeuch	Institut für Physikalische Chemie Georg-August Universität Göttingen

Tag der mündlichen Prüfung: 07. Oktober 2021

Die hier dargelegte Arbeit basiert auf der Forschung, die in der Arbeitsgruppe für Makromolekulare Chemie aus dem Institut für Physikalische Chemie an der Georg-August Universität zu Göttingen durchgeführt wurde.

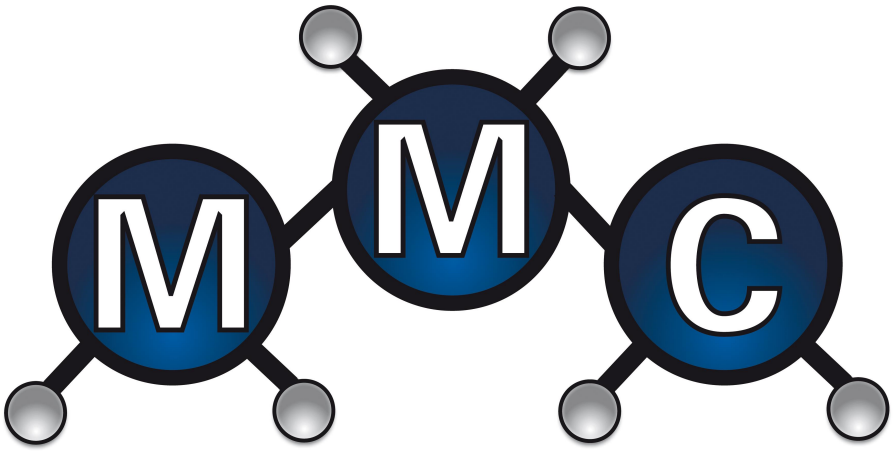

Tag der Abgabe: 31. August 2021

Abstract

Within this thesis various nanohybrid systems constructed from metal nanocrystal cores and polymer shells were specifically tailored towards distinct practical applications.

The first part of this work addresses the straightforward design of a recyclable palladium-core–silica-shell nanocatalyst applied in Heck-reactions. Therefore, a mesoporous silica (*m*Si) shell was tailored onto palladium nanocubes (PdNCubes) in a single-step coating approach. Further functionalization of the porous silica platform *via* polyethylene glycol (PEG)-silanes is presented. This hierarchal strategy offers an excellent balance between nanohybrid stability and sufficient permeability for small organic molecules. To ensure reusability not only of the nanocatalyst but also of the solvent, unfunctionalized PEG was used as reaction medium. The overall process – design, catalysis and purification – is characterized by its simplicity and sustainability accompanied by a great recycling potential and ultra high yields in C–C-coupling reactions.

Palladium nanocubes were further applied in seed-mediated growth processes to obtain larger nanocubes by tuning the seed-to-feed ratio. The variously sized PdNCubes were coated with poly(*N*-isopropyl acrylamide) (poly(NIPAM)) fabricated *via* reversible addition–fragmentation chain transfer (RAFT) polymerization. The inherently formed trithiocarbonate group of the RAFT-polymer served as anchor to immobilize the polymer onto the surface. Thus, prolonged stability and improved processability of palladium nanocubes compared to their cetyltrimethylammoniumbromide-capped (CTAB) counterpart were achieved. These nanohybrids were provided to the *Pundt*-group at the Karlsruher Institute of Technology (KIT) for investigations regarding its size dependent properties in hydrogen storage applications.

Gold nanorods (AuNRs) were coated with linear and 3-arm star RAFT-polymers

with tunable chain lengths constructed from NIPAM building blocks. AuNR nanohybrids self-assembled into 2D nanoarrays by a straightforward drop-casting approach onto an amorphous carbon film observed *via* transmission electron microscopy (TEM). Here, interparticle distances could be tuned over a wide range by altering the average molecular weight of the grafted polymer. Dynamic light scattering (DLS) experiments indicated that the rotational diffusion of gold nanorods may be a good relative measure regarding the size of polymer-grafted nanorods. AuNRs functionalized with 3-arm star RAFT-polymers were further decorated with spherical gold nanoparticles by taking advantage of free anchor groups on the outside of the polymer shell which were not immobilized on the AuNR planet within the first step. Tailorable planet–satellite nanostructures were fabricated in this hierarchal self-assembly approach while spacings between planet and satellites were tuned by different polymer chain lengths. Thus, optical properties in solution were altered, attributed to a plasmonic coupling between the AuNR core and the AuNPs offering potential applications for biological sensing or surface-enhanced Raman spectroscopy (SERS).

At last, AuNRs were decorated with thermoresponsive copolymers constructed from *N*-isopropyl acrylamide and acrylamide (AAM) building blocks. Copolymers of tailored architecture and chain length were prepared *via* RAFT-polymerization using either a monofunctional or 3-arm star RAFT-agent and immobilized on gold nanorods over the trithiocarbonate groups. Two-dimensional arrays of the self-assembled core–shell nanostructures were fabricated by drop-casting showing tunable interparticle spacings in TEM. Nanohybrids dispersed in pure water showed a continuous shrinkage of the polymer shell along an increasing temperature due to a lost of bound water molecules. In a simulated blood fluid, the discrete lower critical solution temperature (LCST) of the nanohybrids could be modified over a significant temperature range around body temperature by adjusting the copolymer composition, the architecture, and/or the size of the polymer. The intrinsic photothermal properties of the gold nanorods were utilized to trigger particle aggregation by irradiation at 808 nm in the optical window of human tissues. Thus, a new nanohybrid system with remotely controllable aggregation *via* an external NIR-light stimulus for nanomedical applications was developed.

Contents

1 Preface

Thousands of years ago, mankind has already been fascinated by overly powerful creatures which led to the imagination of myths and legends about fictive hybrids such as centaurs, griffins, the sphinx or pegasos.[1,2] The belief prevailed that by combining attributes of at least two species, the limitations of each individual alone can be overcome. Interestingly, the fascination and desire to create particularly versatile, strong or efficient systems has not changed over all these years. Nowadays, hybrids have become reality in various kinds of fields like economy,[3] politics,[4] automotives[5] and science.[6]
In this context, the question arose whether the combination of polymers and particles may lead to functional, high-performance hybrid materials, even though each component individually is considered as an environmental villain among the wider society of the 21st century. This prejudice may be caused by the continuously increasing accumulation of plastics within flora and fauna and its low recycling ratio. In 2018, less than 10 percent of the 400 million tons of plastic production originated from recycled or bio-based sources.[7–9] Additionally, the growing consumption of fossil-based resources not only led to higher CO_2 emissions but also to greater outputs of fine particulates with drastic consequences regarding humans' and animals' health.[10,11]
Within the last decade, the *Vana*-group presented outstanding science in the world of nanocomposites. Various metal nanocrystals from gold,[12–18] silver[19,20] and palladium[21] as well as silica nanoparticles[22] could be functionalized with tailored macromolecules. In this context, their self-assembly into 2D nanostructered surfaces, 3D superstructures and planet−satellite structures was studied intensively. Based on these previous works, the aim of this thesis was to create routes towards functional hybrid materials constructed from polymer and metal nanoparticle building blocks and to demonstrate their outstanding potential for specific applications. Therefore, smart choices of suitable particles and polymers for the respective purpose were inevitable to transform these inherent villains to useful and practical hybrids.

2 Theoretical Background

Within this chapter, the key theoretics behind nanohybrid materials used in this thesis shall be highlighted. Therefore, background insights into the **Fabrication and Characteristics of Nanomaterials** such as metal nanocrystals (NC) and mesoporous silica (*m*Si) is given. The reversible addition–fragmentation chain transfer polymerization (RAFT) in combination with different grafting approaches and the polymer poly(*N*-isopropyl acrylamide) (poly(NIPAM)) play central roles regarding the **Synthesis of Tailored Polymers** and are thus addressed in this chapter, as well.

2.1 Fabrication and Characteristics of Nanomaterials

Opposed to their bulk counterpart nanocrystals are characterized by distinct optical, electronic, physical and catalytic properties caused by their size in the nanometer scale.[23–27] Their features are generally determined by geometry, size and environment.[25,28–30] It is obvious that high effort has been put in numerous fabrication processes to synthesize nanocrystals of different topologies such as spheres, octahedra, cubes, tetrahedra, etc. which may lead to totally new properties.[31–36] In nanoscience techniques are generally categorized into two different fields: the top-down and the bottom-up approach.[37]

2.1.1 General Fabrication Approaches

The top-down approach is based on reduction of bulk material to nanoscale structures, similar to a sculpture being modeled from a gigantic marble stone. Depending on the material needed various techniques can be applied such as optical-, electron- or ion beam, nanoimprint- or block-copolymer-lithography.[37–39] These methods exhibit a very reproducible and way to obtain

nanoscale patterns. However, top-down experiments require special technical equipment and conditions (e.g. laser, electron- or ion-beams, high vacuum) while throughput is very limited.[38]
In the bottom-up approach, metal salts or other molecular precursors are used to fabricate nanoparticles in either liquid- or gas-phase syntheses.[37] Within wet-chemistry methods tunable dimensions and geometries are accessible by adjustment of the reaction conditions. Various parameters play crucial roles in the NC fabrication including concentration or choice of surfactant and reductant as well as temperature and solvent.[31–34,40–43]

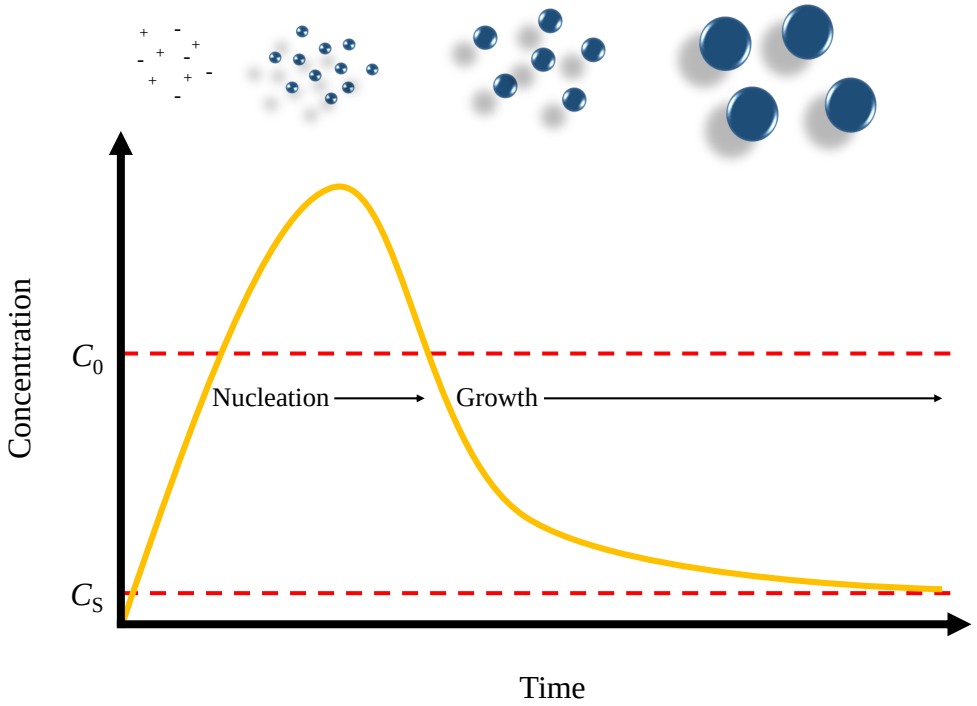

Scheme 2.1: Idealized model of the nucleation–growth-mechanism in nanocrystal synthesis proposed by *LaMer* and *Dinegar*.[44]

The basic understanding of the NC formation mechanism in solution was given by *LaMer* and *Dinegar* called the nucleation–growth-mechanism.[44] The idealized model of the NC-concentration along the reaction time is shown in Scheme 2.1. Here, a metal salt is reduced and nucleation occurs very quickly which leads to an exceedence of the so called saturation concentration C_0.

The formed NCs are rather small and thus possess an elevated surface energy. Consequently, a stage of enhanced growth appears (dictated by the salt-to-NC diffusion) which results in a decrease of the concentration below the nucleation level.[45]
For particular small NCs the surface free enthalpy plays a crucial role in the overall nucleus formation enthalpy. The contrary trends of surface reduction *versus* nucleation results in a critical radius r^* where the overall free enthalpy reaches a maximum. Hence, larger particles are formed at the cost of smaller NCs to reduce the surface free energy.[44,45] This diffusional controlled process is generally known as *Ostwald*-ripening which leads to the saturation concentration C_S of the NCs at the end of the formation process.[46] To yield monodisperse NCs a high nucleation rate, a fast first nuclei-growth and a rate determining second growth step are required. First may be accomplished by using a strong reducing agent. On the other hand, the nuclei growth and *Ostwald*-ripening is dictated by *in situ* stabilization using protective surfactants.
Unprotected metal NPs pursuit a reduction of the surface-to-volume-ratio to lower the chemical potential at the solid–liquid interface. Hence, aggregation of nanoparticles occurs if no or an unsuitable stabilization ligand is used.[31–34,40,45]
In general, nanoparticle stabilization can be categorized into three major concepts: electrostatic,[47–49] steric[33,50–57] and electrosteric stabilization.[58,59]

2.1.2 Fabrication of Metal Nanocrystals

Since palladium and gold nanocrystals were fabricated in this thesis, general approaches of their syntheses shall be outlined.

2.1.2.1 Palladium Nanocrystals

In 1998, the *Miyake*-group was one of the first to synthesize palladium NCs with tunable dimensions.[60] By changing the concentration of the protective polymer (poly(*N*-vinyl-2-pyrrolidone), PVP) in different aqueous–alcoholic solutions PdNC diameters could be altered between 1.7 nm to 3.0 nm. Here, methanol, ethanol or propanol acted as both solvent and reductant. To obtain larger nanocrystals multiple seed-mediated growth processes were applied yielding NCs up to 4.1 nm.
Oleylamine (OAm) is a frequently used surfactant in NC synthesis. *Li et al.*

investigated its influence in PdNC fabrication.[33] Accordingly, an increased amount of OAm lowers the surface energy per unit area which results in geometries with a different surface-to-volume ratios such as icosahedra, tetrahedra, octahedra or triangular plates.
Highly crystalline rectangular PdNCs were fabricated by *Rafailovich et al.*[61] A Pd-precursor was solved aqueous solutions of cetyltrimethylammoniumbromide (CTAB) and reduced by ascorbic acid at room temperature. CTAB is known for its preferential binding to {100} facets. However, to obtain rectangular NCs the addition of trisodium citrate was inevitable which is assumed to be a co-surfactant in the NC formation. Variation of the citrate concentration yielded nanorods (NR) and nanocubes (NCubes) simultaneously with tunable dimensions such as the aspect ratio which ranges between 2.5 and 4.0 for PdNCubes.
Opposed to that, *Xu et al.* fabricated nearly monodisperse PdNCubes using higher concentrations of CTAB at elevated temperatures without the need of trisodium citrate.[58] These single-crystalline nanocrystals (22 ± 0.8 nm in edge lenght) are bound by {100} facets. Here, the Br^--ion of CTAB plays an essential role in the formation of the {100} facet. The bromide-anion was found to be able to chemisorb onto the palladium surface while its chloride counterpart cannot provide adequate stabilization of the {100} facet. Further studies revealed that PdNCubes can be applied in seed-mediated growth processes to yield polyhedral PdNCs.[32] The *Xu*-group showed that iodide-anions can enhance the deposition kinetics of palladium on the {100} facet leading to an enlargement of the {111} facets. Variation of both, temperature and I^--concentration resulted in various single-crystalline geometries such as rhombic dodecahedra, cubes and octahedra.

2.1.2.2 Gold Nanocrystals

One of the most popular and applied processes to synthesize quasi-spherical gold nanoparticles (AuNPs) is the *Turkevich*-method.[62] Here, chloroauric acid is reduced by sodium citrate in water under reflux. A deep red color of the final Au-sol is observed due to a localized surface-plasmon-resonance band (LSPR, see Section 2.1.2.3) of the AuNPs (20 ± 1.5 nm). Over the last years, numerous studies altered this method yielding 13 nm-particles.[12,13,63–67] Due to the facile exchange of the capping agent, these NPs are prone for surface modifications

and were therefore used in various studies.[12,13,51,67]
Another famous approach was presented in 1994 by *Brust et al.* by establishing a method to obtain 4 nm-AuNPs in an non-polar, organic solvent.[59] Here, $HAuCl_4$ is reduced by sodium borohydride in presence of dodecanethiol which acts as capping agent. To enable a phase transfer of the gold precursor from the aqueous to a toluene phase, tetraoctylammonium bromide (TOAB) is added.
Within the last decades, immense effort has been put into fabrication processes to obtain full control over the size, shape and surface chemistry of gold nanocrystal.[40,68,69] Today, methods to yield gold nanoprisms[70], nanocubes,[71] nanocages,[72] nanoshells,[73,74] nanooctahedra[75] and nanobipyramides[76] with variable dimensions are well established. By altering the shape and size of these nanocrystals unique electronic, catalytic and optical properties arise.

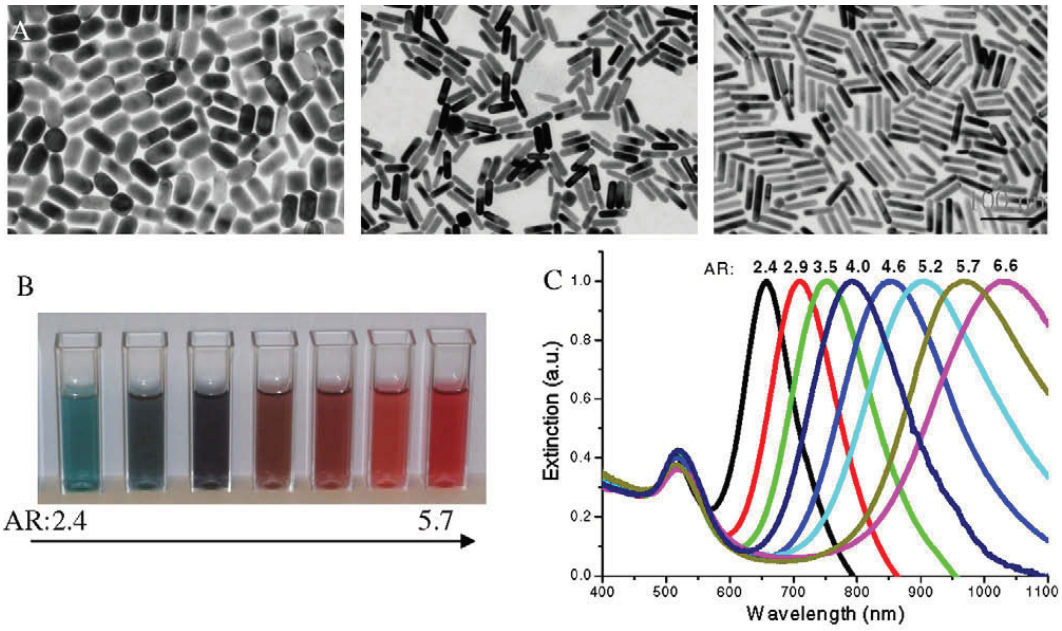

Fig. 2.1: Tunable optical properties of gold nanorods by changing the aspect ratios. Gold nanorods of different aspect ratios exhibit different dimensions as seen by TEM (A), in different colors (B) and different LSPR wavelength (C). Reprinted with permission from *ElSayed et al.*. Copyright 2009 Elsevier.[77]

Another interesting geometry that has not be discussed yet is the cylindrical or nanorod (NR) shape. Due to its anisotropy gold nanorods show special optical properties. Depending on the aspect ratio (AR) between diameter

and length, two distinct peaks in the visible/NIR-range can be observed attributed to two different localized surface-plasmon resonances (see Figure 2.1): a strong longitidunal band along the long axis and a weaker transverse band along the short axis. Due to lower polarizability of LSPR the transverse band is nearly independent on the AR and occurs at ~520 nm similar to the LSPR of 13 nm-AuNPs. The larger the AR the more shifted the LSPR of the longitdunal band towards larger wavelengths.[78] Detailed theoretics about localized surface-plasmon resonances are given in Section 2.1.2.3. The tunability of their optical properties makes AuNRs superior candidates for multiple applications such as plasmon rulers,[79] biological sensing[80,81] or surface-enhanced Raman spectroscopy (SERS).[57,82,83] Due to non-radiative processes (e.g. electron–phonon-coupling) after the absorption of light, AuNRs can transform the incoming energy into heat which is why they are applied in photothermal therapies (PTT) of cancer ulcers.[84–88]

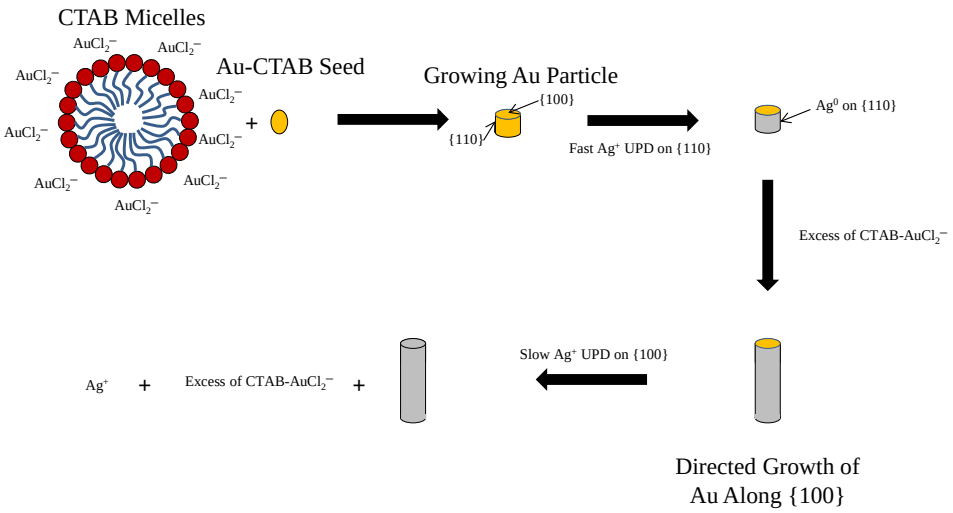

Scheme 2.2: General reaction mechanism of the gold nanorod formation in a seed-mediated growth process.

In general, AuNRs are synthesized by a seed-mediated growth even though some seedless growth approaches are reported as well.[87,89] The mechanism of the seed-mediated growth of gold nanorods is depicted in Scheme 2.2. Here, small

CTAB-capped seeds (~1.5 nm) are formed first by the reduction of Au^{3+} to Au^0 *via* sodium borohydride. The growth solution is prepared separately by reducing Au^{3+} to Au^+ in presence of CTAB and Ag^+-ions and given to the seed-solution. The $AuCl_2^-$-complex hits the seed which leads to a diffusional-controlled growth of the NC towards a nanorod. Several parameters like seed-to-feed ratio, surfactant concentration, silver or gold concentration, pH and temperature can be altered to adjust the desired size and/or aspect ratio.[71,76,77,89–91] To describe the distinct formation of the rod-shape understanding of the so called *underpotential deposition* (UPD) of silver is needed.[92,93] Here, the reduction potential of Ag^+ to Ag^0 is lower at the substrate (in this case: gold) than the potential of the standard reduction potential of Ag^+.[82] The UPD shift ΔU_p is caused by a lowered chemical potential of the adsorbate μ_ads when compared to the respective bulk potential μ_bulk:[92]

$$\mu_\mathrm{bulk} - \mu_\mathrm{ads} = z\,e\,\Delta U_\mathrm{p} \tag{2.1}$$

Here, e represents the elemental charge and z the number of transferred electrons. This criteria is correlated in literature to differences in electronegativity and the respective work functions Φ. If Φ of the bulk of the adlayer-metal is lower than the workfunction of the substrate-metal, an UPD occurs. In the discussed case, the work function of silver is ~0.5 eV lower than work function of gold. Additionally, the structure of the surface has an influence on the work function and therefore on the UPD.[76] For the {111}, {100} and {110}-facets of gold, the difference in work function with Ag^+ is 0.57, 0.83 and 0.85 eV, respectively. Another factor influencing the UPD shift is the accessibility of the surface and the number of nearest neighbors (see Figure 2.2). Here, the {111}-facet has the fewest and {110}-facet the most bonding partners. In this regard, *Sanchez et al.* calculated the UPD shifts for the Au–Ag^+ system with 0.12, 0.17 and 0.28 eV for Au{111}, Au{100} and Au{110}.[94,95] Consequently, deposition is favored onto Au{110} compared to Au{100}. Since the reduction potential of ascorbic acid is about 0.3 V higher than the potential for bulk deposition of silver within the growth solution, a monolayer of silver at Au{110} may be formed, preferentially. These silver atoms shield the surface from further growths by Au^+-ions. However, top of the AuNR (Au{100}) is less covered with silver atoms and is thus growing faster leading to a nearly one-dimensional growth of

the NC. Since the desposition onto Au{100} is not completely inhibited, NR growth stops once a complete passivation is obtained. It appears obvious that by increasing the Ag^+ concentrations higher aspect ratios become accessible.

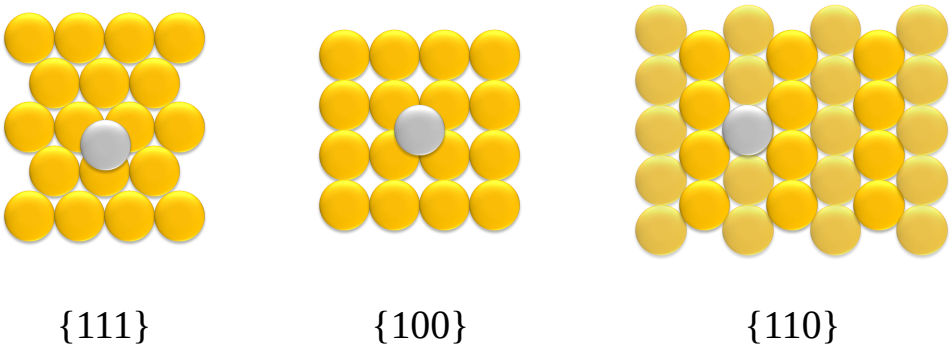

Fig. 2.2: Deposition of silver atoms (silver spheres) onto {111}, {100} and {110}-facets of gold (gold spheres). For the Au{110}-facets, the gold atoms of the underlying second layer are depicted as blurred spheres.

2.1.2.3 Localized Surface Plasmon Resonance

One shared feature of all bulk metals is its metallic luster caused by highly mobile, free electrons within the metal.[96] Due to the overlap of the valence- and conduction band, electrons can relax very quickly to their ground state once they were exited by an incoming electromagnetic wave. Consequently, light is almost fully reflected on planar metal surfaces. The color of the metal is also determined by its electronic properties. In gold for instance, relativistic effects play a crucial role. The s-orbital contraction along with the d-orbital expansion leads to a small band gap between the fully filled 5d band and the Fermi-level of the partially filled 6s band which results in the characteristic yellow color of gold.[97]
However, if the size of the metal reaches the sub-wavelength range other effects become significant. For example, as the particles sizes decreases energy levels go from a quasi-continuous band structure in the bulk material over more discrete energy levels in nanoparticles to a distinct energy level structure in an individual atom.[98] It is obvious that electronic and therefore optical properties become size dependent in a certain range. When a certain oscillating electromagnetic

wave hits a metal NP the conduction band electrons start a coherent oscillation which leads to a charge separation of electrons with respect to the ionic lattice (see Figure 2.3).

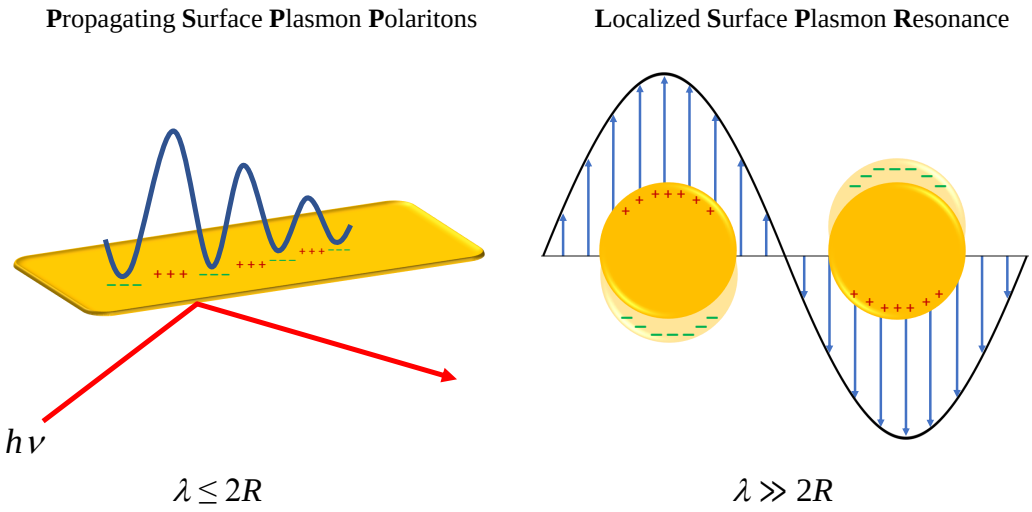

Fig. 2.3: Interaction of an electromagnetic wave with a bulk metal surface and a subwavelength metal nanocrystal leading to either propagating surface plasmon polaritions (PSPP) or localized surface plasmon resonances (LSPR), respectively.

This results in a linear restoring force within the nanoparticle. The amplitude of the dipole oscillation reaches its maximum at a certain frequency called localized surface plasmon resonance (LSPR). For precious metal nanoparticles the LSPR lies in the visible–NIR-range.[79] It has to be noted, that surface plasmons are also present in bulk along the surface–air interface. As displayed in Figure 2.3, the light interacts most efficiently with conduction band electrons at large incident angles. This kind of oscillation is called propagating surface plasmon polaritons (PSPP) which has a limited propagation lengths in the µm-range due to different damping effects. For particles smaller than the wavelength, oscillations are not propagating since the oscillation is distributed over the whole particle.[99] This phenomenon was calculated and described first by *Gustav Mie* in 1908 by applying Maxwell's equations with suitable boundary conditions for the interaction of light with spherical metal NPs.[100] In this so

called *Mie theory* both particle and surrounding medium were characterized by their bulk optical dielectric functions.[98] For the case that the particle diameter is much smaller than the light wavelength a quasistatic approximation and therefore dipolar excitation can be assumed similar to the response to an electric field E_0:

$$E_\mathrm{p} \;=\; E_0 \,\frac{(1 \,+\, \kappa)\varepsilon_\mathrm{m}}{\varepsilon_\mathrm{p} \,+\, \kappa\varepsilon_\mathrm{m}} \tag{2.2}$$

with ε_m as dielectric constant of the surrounding medium, ε_p as dielectric constant of the particle and E_p as electric field inside the particle. κ is a shape factor which connects the polarizability with the geometry of the particle. For spherical NPs, $\kappa = 2$ while other shapes with larger polarizabilities may have higher κ-values.[74] If particles are larger than the incident wavelength multipolar excitations within the particle occur and the *Mie theory* does not apply. The influence of the particle size on the extinction cross-section σ_ext within the quasistatic regime follows:[98,100]

$$\sigma_\mathrm{ext} \;=\; 24\pi^2\, R^3\, \varepsilon_\mathrm{m}^{\frac{3}{2}}\, \frac{\nu\, \varepsilon_{\mathrm{p,\,i}}(\nu)}{c(\varepsilon_{\mathrm{p,\,r}}(\nu) \,+\, 2\varepsilon_\mathrm{m})^2 \,+\, c(\varepsilon_{\mathrm{p,\,i}}(\nu))^2} \tag{2.3}$$

with R as particle radius, c as the velocity of light, ν as light frequency and $\varepsilon_{\mathrm{p,\,r}}$ and $\varepsilon_{\mathrm{p,\,i}}$ as real and imaginary part of the dielectric constant of the particle. In precious metal nanoparticles two types of transitions determine the behavior of $\varepsilon_\mathrm{p}(\nu)$: intraband transitions within the conduction band and interband transition from the valence to the conduction band. This leads to:

$$\varepsilon_{\mathrm{p,\,r}}(\nu) \;= \varepsilon^{\mathrm{IB}}_{\mathrm{p,\,r}}(\nu) \,+\, \varepsilon^{\mathrm{D}}_{\mathrm{p,\,r}}(\nu) \tag{2.4}$$

$$\varepsilon_{\mathrm{p,\,i}}(\nu) \;= \varepsilon^{\mathrm{IB}}_{\mathrm{p,\,i}}(\nu) \,+\, \varepsilon^{\mathrm{D}}_{\mathrm{p,\,i}}(\nu) \tag{2.5}$$

with $\varepsilon^{\mathrm{IB}}(\nu)$ and $\varepsilon^{\mathrm{D}}(\nu)$ denoted as interband (IB) and free electron (Drude-

model, D) contribution. Within the Drude-model dielectric functions are given by:

$$\varepsilon^{\mathrm{D}}_{\mathrm{p,\,r}}(\nu) = 1 - \frac{\nu^2_{\mathrm{plasma}}}{\nu^2 + \gamma^2} \tag{2.6}$$

$$\varepsilon^{\mathrm{D}}_{\mathrm{p,\,i}}(\nu) = \frac{\nu^2_{\mathrm{plasma}}\,\gamma}{\nu(\,\nu^2 + \gamma^2)} \tag{2.7}$$

with ν_{plasma} as plasma frequency of free electrons and γ as inelastic collision frequency of electrons (electron–phonon coupling, defects, impurities).[98] The plasma frequency can be further described by the free electron density N and the electron mass m_{e}:[79]

$$\nu_{\mathrm{plasma}} = \sqrt{\frac{Ne^2}{4\,\pi\varepsilon_0\,m_{\mathrm{e}}}} \tag{2.8}$$

The influence of interband transitions can be illustrated by gold and silver nanoparticles. Even though both metals have similar electronic densities ($\sim 5.9 \times 10^{22}\,\mathrm{cm}^{-3}$) their LSPRs do not occur at the same wavelength due to different d–s interband transitions, respectively. For gold, LSPR is more red-shifted and broadened caused by these transitions compared to silver NPs.[79] As seen it Equation 2.2, an incoming electromagnetic wave induces a strong electric field at the NP surface. This near-field reaches its maximum at the LSPR compared to E_0.[79] For small NPs, the quasistatic approximation holds up and dipolar excitation can be assumed. This leads to an enhanced near-field E_{NF} in vicinity to the NP surface:

$$E_{\mathrm{NF}} \approx \frac{2\alpha\,E_0}{4\pi\varepsilon_0\,r^3_{\mathrm{p\text{-}p}}} \tag{2.9}$$

with α as dipolar polarizability and $r_{\mathrm{p\text{-}p}}$ as interparticle distance. This greatly enhanced near-field can be utilized to enhance transitions within molecules placed in close proximity to the NPs. Surface enhanced Raman spectroscopy (SERS) is one technique which takes advantage of this phenomenon.[57,83,101–103] Here, Raman scattering is able to show large amplifications by five to six orders of magnitude.[104]

This near-field also plays a key role if at least two metal NPs come into contact

with each other.[105–110] Here, the near-fields of each particle individually interact and become coupled which has not only an influence on the localization of the LSPR but also on its intensity. If for instance two AuNPs are in close proximity to one another, LSPR will be strongly red-shifted compared to individual AuNPs in case that the incident light polarization direction is parallel to the interparticle axis.[111,112] For non-spherical particles such as nanorods not only the polarization direction plays a crucial role but also the orientation to one another.[29,113–116]

2.1.3 Fabrication of Mesoporous Silica

In 1968, Stöber *et al.* were the first to synthesize monodisperse, spherical silica particles in the range of 0.05–2 µm which is now known as Stöber's method.[117] Here, alkyl silicates were hydrolyzed in alcoholic solutions followed by a subsequent condensation of silicic acid catalyzed by ammonia (see Scheme 2.3).[118] This pioneer work of *Stöber* was the cornerstone for further studies including constant modifications to yield nanosized silica particles as well as porous silica particles. By processing a silica precursor (silica alkoxide) an ordered network and/or particles of a desired size can be obtained. Here, the rate of hydrolysis is significantly higher under alkaline conditions compared to acidic conditions.[119]

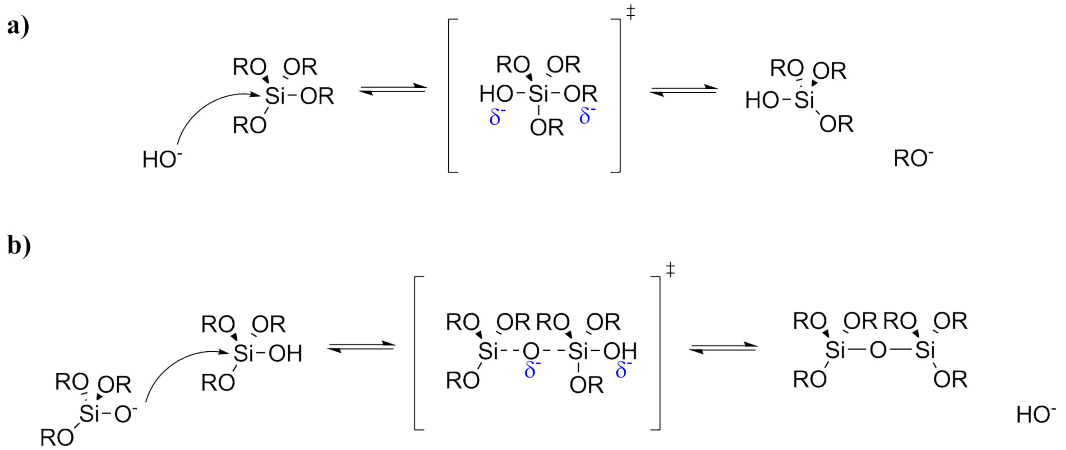

Scheme 2.3: General reaction mechanism of the base catalyzed **a)** hydrolysis and **b)** condensation of silica alkoxides.[118]

In general, porous materials can be divided into three different categories according to the International Union of Pure and Applied Chemistry (IUPAC). 1st: the microporous regime showing pore sizes below 1 nm, 2nd: the mesoporous regime ranging between 2 – 50 nm and 3rd: the macroporous regime which includes all pore sizes greater than 50 nm.[119–123] Mesostructured silica (*m*Si) materials show high surface areas (800 – 1400 $m^2\,g^{-1}$) and large pore volumes in the range up to ≈ 2 $cm^3\,g^{-1}$.[124–127] Typically, mesostructered silica can be formed *via* two different mechanisms depending on the reaction conditions.[119] Both include the formation of silica around self-assembled surfactant micelles (see Scheme 2.4).

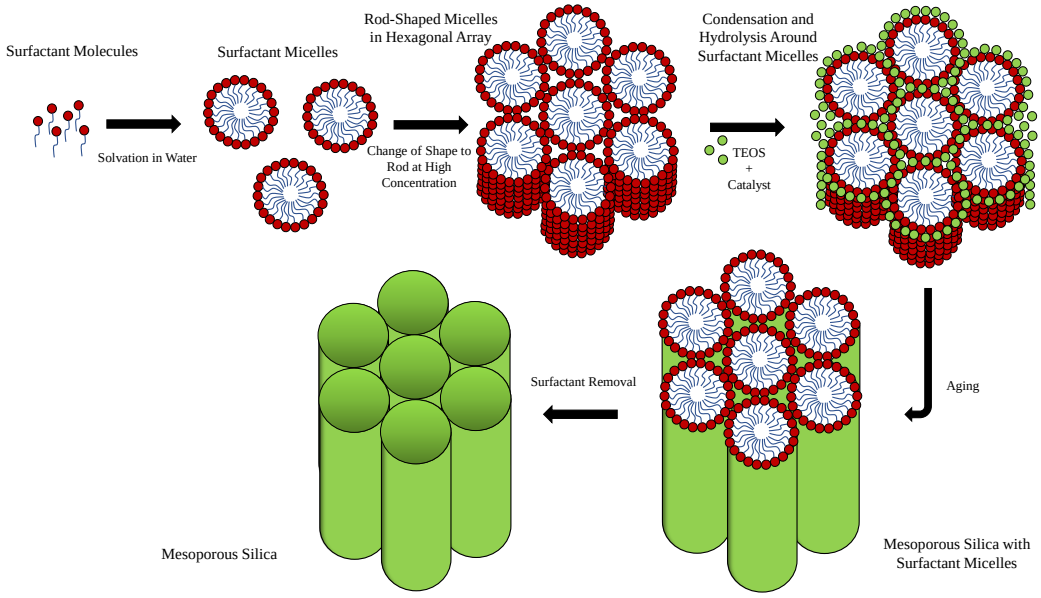

Scheme 2.4: Idealized reaction mechanism to fabricate mesoporous silica from an alkyl silicate as silica precursor in presence of a surfactant which acts as templating agent.

By using tetramethyl orthosilicate (TMOS) as silica source, silicate ions adsorb around the surfactant micelles within the first 40 seconds of the initial growth phase. Due to the partial hydrolysis of TMOS in vicinity to the surfactant, the repulsion between micelles becomes lower which leads to hexagonally ordered mesoporous silica within less than 10 minutes.[128,129]
If tetraethyl orthosilicate (TEOS) is used as an even more hydrophobic silica precursor compared to TMOS, a different mechanism is proposed called the

swelling−shrinking mechanism. Here, TEOS is solved within the hydrophobic core of the surfactant micelles (e.g. cetyltrimethylammoniumbromide: CTAB) which leads to swelling of the micelles and therfore a change in shape from ellipsoidal towards spherical micelles. Once the initial hydrolysis of TEOS starts, it becomes more hydrophilic resulting in its release into the aqueous phase. Since the outer sphere of the CTAB-micelle is positively charged, partially hydrolyzed TEOS gets adsorbed due to electrostatic interactions. Since hydrolysis and condensation of TEOS occurs constantly, micelles shrink in size and agglomerate which results in the formation of the mesoporous silica structure.[130]

With knowledge about these mechanisms there are various tools to tune the characteristics of mesoporous materials towards the desired application. The dimensions, pore size and morphology can be adjusted by altering the reaction conditions which may include the relative ratios between surfactant, catalyst (pH), alkoxysilane or water and environmental conditions such as temperature and stirring velocity.[131–134]

To possess control over the particle size, hydrolysis and condensation of the silica precursor (see Scheme 2.3) has to be altered. Therefore, additives such as amines, alcohols or inorganic salts can increase reaction kinetics and hence result in smaller particles sizes. Various research groups studied the influence of the silica precursor TEOS.[134–136] *Chiang et al.* showed that by increasing the amount of TEOS, particle size can be increased simultaneously.[136] However, if an excess of TEOS is used the particle size distribution changes from monodisperse to heterogeneous due to secondary condensation reactions which produce further nuclei amongst already existing silica particles.[134,135] *Kuroda et al.* investigated the influence of the alkyl chain ($Si(OR)_4$ with R = Me, Et, Pr, Bu) of silicon alkoxides in the respective alcoholic solution.[137] Longer alkyl chains decreased the hydrolysis rate and therefore increased the particle size up to 330 nm (R = Bu) compared to 20 nm for R = Me. Instead of using NaOH and NH_4OH as base catalysts *Möller et al.* used triethanolamine (TEA) which can also act as complexing agent.[138] By simple variation of the ratio between TEOS and TEA particle size could be tuned between 50 and 100 nm. *Qiao et al.* investigated the influence of various additives under certain pH-values.[139] It could be shown that the size of the nanoparticles is mainly determined by the initial pH and can be varied between 25 and 200 nm depending on the

acid−base buffer capacity of the reaction mixture.
In general, the pore size is given by the dimensions of the surfactant (-micelles). Therefore, an easy approach is to alter its chain length to tune the pores between $3-40\,\mathrm{nm}$.[124,140–142] The influence of the concentration of CTAB as surfactant was studied by *Beck et al.* leading to the development of one of the most famous mesoporous materials called *Mobil Composition of Matter No. 41* (MCM-41).[124] If the concentration is too low to form micelles no template effect can be utilized whereas very high concentrations lead to disordered structures. Besides the alkyl chain length the counter ion also affects the pore size and the mesostructural ordering.[143] If cetyltrimethylammoniumchloride (CTAC) is used as template a wormhole-like arrangement of the mesostructure is formed. By changing the counter ion to the larger tosylate ion in cetyltrimethylammoniumtosylate (CTATOS), the pore size increased and its structure changed from worm-like to stellate. Another approach was presented by *Huang et al.* where a dual templating sol−gel reaction was applied.[144] Here, a partially fluorinated, short-chain, anionic surfactant (Capstone FS-66) was mixed with CTAB. By increasing the amount of Capstone FS-66 the pore size increased and the morphology changed from a small, dendritic, channel-like structure to a large, dendritic, flower-like structure.
Due to its high surface area, large pore volumes and therefore enhanced loading capacity, mesoporous silica is of highest interest for biomedical applications. Especially, *m*Si systems are prone as drug delivery carriers. Hence, both hydrophobic and hydrophilic drugs can be adsorbed or bound to the *m*Si.[119] By specific surface functionalization and/or the pore size profile the drug release can be controlled. This approach can also determine the application as targeted anti-cancer therapeutics. Due to the enhanced permeation and retention (EPR) effect of tumor ulcers particles ($>5\,\mathrm{nm}$) accumulate within the tumor tissue which can be further enhanced by targeting ligands bound to the mesoporous surface. Once the *m*Si particles reach their target a controlled drug release is needed. This can be achieved by various stimuli such as pH, redox, temperature, light, magnetism or ultrasound depending on the respective surface functionalization.[119,121,123] Additionally, the large surface area of *m*Si is highly advantageous for biomedical imaging applications. The mesoporous structure offers sufficient protection and stability and can be further loaded with fluorophores, dyes or other contrast agents such quantum dots.

Besides medical applications *m*Si is found in various catalytic applications. Mesoporous silica offers a high permeability along with sufficient thermal and chemical stability.[122] For example, volatile palladium complexes are used to incorporate palladium into MCM-41 *via* vapor deposition and perform Heck-reactions.[145]

2.2 Synthesis of Tailored Polymers

2.2.1 Reversible Addition–Fragmentation Chain Transfer Polymerization

The conventional free radical polymerization (FRP) is one of the most performed techniques in industry to obtain polymeric materials. Due to its good compatibility with multiple monomers and its high tolerance towards various functional groups, FRP is known for its advantageous operability.[146] In contrast to other polymerization techniques such as polycondensations or living/anionic polymerizations, free radical polymerization is rather insensitive towards impurities and high molecular weight species are formed initially once the reaction has started. However, there are still some limitations in the FRP process. A control over the average molecular weight M_n and its distribution is not accessible in a conventional free radical polymerization. Additionally, no unique archtitectures such as star- or comb-polymers as well as (multi)block-copolymers can be fabricated.

To obtain control over the molecular weight distribution ($Đ \leq 1.2$) and to enable exclusive topologies, chain transfer agents (CTA) can be a very helpful tool.[147–149]. In general, these processes are described in literature as reversible-deactivation radical polymerization (RDRP). Atom transfer radical polymerization (ATRP)[150] and nitroxide mediated polymerization (NMP)[151] are the two most famous candidates of RDRP-techniques. Both techniques rely on the so called *persistent radical effect* by using a CTA in the form of R-Y whose bond can be easily broken homogeneously by another radical. Here, the cross-product between the radicals $R^{\bullet}$ and $Y^{\bullet}$ becomes more pronounced throughout the process since termination between the short-living $R^{\bullet}$ proceeds very fast and the termination between two persistent $Y^{\bullet}$ radicals is greatly suppressed. If for instance a metal complex (e.g. Cu^{+}, Ru^{+} or Fe^{2+}) with two accessible oxidation

states is added in ATRP, the cross-product is formed reversibly. Consequently, an equilibrium between an active and an inactive species occurs which lies on the inactive species side.[150] In effect, the radical concentration is reduced and therefore termination is suppressed. This leads to low dispersities $Đ$ but simultaneously to slower overall reaction rates.
Another prominent technique in controlled FRPs is the reversible addition–fragmentation chain transfer polymerization (RAFT) which does not rely on the persistent radical effect but rather on a reversible chain transfer.[152,153] In 1998, *Rizzardo et al.* applied dithioesters, xanthogenates, dithiocarbamates and trithiocarbonates in radical polymerizations which gave rise to low dispersities and non-reduced reactions kinetics at the same time. Various topologies as well as functionalization opportunities are accessible by choice of the fitting RAFT-agent.[154,155] Even di-, tri- or multiblock copolymers are accessible depending on the structure of the RAFT-agent and the monomer sequence. The general chemical structure of a RAFT-agent is displayed in Figure 2.4.

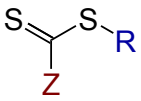

Fig. 2.4: Chemical structure of a RAFT-agent.

Here, **R** is ascribed as leaving group while **Z** symbolizes the stabilizing group. The reaction mechanism is depicted in Scheme 2.5. Two equilibria superimpose the elemental reactions of the conventional FRP process. After the decomposition of the initiator and the additions of some monomers, $P_m^\bullet$ adds onto the RAFT-agent. To ensure a sufficient addition the Z-group has to stabilize the C-centered radical but simultaneously if the stabilization is too strong fragmentation is suppressed and the radical is trapped in this state.[156] On the other hand, the R-group has to form a similary or slightly more stabilized radical than $P_m^\bullet$ to enable its own fragmentation from the C-centered state. At the same time it has to be a good initiating radical for further monomer additions. Once the pre-equilibrium is overcome, an alternation between addition and fragmentation of oligomeric or polymeric chains occurs leading to similar propagation probabilities which leads to narrow molecular weight distributions. Opposed to RDRP-processes the reaction rate is not decreased if both, addition- and fragmentation-steps are fast.[157,158]

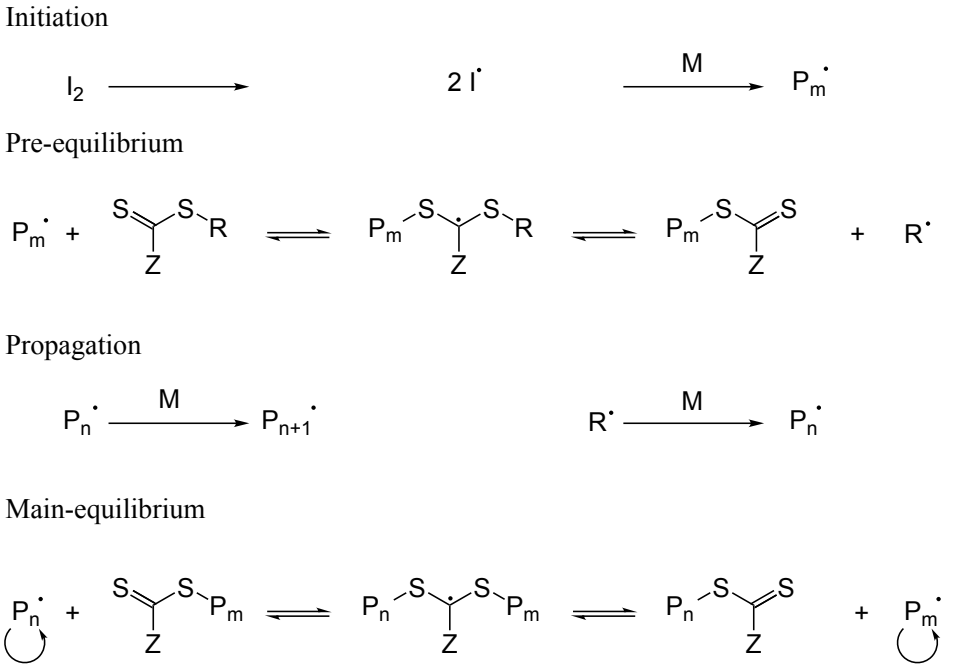

Scheme 2.5: General reaction mechanism of the RAFT-process with $\mathbf{I_2}$: Initiator, $\mathbf{I^{\bullet}}$: Initiator fragment, **M**: Monomer, $\mathbf{P^{\bullet}_m}$: Short-chain, polymeric radical, **Z**: Stabilizing group of the RAFT-agent, **R**: Leaving group of the RAFT-agent, $\mathbf{P^{\bullet}_n}$: Long-chain, polymeric radical.

The RAFT-process not only yields polymers with a narrow molecular weight distribution but also bears the possibility to adjust the average molecular weight M_n. Under the assumptions that all monomer building units are homogeneously incorporated into the RAFT-agent molecules while chains produced by the initiator are neglected, the theoretical average molecular weight $M_{n,\mathrm{theo}}$ can be predicted by knowledge over the ratio between monomer and RAFT-agent concentrations ($^{[\mathrm{M}]}/_{[\mathrm{RAFT}]}$) and can therefore be precisely tuned by the following equation:[109]

$$M_{n,\mathrm{theo}} = \frac{[\mathrm{M}] \cdot M_{\mathrm{M}} \cdot \mathrm{conversion}}{[\mathrm{RAFT}]} + M_{\mathrm{RAFT}} \tag{2.10}$$

Here, M_{M} and M_{RAFT} correspond to the molecular weights of the monomer and the RAFT-agent, respectively.

2.2.2 Grafting Approaches

In our day-to-day life we frequently encounter polymer coatings as protective, anti-scratch surfaces on smartphones or in our living environment on e.g. kitchen furniture.[159] Even in more sophisticated applications such as in electron-beam lithography towards micro-chip production,[37–39] ultra-hydrophobic surfaces,[160] anti-bacterial surfaces[161,162] or other smart surfaces,[163] polymer coatings become immensely important. One distinct disadvantage of commonly used polymer coatings is based on the fact that they are only physiosorbed and therefore only weakly attached to the respective surface.[67] Additionally, nanoscale coatings are hardly accessible since usual approaches yield polymer films in the µm- or mm-range.

To ensure that polymers are permanently linked to a certain surface within the nanoscale regime, three different strategies are applicable: *grafting-to*, *grafting-from* and *grafting-through* (see Scheme 2.6). All three approaches are known to be applicable not only to bulk surface but also to various types of organic and inorganic nanoparticles. The choice of the anchor-group obviously depends on the nature of surface to be functionalized. For noble metal surfaces such as gold and silver, sulfur[12,164–167] containing functionalities are applied whereas for oxide surfaces like silica or titanium oxide, silanes or catechols are used, respectively.[22,163,168,169]

In the grafting-to approach polymers are synthesized prior to functionalization experiments. The anchor group can either be inherently bound the the polymer (for instance in RAFT-polymerization) or attached to the polymer afterwards. Generally, the grafting-to strategy bears the advantage that the polymer can be fully analyzed beforehand and separately from the surface. Additionally, it offers a higher step-efficiency and scalability than the grafting-from approach. However, due to the steric demand of already existing macromolecules, high grafting densities are difficult to achieve.[67,170] Still, similar to the grafting-from approach, the coating thickness increases with an increasing polymer chain length.[12,14,19,171,172]

As depicted in Scheme 2.6 the grafting-from approach can be broken down into initiator-bound, Z-group and R-group approaches. Here, either the initiator or a CTA is anchored to surface prior to polymerization.[67,168,171–173] Azo-initiators are commonly used in initiator-bound grafting-from polymerizations.[173] Opposed to that, in RAFT-controlled grafting-from approaches it has to be

distinguished between R-group and Z-groups approaches. Using the R-group approach, the leaving group (see Scheme 2.5) of the RAFT-agent is covalently bound while in the Z-group approach the stabilizing group is attached to the surface. During the R-group approach the polymer chain remains immobilized on the surface and growths throughout the polymerization. In contrast to that, within the Z-group approach, the polymer is cleaved off due to the RAFT mechanism and polymerizises in solution. After a few propagation steps including further additions of monomer units, the long-chain radical adds on the surface-bound RAFT-group again. Grafting densities can be easily controlled by using suitable anchors for the respective polymerization technique and dummy-anchors, simultaneously. [173,174]
In the grafting-through approach a molecule with an adequate anchor group and an unsaturated unit is immobilized on the surface. [168,175] Propagation with another monomer occurs in solution and the surface-bound monomer is added to the long-chain radical, eventually.

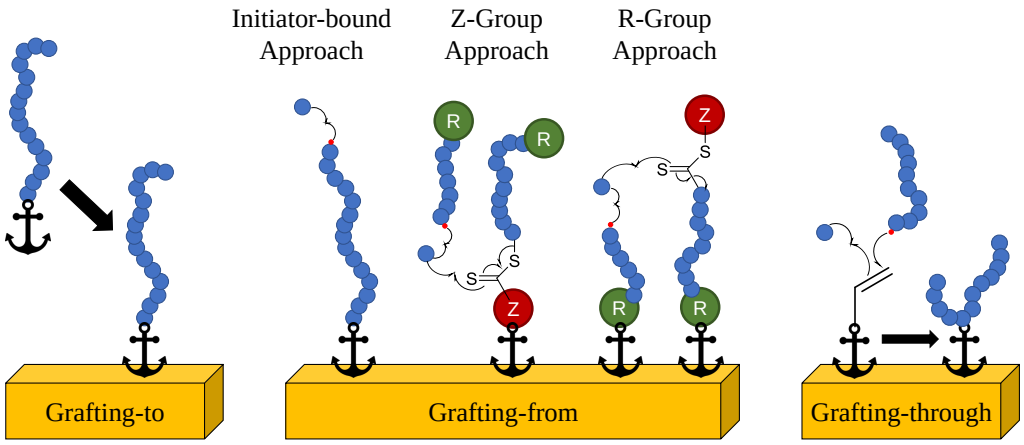

Scheme 2.6: Idealized grafting strategies towards polymer-grafted surfaces.

2.2.3 Poly(*N*-Isopropyl Acrylamide) as Smart Material

Among other polymers such as poly(*N*-vinylcaprolactam) (PVCL),[176] poly(*N*-vinylpyrrolidone) (PVP),[176] and poly(vinyl methyl ether)(PVME)[177] poly(*N*-isopropyl acrylamide) (poly(NIPAM)) shows thermoresponsive properties in aqueous solutions.[178,179] Due to its lower critical solution temperature (LCST) in water at 32 °C ($M_n > 10^4\,\mathrm{g\,mol^{-1}}$) poly(NIPAM) is often described as smart, intelligent or stimuli-responsive polymer. Such polymers interact with their environment (temperature, pH, light, etc.) and change their physical and/or chemical properties once a certain threshold of the respective stimulus is reached.[180,181] It is not surprising that various applications like in tissue engineering,[182] chromatography,[183] drug delivery,[165,184,185] sensoring,[186] etc. are based on such smart polymers.

Poly(NIPAM) is typically synthesized by free[178] or controlled[12] radical polymerization techniques from its respective monomer *N*-isopropyl acrylamide. When talking about the lower critical solution temperature (LCST) solution properties of polymers in general must be considered.[67] In a typical temperature–mole-fraction phase diagram a binary polymer solution can possess two different coexistence/bionodal curves: upper and lower. Under the upper coexistence curve two separate phases are present meaning that the polymer is not soluble at lower temperatures. In the other case of a lower coexistence curve the polymer becomes inmiscible at elevated temperatures. The temperatures lying on the lower coexistence curve are generally known as cloud points T_{cloud}. However, both curves show a maximum or minimum respectively which are referred as upper critical solution temperature (UCST) or lower critical solution temperature (LCST). Between these coexistence curves the polymer is soluble at any temperature and mole-fraction.

From the thermodynamic point of view this behavior can be described by considering the free mixing enthalpy ΔG_{mix} (see Equation 2.11).[187] It has to be negative if the solution shall be fully miscible:

$$\Delta G_{\mathrm{mix}} = \Delta H_{\mathrm{mix}} - T\,\Delta S_{\mathrm{mix}} < 0 \tag{2.11}$$

Here, ΔH_{mix} and ΔS_{mix} symbolize the mixing enthalpy and mixing entropy, respectively. Concerning the LCST case, both ΔH_{mix} and ΔS_{mix} have to be

negative. On the other hand, if the system shows a UCST both mixing enthalpy and mixing entropy possess positive values:

$$\text{LCST} : \Delta H_{\text{mix}} < 0 \quad \Delta S_{\text{mix}} < 0 \tag{2.12}$$

$$\text{UCST} : \Delta H_{\text{mix}} > 0 \quad \Delta S_{\text{mix}} > 0 \tag{2.13}$$

As experimental chemist, the UCST is more familiar since elevated temperatures are commonly applied in the lab to enhance the solubility of solids. The LCST phenomena on the other hand is not intuitive since it requires a negative ΔS_{mix} meaning that thermodynamically the system is more ordered when mixed together. A basic requirement for this behavior relies in the formation of ordered structures between the solvent molecules (e.g. water) and the macromolecular chain.[67] For poly(NIPAM), this effect was discovered in 1968 by *Heskins* and *Guillet* by investigating aqueous solutions of the polymer.[178] Here, water molecules strongly bind to the amide moieties of NIPAM over hydrogen-bonds below the LCST (hydrated state). Due to the sterically demanding isopropyl groups intramolecular bonding between adjacent NIPAM moieties is hindered.[188] Once a certain temperature is reached (cloud point T_{cloud} or LCST) water molecules are pushed out of the polymer coil and the polymer chains collapse which leads to coild-to-globule transition (see Scheme 2.7). Subsequently, the chains start to aggregate towards larger agglomerates to reduce the surface area and therefore the high surface tension between the dehydrated, hydrophobic polymer and water. Here, solutions become cloudy and turbid due to the enhanced light scattering of the agglomerates. However, this transparent-to-turbid transition is fully reversible when the temperature is decreased again. Besides its abruptness this is one of the major features why poly(NIPAM) is considered as smart material. Within the phase diagram of aqueous poly(NIPAM) solutions the spinodal curve is very flat meaning that the cloud point is not highly affected by the composition of the solution.[189] Therefore, transition temperatures for any mole fractions are often assigned as LCST values in literature even though the exact concentration for the minimum of the spinodal or binodal (LCST) was not determined.
The LCST of poly(NIPAM) is generally given for an average molecular weight $M_n > 10^4\,\text{g}\,\text{mol}^{-1}$ at atmospheric pressure in water with only little to none ions present. It is not surprising that the LCST of the polymer is dependent on

various parameters such as the average molecular weight,[190] its end-group functionality,[191] its architecture[192] and its composition.[193] Latter includes the copolymerization with another monomer mostly to tune the LCST value towards physiological relevant temperatures.

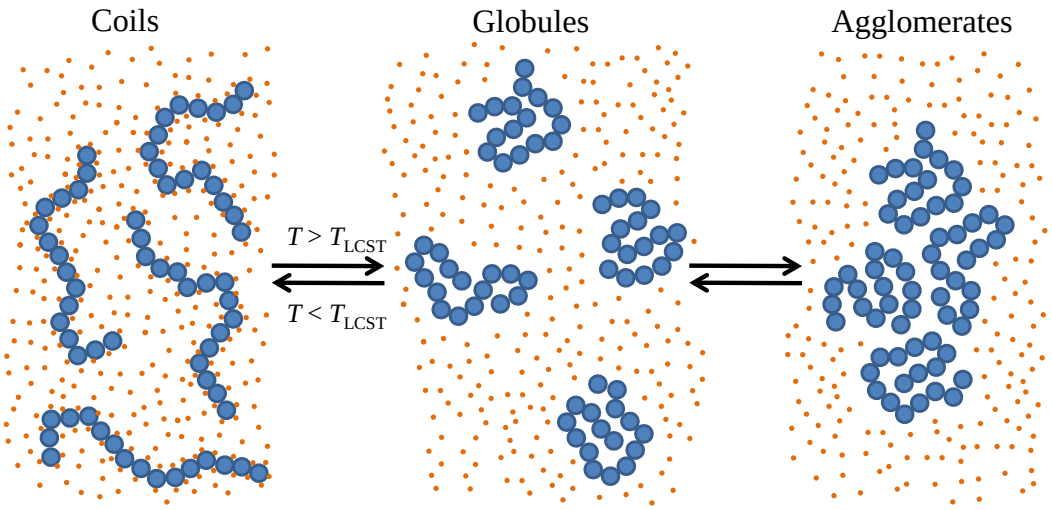

Scheme 2.7: General mechanism of the coil-to-globule phase transition of poly(NIPAM) upon heating followed by the formation of agglomerates.

Another paramter affecting the lower critical solution temperature of poly-(NIPAM) is the salt concentration which is correlated to the so called *Hofmeister* series.[190,194,195] Originally, this series ranked the ability of inorganic salts to "salt-out"/precipitate proteins from aqueous solutions. In general, this effect is more dependent on the anion than the cation which results in a typical ranking for the anions:

$$CO_3^{2-} > SO_4^{2-} > H_2PO_4^- > F^- > Cl^- > Br^- \approx NO_3^- > I^- > ClO_4^- > SCN^-$$

Anions on the left are called kosmotropes and are highly hydrated whereas anions on the right are referred as chaotropes and are only weakly hydrated. Consequently, depending on the anion different interactions with poly(NIPAM) play a role in the mechanism of the LCST phase transition. *Cremer et al.*

investigated the phase behaviour of poly(NIPAM) in presence of sodium salts of various Hofmeister anions and accounted three basic interactions (see Figure 2.5). Here, chaotropic anions decrease the LCST due to an increasing surface tension (Figure 2.5 **(b)**) between water and the hydrophobic parts of the polymer (e.g. backbone and isopropyl groups) and a weak salting-in effect (Figure 2.5 **(c)**). Both interactions can be assigned to anions from Cl^- to SCN^-.

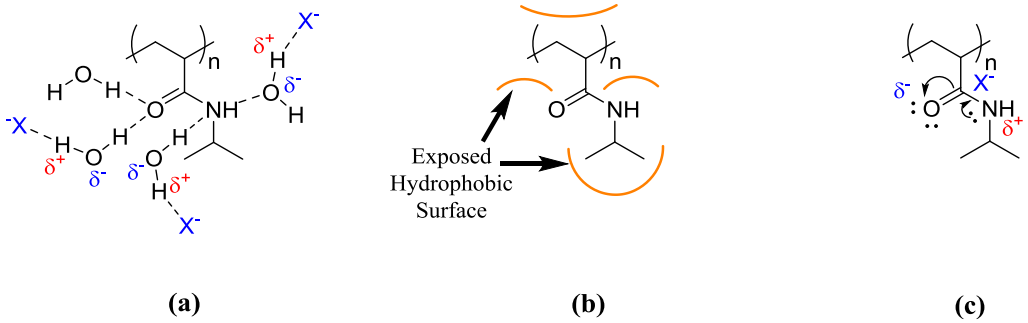

Fig. 2.5: Basic interactions of Hofmeister anions with poly(NIPAM) and hydrating water molecules: **(a)** Polarization of water molecules bound to the amide group of poly(NIPAM), **(b)** Increased surface tension between hydrophobic moieties of the polymer and water and **(c)** salting-in effect and direct binding of the anion to the amide group of poly(NIPAM).

In the case of kosmotropic anions (from CO_3^{2-} to F^-) another effect is declared. Here, anions weaken the hydrogen-bonds between amide groups and water by polarizing the respective water molecules (Figure 2.5 **(a)**) which facilitates its dehydration and therefore decreases the LCST. Separated from this behavior is the hydrophobic dehydration of water molecules from the rest of the polymer.

3 Catalytic Application of Palladium-Core–Silica-Shell Nanohybrids

The content of the following chapter has already been published by the author of this work and results were adapted with permission of the journal and the authors.[196]

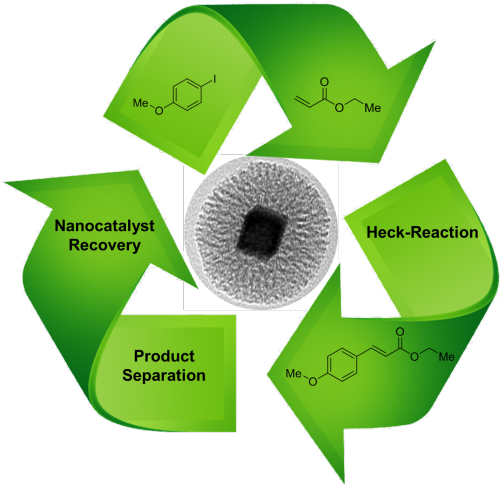

3.1 Introduction and State of the Art

The demand for resource-efficient organic syntheses has increased drastically over the last decades. Especially, due to the consistently growing population and economy, smart strategies for a sustainable usage of limited resources such as precious metals and hydrocarbons are inevitable.[197–199] Generally, catalysis gives rise to novel and energy saving synthetic routes. However, homogeneous catalysis is not widely used in industrial processes, due to the need of mostly toxic ligands and the costly purification along with a restricted

reusability potential.[200–202] Heterogeneous catalysis based on the utilization of metal nanocrystals overcomes most of these limitations. Due to its high surface-to-volume ratio, catalytic activities are drastically increased opposed to bulk materials. However, the most common disadvantage in NC-based catalysis relies in the occurrence of aggregates during the reaction which leads to a decrease of catalytic active surface. Several studies were presented already in literature to delay that phenomenon using micelle-like- or core–shell nanostructures as potential nanocatalytic systems.[53,56,203–206] Other approaches used the deposition of small NCs in a mesoporous support offering a large active surface area.[145,207–209] In this context, it is crucial to find an adequate balance between permeability for small organic molecules and the overall stability of the nanocatalyst. As seen in Scheme 3.1 palladium nanocubes can be functionalized with various *N*-isopropyl acrylamide polymers fabricated by the reversible addition–fragmentation chain transfer polymerization (RAFT). However, thermal stability of the shell and its sulfur-containing anchor group is insufficient leading to the formation of palladium aggregates and therefore a decreased surface area available. Overcoming this obstacle is the subject matter of this chapter and may contribute to a sustainable supply of drugs and other organic substances.

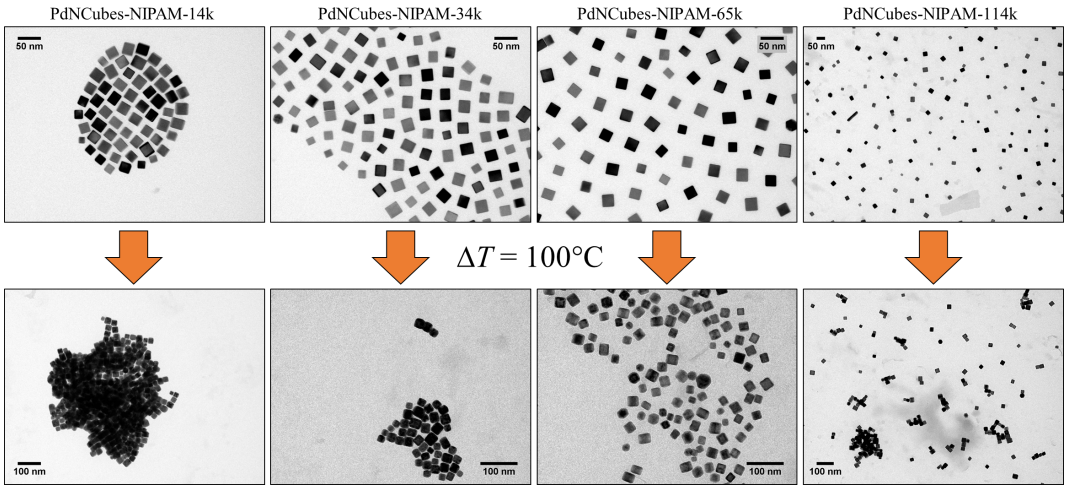

Scheme 3.1: TE micrographs of PdNCubes functionalized with different NIPAM RAFT-polymer before and after heat treatment at 100 °C.

3.2 Fabrication of CTAB-capped Palladium Nanocubes

Xu and coworkers demonstrated a straightforward and seedless approach to obtain palladium nanocubes (PdNCubes).[32,58] Accordingly, a Pd^{2+}-precursor was reduced by ascorbic acid in aqueous solution using cetyltrimethylammonium-bromide (CTAB) as surfactant. For a detailed description of the experimental procedure see Experimental Section 8. Further studies could show that these PdNCubes (edge length: 22 nm) can be applied in a seed-mediated growth of polyhedral Pd nancrystals.[32]
In this work, the procedure of *Xu et al.* was modified so that a 10-fold upscaling could be accomplished. The respective transmission electron micrographs (TEM) and the selected area electron diffraction (SAED) pattern of the as-obtained PdNCubes are shown in Figure 3.1. Latter indicates the single-crystallinity of the NCubes bound by {100}-facets. The evaluation of multiple TEM images revealed an average edge length of (18 ± 2) nm (see Figure 3.2). The role of CTAB in the fabrication process of palladium nanocubes is described in literature intensively.[58,61,210] Previous studies showed that CTAB can be removed from metallic NCs and replaced by other ligands such as thiolated alkyls,[211,212] DNA[213] or synthetic polymers.[87,214] Consequently, it appeared promising that this approach is highly advantageous for further functionalization experiments.

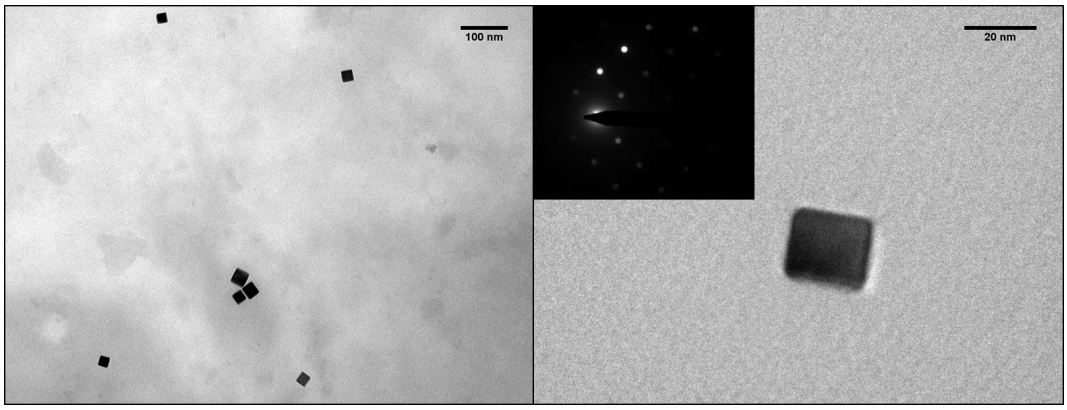

Fig. 3.1: TE micrographs of CTAB-capped PdNCubes and the respective SAED pattern.[21]

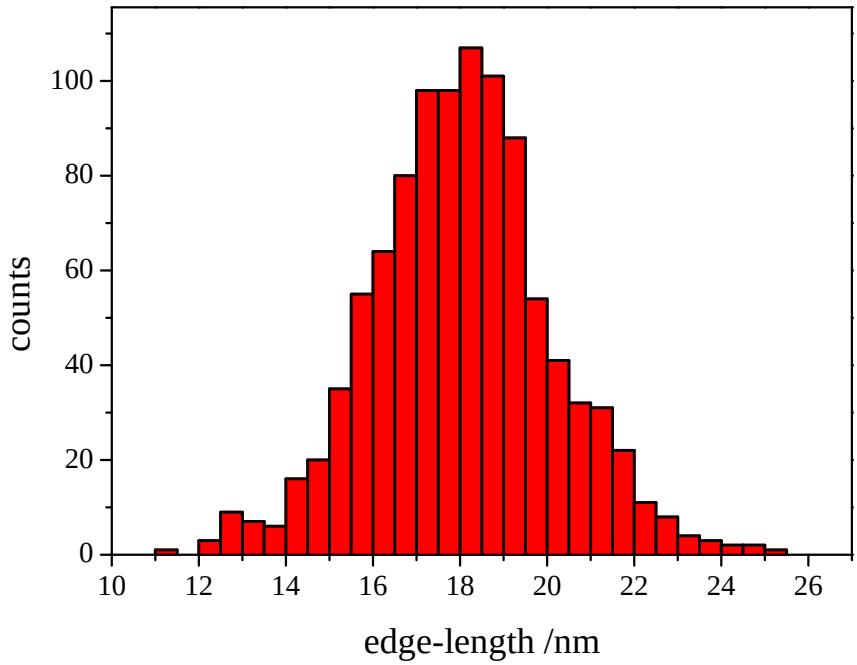

Fig. 3.2: Histogram of the Pd edge length distribution obtained by evaluating multiple TE migrographs of PdNCubes.

3.3 Mesoporous Silica Coating on Palladium Nanocubes

Opposed to other nanocrystal functionalization approaches where CTAB was simply removed and replaced by other surfactants *Matsuura et al.* used CTAB as template for the formation of a mesoporous silica (*m*Si) shell.[215] They demonstrated that CTAB-capped AuNRs and CdSe/ZnS quantum dots can be applied in a single-step coating appraoch to yield a silica shell with ~4 nm pores and ~2 nm walls. Since the PdNCubes are covered by CTAB already no surfactant exchange is necessary. Consequently, this procedure could be directly transferred to the as-obtained PdNCubes (~10^{15} particles/L) using tetraethyl orthosilicate (TEOS) as silica precursor in an alkaline solution (see Scheme 3.2). For a more detailed description of the conducted procedure see

Experimetal Section 8. The amount of $2 \times 6\,\mu L$ TEOS was found to give the best results so that neither free silica particles were formed nor crosslinking between silica coated PdNCubes occurred.

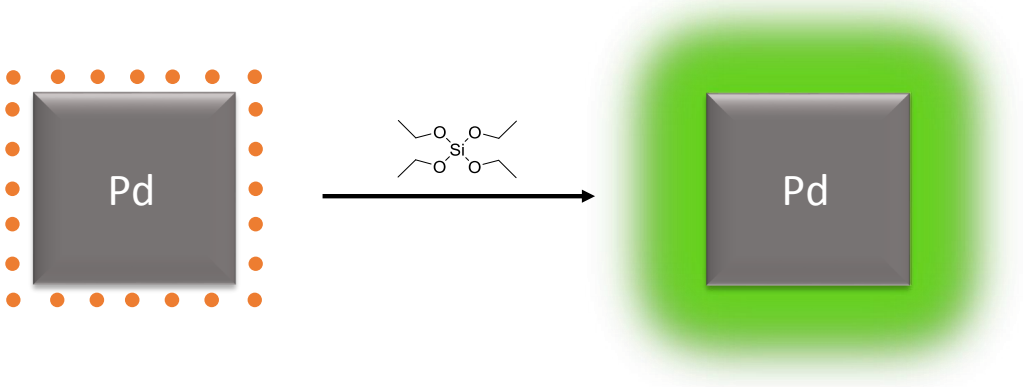

Scheme 3.2: Single-step approach to obtain a mesoporous silica shell on CTAB-capped PdNCubes.

TE micrographs of individual Pd–*m*Si nanohybrids are depicted in Figure 3.3 showing a spherical silica coating with a thickness of (17 ± 2) nm (for histogram see Figure 3.4). The porosity is essential to ensure that vacant coordination sites on the palladium-core are present and accessible for catalysis. In contrast to other multistep approaches, pores are formed *in situ* with no additional etching step necessary.[117,216] This avoids the usage of harmful etching agents such as fluorides or ammonia.[217]
The silica shell then served as platform for further surface modification using two different PEG-silanes ($M_n = 5{,}000\,g\,mol^{-1}$ and $M_n = 20{,}000\,g\,mol^{-1}$, see Figure 8.2). TE microscopy did not reveal any changes in the structure of the PEG functionalized Pd–*m*Si nanohybrids opposed to the unfunctionalized nanocatalyst, since the contrast of polymer is too low (see Figure 3.5). However, dynamic light scattering (DLS) measurements in diluted aqueous solutions proved an increased hydrodynamic radius with increasing molecular weight of the PEG-chain grafted onto the silica shell (see Figure 3.6). These results provide evidence that only individual nanostructures are formed while no larger aggregates are present.

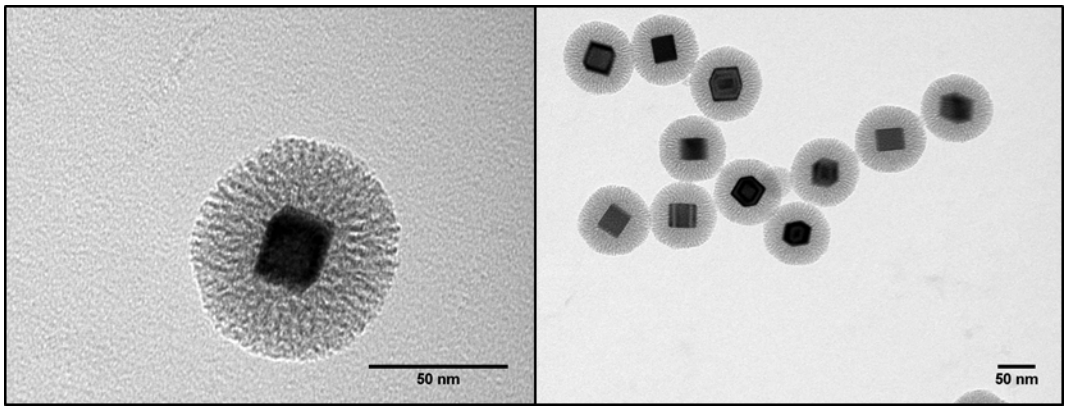

Fig. 3.3: TE micrographs of Pd–*m*Si nanohybrids fabricated *via* a single-step coating process.

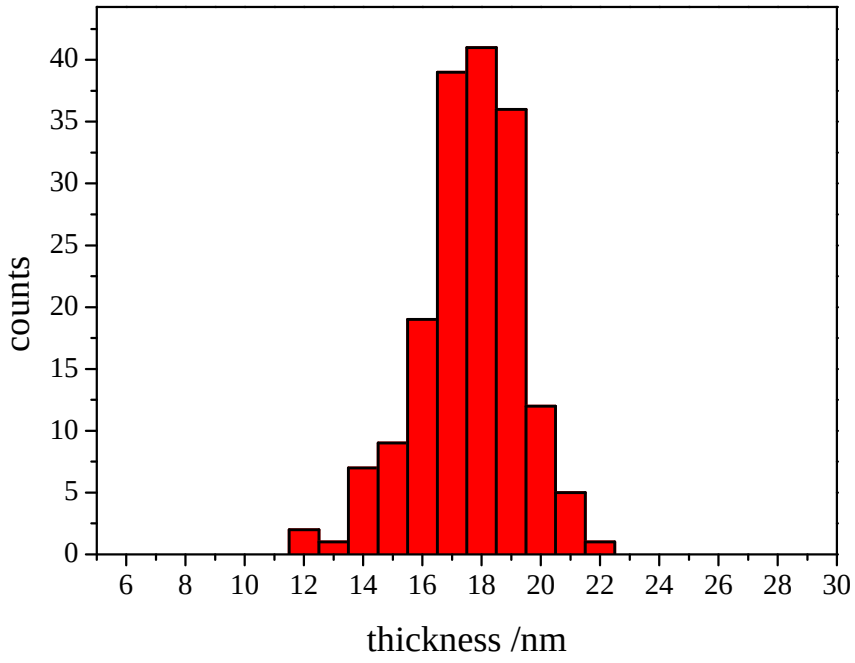

Fig. 3.4: Shell thickness distribution obtained by evaluating multiple TE migrographs of Pd–*m*Si nanohybrids fabricated *via* a single-step coating process.

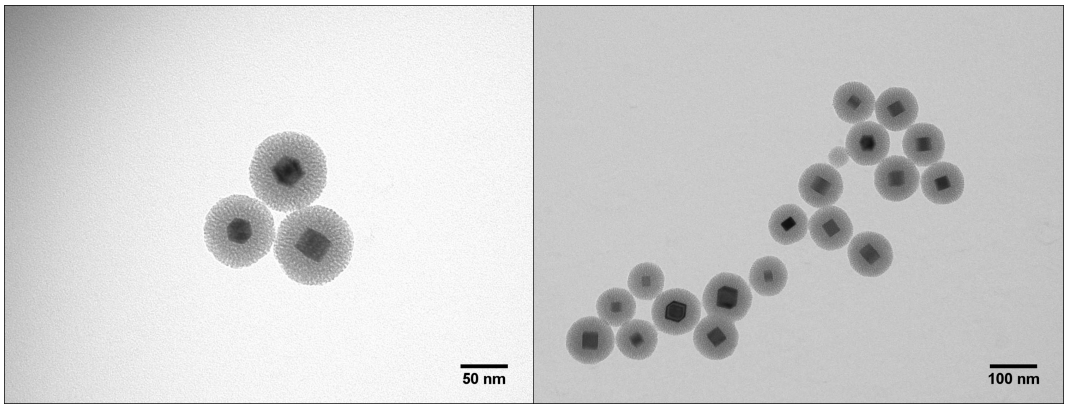

Fig. 3.5: TE micrographs of Pd–*m*Si–PEG-5k nanohybrids.

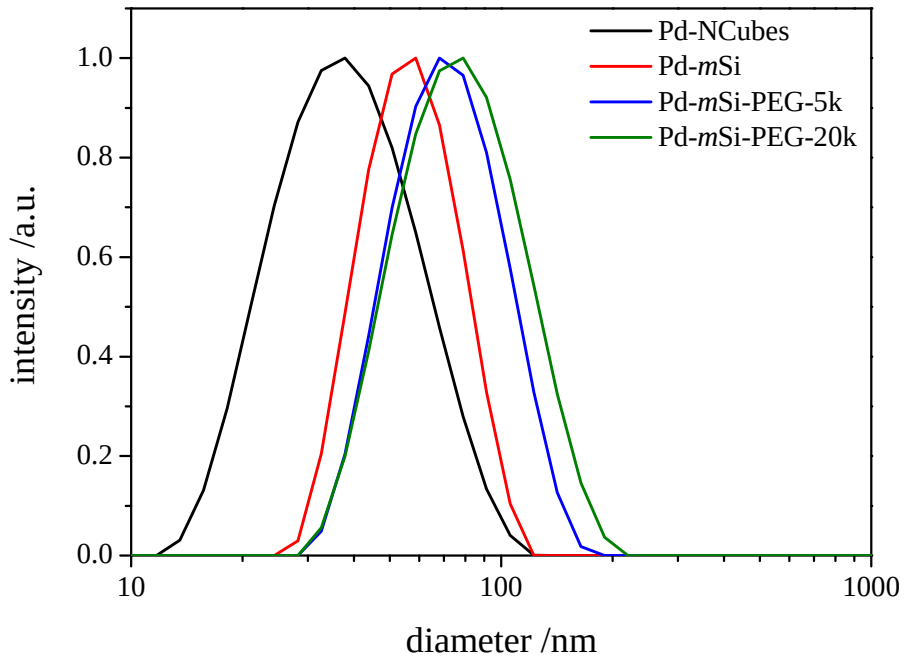

Fig. 3.6: DLS distributions of different palladium nanohybrids obtained in nanopure water at 25 °C.

3.3.1 Catalytic Application of Pd–*m*Si–PEG-5k in Heck-Reaction

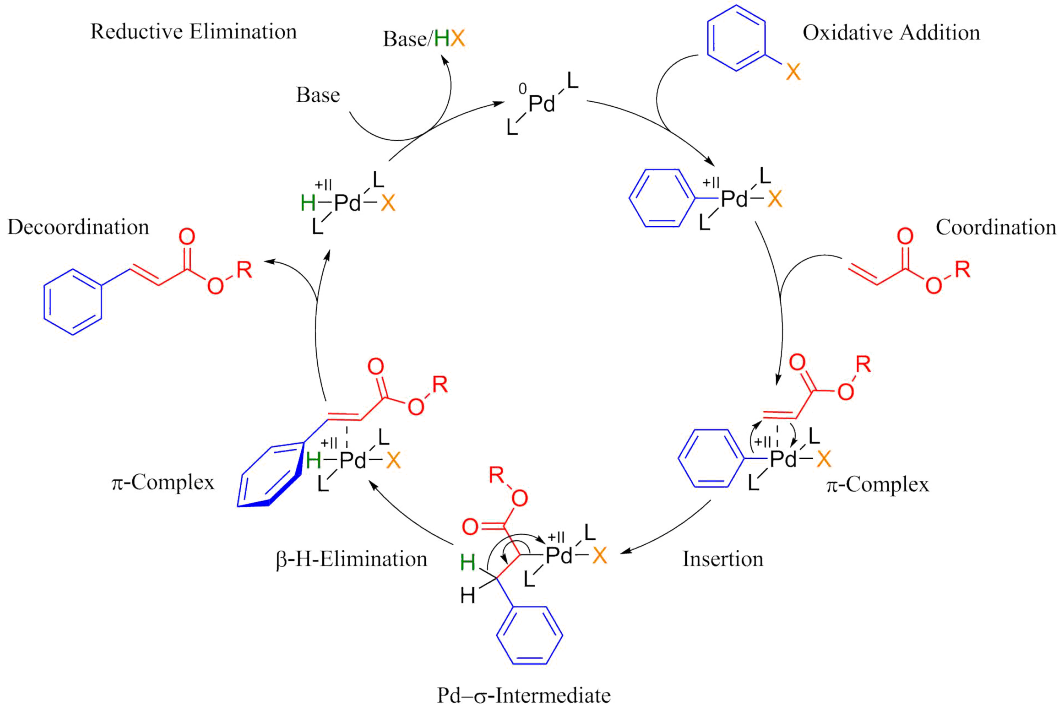

Scheme 3.3: General mechanism of the palladium catalyzed Heck-reaction between an aryl halide (Ph−X) and an acrylate; L = ligand.

The successful functionalization of the Pd–*m*Si nanohybrid with PEG provides the dispersibility for the overall nanocatalyst in a PEG matrix. Due to its lack of toxicity and its simple recovery, caused by its melting point at ~50 °C, PEG is considered as a "green" reaction medium.[218–221] It has already been shown that PEG can act as suitable solvent for both homogeneous and heterogeneous catalysis.[221–223] Consequently, further experiments were performed using only the Pd–*m*Si nanohybrid functionalized with PEG-silane having an average molecular weight of $M_n = 5{,}000\,\mathrm{g\,mol^{-1}}$ (PEG-5k). For catalytic reactions, Pd–*m*Si–PEG-5k was dispersed in a PEG matrix (PEG-2000, $M_n = 2{,}000\,\mathrm{g\,mol^{-1}}$) and charged into a Teflon centrifuge tube. For a detailed description of the procedure see Experimental Section 8.

A Heck-reaction was chosen as model reaction to investigate the catalytic

activity of the Pd–*m*Si nanocatalyst. Here, the C−C-coupling reaction occurs between an aryl halide and an acrylate (see Scheme 3.3).[224] In particular, the reaction between *p*-iodoanisole and ethyl acrylate appeared very auspicious since it has already been conducted in presence of PEG-2000 giving high yields of the product ethyl *p*-methoxycinnamate.[222]
Generally, Heck-reaction yields are highly dependent on the base used to support the reductive elimination of the proton and the halide-anion (see Scheme 3.3). Sodium or potassium carbonates, phosphates or acetates are typically applied in such C–C-coupling reactions. Consequently, the first step towards a successful usage of the Pd–*m*Si nanocatalyst was to find a suitable base. All reactions were conducted under the same conditions at 110 °C for 24 h and with the same amount of Pd–*m*Si–PEG-5k (4.4 mol-% with respect to palladium, determined by ICP-MS). For a detailed description of the procedure see Experimental Section 8. A major advantages of the overall approach applied in this work relies in the absence any chromatographic purification steps. Diethyl ether is used to extract the product out of the PEG matrix and is removed under mild condition *in vacuo*. Afterwards, the product was directly measured by NMR. The results of the obtained product yields are shown in Table 3.1.

Tab. 3.1: Results of the obtained yield after conducting the Heck-reaction between *p*-iodoanisole and ethyl acrylate using different bases.

Base	K_2CO_3	K_3PO_4	Na_2CO_3	Na_3PO_4
$^{\alpha}$Yield /%	47	59	99	98

$^{\alpha}$ Yield of ethyl *p*-methoxycinnamate was determined by NMR and gravimetry.

In general, the results show that the Pd–*m*Si–PEG-5k nanohybrid is able to conduct catalyses revealing that the mesoporous shell can be penetrated by the educts and the bases. Since sodium bases have shown to be superior when compared to their potassium counterparts, further experiments were conducted with Na_2CO_3 and Na_3PO_4, only. Figure 3.7 **(a)** shows the ^{1}H-NMR spectrum of ethyl *p*-methoxycinnamate and its assignment to the chemical structure after conducting the reaction with Na_3PO_4 as base. Even though no chromatographic purification was applied the product is of highest purity. Only little amounts (< 1 weight-%) of the solvent PEG are present (identified

by the signal at ~3.6 ppm). In addition, Figure 3.7 **(b)** reveals that nearly no educts are detected.

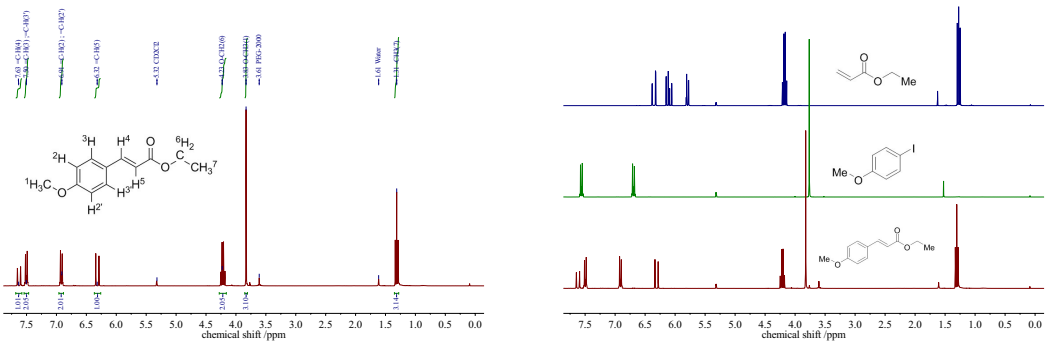

(a) **(b)**

Fig. 3.7: **(a)** Assignment of ^{1}H-NMR signals to the chemical structure of ethyl *p*-methoxycinnamate after conducting the reaction with Na_3PO_4 **(b)** ^{1}H-NMR spectrum of ethyl *p*-methoxycinnamate (red) and the educts *p*-iodoanisole (green) and ethyl acrylate (blue).

3.3.2 Recycling of the Pd–*m*Si Nanocatalyst

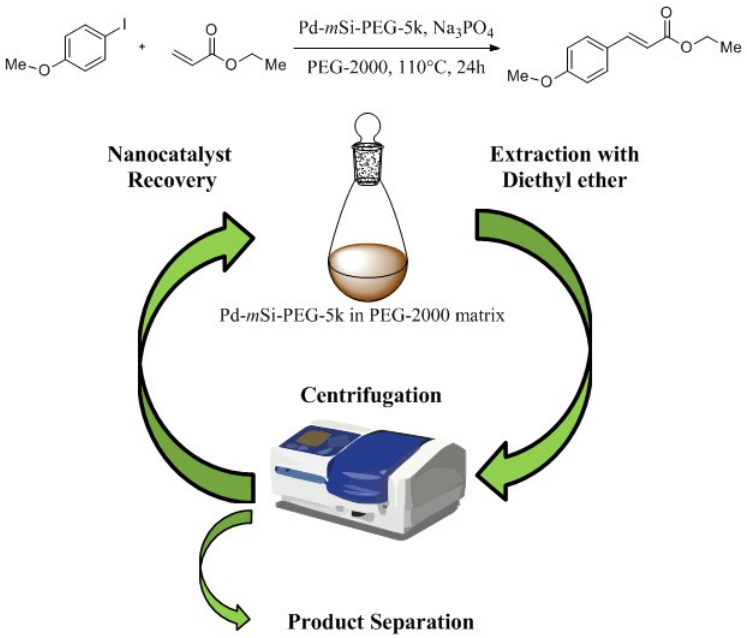

Scheme 3.4: Recycling process of the Pd–*m*Si–PEG-5k nanocatalyst and PEG-2000 as solvent after the Heck-reaction between ethyl acrylate and *p*-iodoanisole to form ethyl *p*-methoxycinnamate.

Since Na_3PO_4 and Na_2CO_3 worked best in combination with the designed nanocatalyst and the PEG matrix multiple Heck-cycles were applied using these two bases. The recycling strategy is displayed in Scheme 3.4. Teflon tubes served as both reaction and purification container which avoids an additional transfer step and prevents any losses of the nanocatalyst between reaction cycles. After the respective reaction cycle was performed the reaction medium was washed with diethyl ether to extract the product. The solution was filtered through a PTFE-filter (pore size: 0.45 µm) and Et_2O was removed *in vacuo*. For a detailed description see Experimental Section 8. Afterwards, both the nanocatalyst and the reaction medium could be recovered and subjected to further reaction–recovery-cycles. The results of the obtained yields after conducting multiple Heck-reactions are displayed in Figure 3.8 **(a)**. Data show that the sodium phosphate shows no decrease in catalytic activity (yields always $\geq 94\,\%$) over eight reaction cycles while at sodium carbonate yields

begin to drop after the 3rd cycle. In Figure 3.8 **(b)** the ^{1}H-NMR spectra of ethyl *p*-methoxycinnamate after each respective cycle are displayed for reactions using Na_3PO_4 as base. Along the eight Heck-reactions only small traces of *p*-iodoanisole (identified by the signal at ~6.75 ppm) were still present (see spectrum 5−7) while ethyl acrylate could be fully removed *in vacuo*.

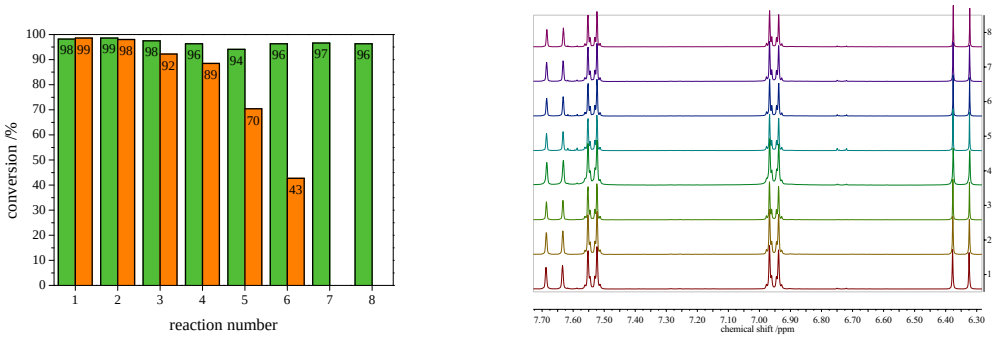

(a) **(b)**

Fig. 3.8: **(a)** Yields of ethyl *p*-methoxycinnamate obtained *via* NMR and gravimetry after each respective Heck-reaction (1-8) using Na_2CO_3 (orange) and Na_3PO_4 (green). **(b)** ^{1}H-NMR spectra of ethyl *p*-methoxycinnamate along the eight Heck-reaction cycles using Na_3PO_4 as base.

In addition, inductively coupled plasma mass spectrometry (ICP-MS) measurements of the catalytic product were conducted to determine the palladium content leached out of the catalytic system. The results reveal that leaching is strongly suppressed (see Table 3.2). The overall Pd-content in the product (~115 mg) ranges from 0.3 – 5.7 ng which corresponds to 0.002 – 0.044 ppm palladium. The ICP-MS results are in good agreement with the high product yields along the eight Heck-reactions.

Tab. 3.2: Results of ICP-MS measurements to determine the Pd-content within the extracted catalysis product. The values in brackets correspond to the mass of palladium with respect to the overall product mass.

Heck-reaction	Pd-content /ng	Pd-content /ppm
1.	5.1	0.044
2.	5.0	0.038
3.	4.2	0.032
4.	1.5	0.012
5.	5.7	0.044
6.	1.7	0.013
7.	1.6	0.014
8.	0.3	0.002

To trace the evolution of the nanocatalyst along the cycles, TE micrographs were taken after the 1st and the 8th Heck-cycle (see Figure 3.9). It can be seen that the cubical structure of the palladium-core vanishes during the first reaction (left TEM image). Inside the silica shell spherical palladium particles were formed. An explanation for this rearrangement lies in the suggested Heck-mechanism (see Scheme 3.3).[224] Here, a Pd^{II+}-species forms after the oxidative addition of the *p*-iodoanisole which can desorb from the PdNCube.

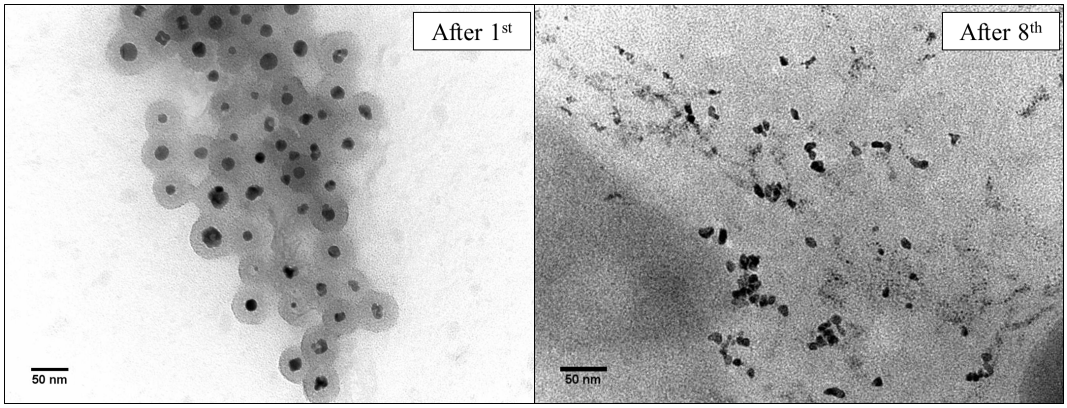

Fig. 3.9: TE micrographs of the Pd–*m*Si–PEG-5k nanocatalyst taken after the 1st (left) and the 8th Heck-reaction (right).

Once the reductive elimination of the proton and the bromide-ion occurs the Pd^0-species is generated again that can re-deposit on the palladium-core.[207] Since the spherical geometry possesses the lowest free surface energy, globules were eventually formed.[28] The mesoporous silica shell is not affected significantly by the catalysis and the rearrangement of the palladium. The porosity appears to stay intact, enabling the penetration of further small organic molecules. Control experiments were performed to validate whether these observations are based on either a thermally or a chemically induced rearrangement process of the palladium core. Therefore, only the nanocatalyst was dispersed in PEG-2000 and heated at 110 °C for 24 h without any conducted catalysis reaction.

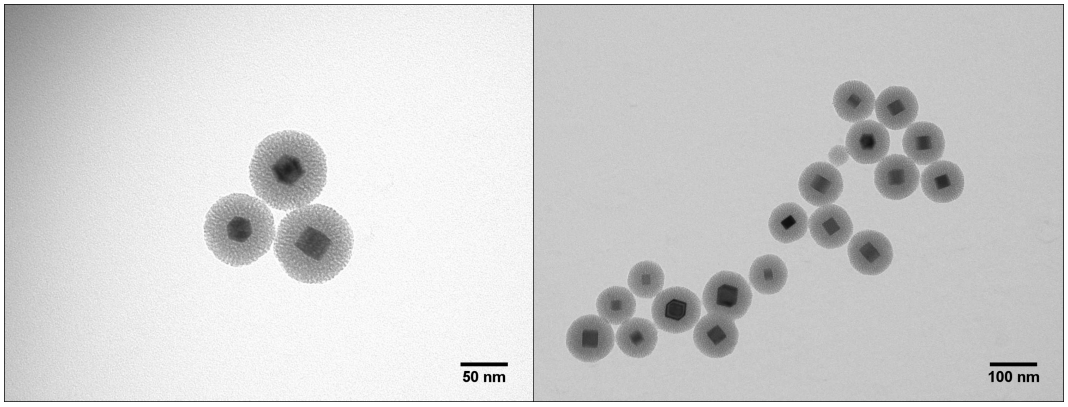

Fig. 3.10: TE micrographs taken after conducting control experiments heating the Pd–*m*Si–PEG-5k nanocatalyst at 110 °C for 24 h without any conducted catalysis reaction.

TEM results showed no changes in the structure of neither the palladium-core nor the silica shell (see Figure 3.10). After the 8^{th} reaction, no core–shell nanostructures could be detected anymore *via* TEM. Only small randomly shaped Pd nanoparticles (≤ 20 nm) were found indicating a slow leaching of the palladium out of the silica shell. However, no larger aggregates were formed (see right TE micrograph in Figure 3.9) which explains the continuously high catalytic activity.

3.4 Summary and Conclusion

In this part of the work, an efficient design strategy to obtain a highly active, heterogeneous palladium nanocatalyst protected by a mesoporous silica shell is presented. This core–shell nanohybrid revealed an outstanding stability over at least several months in the presence of both water and air. During catalysis the *m*Si-shell showed sufficient permeability for organic molecules and thermal stability at elevated temperatures. It could be demonstrated that both the catalyst and the solvent can be easily recycled after Heck-reactions and subjected to further reaction–recovery-cycles without any significant decrease in catalytic activity. The newly developed approach offers various advantages over other catalytic systems: 1st the highly step-efficient and simple fabrication process of both the Pd-catalyst and its shell, 2nd the absence of expensive and toxic ligands and solvents, 3rd the full recyclability of the nanocatalyst and the reaction medium and 4th the facile isolation of the product without further need of chromatographic purification to receive excellent product purities. Consequently, this work may contribute substantially to a more sustainable usage of limited resources.

4 Palladium Nanohybrids as Model System for Potential Hydrogen Storage Applications

This chapter is based on the collaboration between the *Pundt*-group from the Karlsruhe Institute of Technology (KIT) and the *Vana*-group from the University of Goettingen. The task of the author was to provide different palladium nanohybrids which shall be investigated by the collaborators regarding its application as potential hydrogen storage material. Experiments are still ongoing and final results are not yet published prior to the submission deadline of this thesis.

4.1 Introduction and State of the Art

The usage of "clean" hydrogen in areas such as the automotive sector[225] or the "green"-steel[226] production plays a crucial role towards a climate-neutral industry. Due to its high energy density and light weight it is also an interesting candidate for temporary energy storage at off-peak times of overproduction from wind power plants or solar cells.[227,228] In that matter, the storage of produced hydrogen is of highest importance. Up to now, it is stored in compressed gas tanks, as liquid and as solid state hydrids. However, there are still challenges for an adequate storage of H_2, especially when it comes to on-board applications in vehicles.[229,230] The major obstacle for solid state hydrids is to combine high capacities (high mass ratio of H_2) and a low decomposition temperature to ensure practical release conditions.[227] Current representatives of this class are metal hydrides, complex hydrides and nonmetal hydrides.[231] Among them, transition metal hydrids bear the advantage of absorbing and desorbing H_2 reversibly under relatively mild conditions.

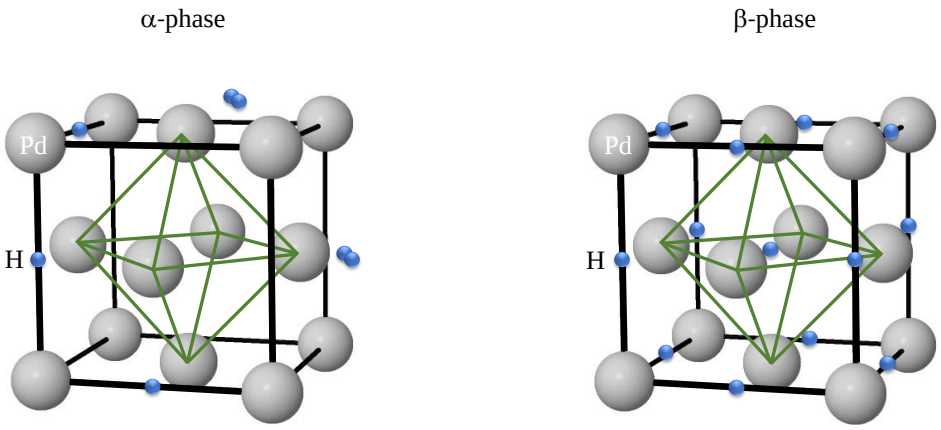

Fig. 4.1: Fcc lattice of palladium and the two different phases of the Pd–H-system: the solid solution α-phase and the metal hydride β-phase. Lattice expansion due to hydrogen uptake within the β-phase is not displayed.

In this context, palladium shows a high affinity towards hydrogen caused by its advantageous absorbing and catalytic properties.[227] Especially nanosized Pd possesses unique features such as enhanced absorption/desorption kinetics and size/shape tunable thermodynamics opposed to its bulk counterpart.[232–234] If H_2 comes in contact with palladium, it dissociates into atomic hydrogen on the Pd surface. Subsequently, these H-atoms diffuse into Pd lattice and occupy interstitial sites of the fcc lattice.[231] Depending on the hydrogen pressure and the temperature two phases within the Pd–H-system can arise (see Figure 4.1): at low concentrations (PdH_x with $x < 0.03$) a solid solution phase appears called the α-phase, whereas at elevated concentrations (PdH_x with $x > 0.03$) a metal hydride phase called the β-phase occurs. Consequently, the latter mainly determines the ability to store H_2. Along the increasing hydrogen uptake within the β-phase, a large lattice expansion arises during that process caused by its distortion. Considering nanosized crystals or films deposited onto rigid substrates, in-plane stresses (several GPa) at the interface may occur leading to changes in the thermodynamics of the Pd–H system. This may also shift the equilibrium pressures regarding the transition between α- and β-phase which

is in general of first-order and takes place at a plateau-pressure.[235,236]
As mentioned before, both physical and chemical properties with respect to hydrogen storage ability of nanosized palladium are dependent on its shape and size. *Takata et al.* investigated PdNPs of 2.6 and 7.0 nm size compared to bulk Pd.[234] They showed that with decreasing NP size H_2 solubility increases within the α-phase but the storage capacity within the β-phase decreases. These properties are closely related to the electronic states of nanosized Pd an Pd–H, respectively. Even though the electronic configuration of Pd is $[Kr]4d^{10}5s^0$, the 4d band is not fully filled and the Fermi-level is located at he 4d band caused by an overlap of 4d and 5s bands.[231,234] Accordingly, the α-phase can be described electronically by the band structure of pure Pd whereas in Pd–H (β-phase) a chemical bond with bonding and antibonding bands below and above the 4d band are present. Therefore, from the electronical perspective the α- and β-phase have to be considered separately. As a result the Fermi-level gradually shifts towards the 5s band along an increasing hydrogen uptake in Pd–H. Since the formation of Pd–H within the β-phase is associated with an electron filling into the 4d band, hydrogen storage capacity can be tuned by controlling the number of 4d band holes. One approach to achieve this relies in metal-alloying with elements carrying either more (Ag)[237] or less (Rh)[238] electrons than pure Pd. Consequently, hydrogen storage capacity is reduced ($Pd_{1-x}Ag_x$) or enhanced ($Pd_{1-x}Rh_x$) compared to pure Pd, respectively. *Kubota et al.* conducted X-ray absorption near-edge structure spectroscopy (XANES) measurements of PdNPs with different sizes in absence and in presence of H_2.[239] A decrease in Pd size was connected to a decrease in the electron density of d-states of Pd–H near the Fermi-level. *Zhou et al.* analyzed various sizes of PdNPs by X-ray photoelectron spectroscopy (XPS). They found a downshift of the valence band with respect to the Fermi-Level of PdNPs with decreasing size.[240] Both observations suggest that the 4d band of pure Pd is more filled in smaller NPs.[231]
Therefore, it appears highly favorable to fabricate larger palladium nanoparticles which should yield in a less filled 4d band and therefore a higher H_2 uptake within the β-phase. In this context, experimental techniques for single-particle tracking within an environmental transmission electron microscope (ETEM) were established just recently. Here, individual particles can be observed while H_2 is introduced *in situ*.[241] Simultaneously, other techniques such as electron

energy loss spectroscopy (EELS) or electron/X-ray diffraction can be applied and pressures up to the atmospheric range are feasible which in combination offers a detailed insight into solid–gas interactions under realistic conditions. [242]

4.2 Fabrication of Palladium Nanohybrids

4.2.1 Seed-Mediated Growth Towards Larger Palladium Nanocubes

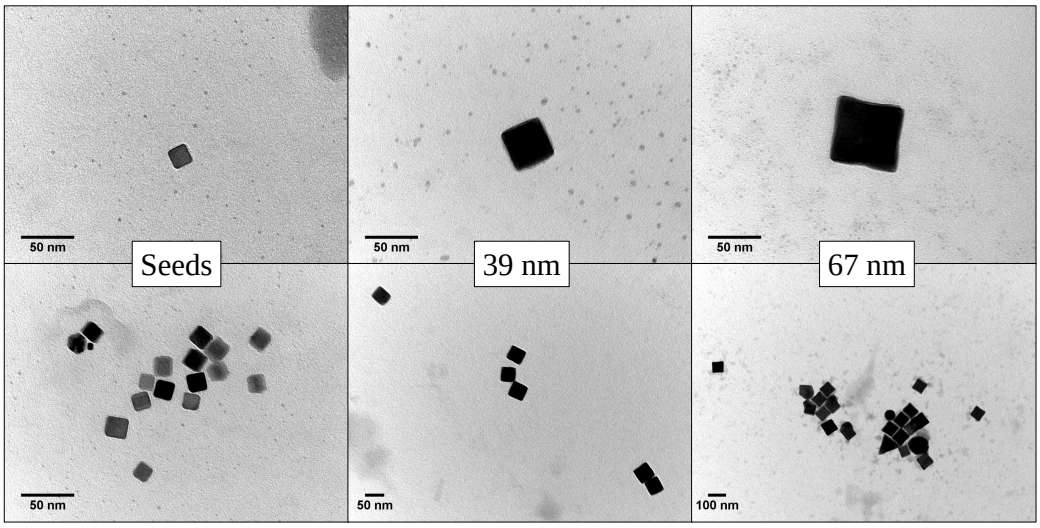

Fig. 4.2: TE micrographs of CTAB-capped seed, 39 nm and 67 nm PdNCubes. The upper three images have the same magnification which clearly visualizes the successful seed-mediated growth.

The fabrication of of 18 nm palladium nanocubes has already been described in Chapter 3. Generally, H_2PdCl_4 was reduced by ascorbic acid in aqueous solution in presence of cetyltrimethylammoniumbromide (CTAB) as surfactant. According to *Xu et al.* these nanocubes can serve as seeds to obtain even larger PdNCubes. [32,58] This seed-mediated growth process offers better control over size and shape than a seedless growth approach and delivers a more uniform size distribution. Hereby, the size can be tuned by the ratio between seed- and feed

solution. For a detailed description of the procedures see Experimental Section 8. Similar to the fabrication of 18 nm seeds the seed-mediated growth processes were upscaled by 10 times for a better handling. Exemplary TE micrographs of the Pd-seeds and two respective samples from a seed-mediated growth are depicted in Figure 4.2. By adjusting the seed-to-feed ratio PdNCubes with edge lengths of 39 ± 4 nm and 67 ± 7 nm were obtained with good size control (standard deviation $\sim 11\%$). The respective histograms of seeds, 39 nm and 67 nm PdNCubes are depicted in Figure 4.3.

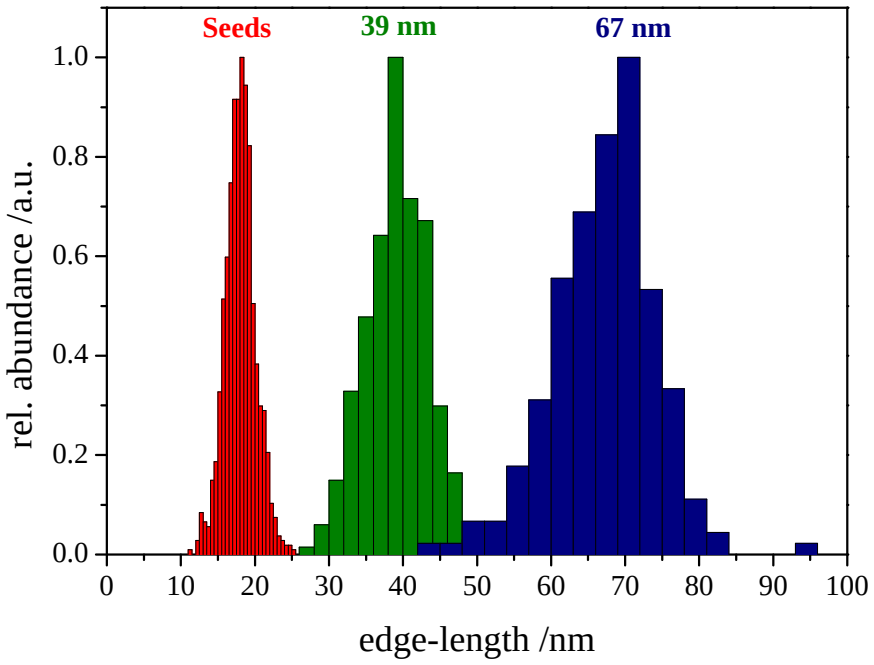

Fig. 4.3: Histograms of the Pd edge length distributions of seeds (red), 39 nm (green) and 67 nm (blue) NCubes obtained by evaluating multiple TE migrographs of PdNCubes.

4.2.2 Functionalization of Palladium Nanocube Surfaces

To ensure a prolonged stability of palladium nanocubes and improve its handling, exchanging CTAB with a synthetic polymer is an effective approach. For instance, sols of CTAB-capped NCs are known to become unstable after the

addition of ethanol since CTAB is highly soluble in ethanol.[211] Opposed to that, polymers which were grafted to NC surfaces over a covalently bonding anchor group overcome that limitation.[21,67,170,243] There were certain requirements for a polymer to be suitable for further experiments: the polymer should possess at least one strong anchor group to attach the polymer to the Pd-surface and give a nanothin, uniform and stable shell to ensure an adequate and homogeneous permeability of H_2 towards the metal surface. Furthermore, it must not react with hydrogen and should be soluble in various volatile and non-toxic solvents to facilitate the handling with polymer-grafted PdNCubes.

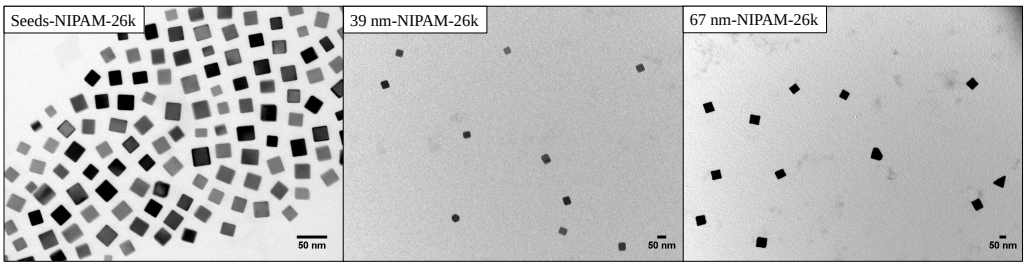

Fig. 4.4: TE micrographs of different PdNCubes functionalized with the RAFT-polymer NIPAM-26k.

In that matter, poly(*N*-isopropyl acrylamide) (poly(NIPAM)) fabricated *via* the reversible addition–fragmentation chain transfer (RAFT) polymerization is a suitable candidate to fulfill all these demands. *Rohleder* showed that NIPAM RAFT-polymers can be successfully immobilized onto 18 nm PdNCube surfaces *via* a grafting-to approach.[21] Here, the inherent trithiocarbonate group of RAFT-polymers served as anchor group to attach the polymer to the palladium nanocube. By variation of the average polymer chain length, the size of the polymer shell could be tuned between 11 and 100 nm. To ensure uniform conditions for further experiments and comparability between all three PdNCubes of different sizes, the same polymer was used. Therefore, the NIPAM RAFT-polymer NIPAM-26k with an average molecular weight M_n =26 kg mol^{-1} and a dispersity $Đ = 1.07$ was applied to further surface functionalization experiments. The detailed description of the polymer synthesis conditions is given in Chapter 5 and in the Experimental Section 8. The functionalization of different PdNCubes was conducted according to previous protocols by solving the polymer in nanopure water and ethanol, respectively. This polymer

solutions were given to the Pd-sol under ultrasonication and incubated over night. The procedure and purification is further specified in the Experimental Section 8. After three centrifugation and redispersion cycles to remove residual polymer, Pd nanohybrids were dispersed in ethanol to yield concentrations of $\sim 0.6\,\mathrm{mg\,ml^{-1}}$. For a successful functionalization it is crucial to establish suitable centrifugation conditions. If the *g*-force was chosen too high aggregates were formed which is particularly important for larger and therefore heavier PdNCubes. The respective details can be found in the Experimental Section 8. Once adequate purification conditions were established samples were analyzed *via* TEM (see Figure 4.4). Interestingly, only for the 18 nm palladium seeds a well defined nanopattern of PdNCubes with defined spacings could be observed. For the 39 nm and 67 nm PdNCube the polymer shell is not able to assembly the nanohybrids into well ordered 2D arrays.

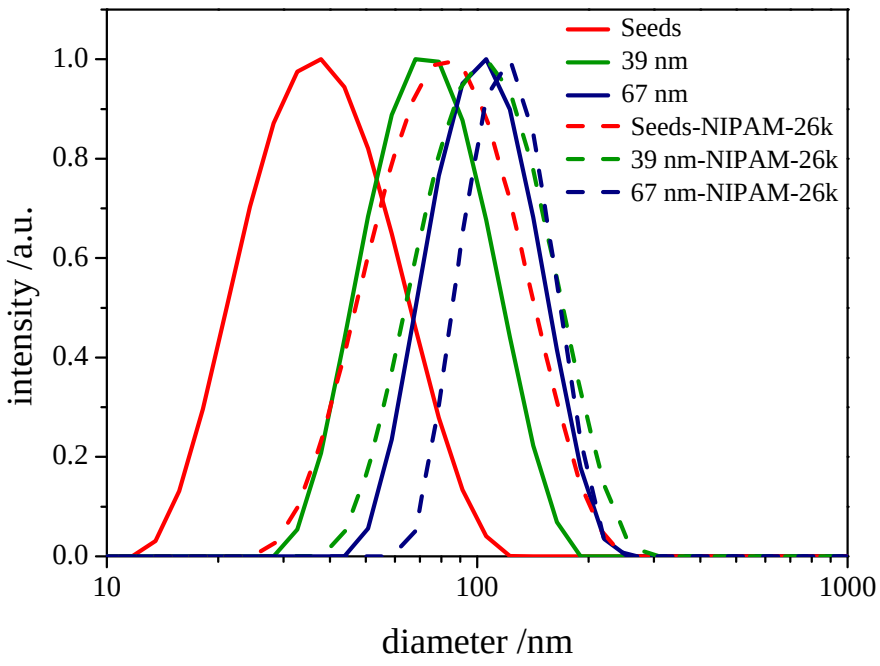

Fig. 4.5: DLS distributions of different CTAB-capped PdNCubes (bold lines) measured in water and PdNCubes functionalized with NIPAM-26k (dotted lines) measured in ethanol at 25 °C.

However, the successful functionalization could be verified by its dispersibility. Without NIPAM-26k on the nanocube surface, PdNCubes were not dispersable in ethanol even under the aid of ultrasonication without the formation of higher aggregates. This would have led to a black sol whereas the color of the nanohybrids remained brown along the purification steps. Further evidence regarding the successful functionalization was obtained by dynamic light scattering (DLS) experiments. In Figure 4.5 diameters of the three different CTAB-capped PdNCubes were compared to the three different polymer-grafted PdNCubes. In addition to Figure 4.2 this clearly shows that the seed-mediated growth was successful. Furthermore, it can be seen that the functionalization led to in an increase in hydrodynamic diameter for all three samples with no larger aggregates present.

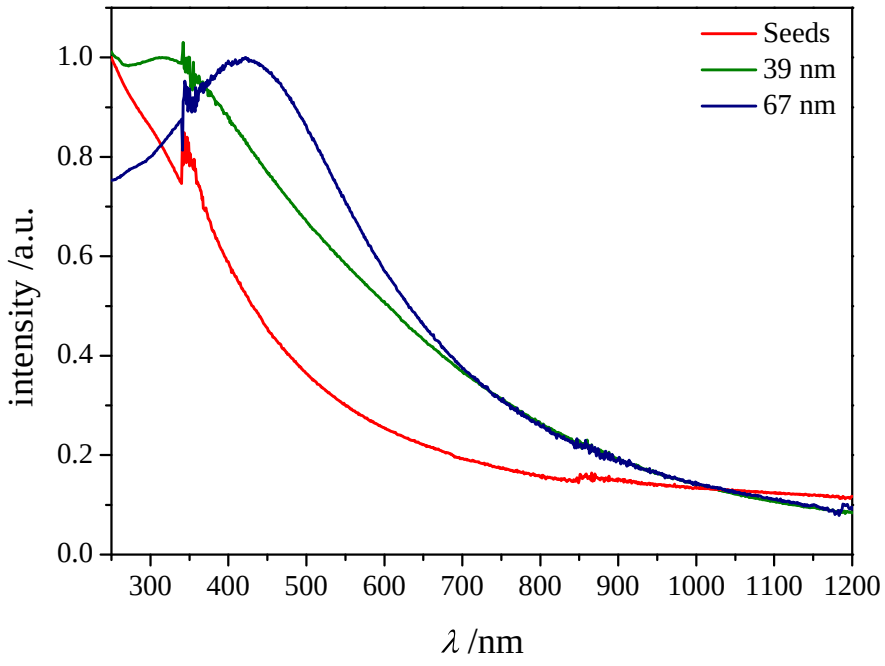

Fig. 4.6: UV/vis spectra of different PdNCubes functionalized with NIPAM-26k (EtOH) in the range between 250 nm and 1200 nm obtained at room temperature. At 360 nm change of light source was conducted.

As mentioned above the size of PdNCubes has a major influence on the

electronic properties and therefore arguably on the ability to store H_2. In this regard, UV/vis spectroscopy can give initial information over surface plasmon resonances of nanocrystals and thus over their electronic states (see Section 2.1.2.3). The respective spectra of the three different nanohybrid samples are displayed in Figure 4.6. It can be seen that by increasing the size of PdNCubes from 18 nm, over 39 nm to 67 nm the surface plasmon resonance peak red-shifts from ~300 nm (small shoulder), over ~320 nm to ~425 nm. These results agree well with results presented in literature.[58]

4.3 Summary and Conclusion

In this chapter, palladium nanocubes with edge lengths between 18 nm and 67 nm were fabricated. Therefore, a seed-mediated-growth process was applied using the 18 nm NCubes as seeds. A NIPAM RAFT-polymer was immobilized onto these PdNCubes *via* a grafting-to approach to ensure the nanocube stability, prevent aggregation and improve the handling for further analyses. The successful functionalization was validated by transmission electron microscopy (TEM) and dynamic light scattering (DLS) techniques. Along the increase in nanocube edge length a change of the electronic properties could be observed *via* UV/vis spectroscopy by a red-shift in the surface plasmon resonance peak. Hence, the fabricated nanohybrids are highly suitable candidates for further investigations towards hydrogen storage applications. Analyses by the *Pundt*-group from the KIT are still needed to get a detailed picture of the size dependent properties of these materials. Here, individual polymer-grafted Pd nanocubes shall be investigated *in situ* upon hydrogen exposure regarding its interaction with H_2 in an environmental TEM at atmospheric pressures. The influence of the size and shape of Pd nanocubes on the substrate-induced stress and on the phase transition behavior in general is of special interest. This is matter of ongoing research and therefore not within the scope of this thesis.

5 Nanopatterning of Polymer-Grafted Gold Nanorods

5.1 Introduction and State of the Art

Highly ordered, periodic nanoarrrays of plasmonic nanocrystals offer an outstanding potential for various applications such as plasmon rulers,[79] biological sensing[80,81] or surface-enhanced Raman spectroscopy (SERS).[57,82,83] Typically, two different approaches can be applied to fabricate such nanopatterns (see Chapter 2). The top-down strategy including nanolithography, nanoimprint or deposition techniques is a widely studied field and finds applications in industry for micro-chip, micro-electro–mechanical system or micro-mirror fabrication.[37–39] However, surface roughness, polycrystallinity of the nanocrystals, area throughput and equipment (-maintenance) costs limit their range of large scale applications. The usage of colloidal nanocrystals overcomes most of these obstacles due to its scalability, single-crystallinity and therefore smoother surfaces within the atomic length scale. Additionally, these wet-chemistry approaches give rise to tunable dimensions and geometries by facile adjustment of the fabrication conditions (see Chapter 2). Through various surface modification and deposition techniques surface patterning can also be achieved using nanocrystals obtained from a bottom-up approach.
Especially noble-metal nanorods are of great interest due to their tunable optical properties. Depending on the aspect ratio NRs show two distinct LSPRs (longitidunal and transverse) which gives rise to various SERS applications in low-dosage molecule detection or process monitoring on the nanoscale.[244] *Murphy et al.* were able to show that SERS activity is significantly enhanced by a factor up to 100 if the plasmon band of gold and silver nanorods overlaps with the excitation source wavelength.[82] This is caused by greater contributions from the electromagnetic enhancement mechanism. Another factor affecting the SERS intensity is the size of nanocrystals. *Ren et al.* demonstrated both

experimentally and theoretically that smaller AuNRs possess a higher SERS activity due to a stronger local field enhancement.[83]
Besides the intrinsically given properties of individual NRs, plasmonic coupling between at least two NRs can alter their optical characteristics and therefore their SERS activity.[244,245] Due to the coupling a shift $\Delta\lambda_{\mathrm{LSPR}}$ occurs with respect to the LSPR λ_{LSPR} for an isolated NR. The general Equation 5.1 is valid for several NC geometries:[114,116]

$$\frac{\Delta\lambda_{\mathrm{LSPR}}}{\lambda_{\mathrm{LSPR}}} = A\, e^{-\frac{s}{D}\frac{1}{\tau}} \tag{5.1}$$

Here, s symbolizes the center of mass distance between two nanorods, D the physical size, τ the exponential decay length and A the pre-exponential factor. *El-Sayed*-group investigated not only the distance dependence but also the influence of the orientation θ on the plasmonic field coupling of two gold nanorods both experimentally and theoretically by discrete dipole approximation (DDA) simulations. Besides a $\cos^2\theta$ orientation dependence, a decay length of $\tau = 0.22$ with respect to the rod length was found. For AuNRs with a length of $\sim 40\,\mathrm{nm}$ spacings of $\sim 9\,\mathrm{nm}$ or lower are of greater interest regarding near-field enhancements.[116] These factors led to the conclusion that tunable nanoarrays of small gold nanorods might have a great potential as SERS substrates or as coated tips for tip-enhanced Raman spectroscopy (TERS). So far, 2D arrays with tunable distances of AuNRs were only fabricated by lithographic techniques or under the aid of prefabricated surfaces or matrices and by controlling the Debye length of AuNRs.[79,116,211,246–248] The fabrication of polymer-grafted gold nanorods with tunable shell thicknesses and therefore adjustable interparticle distances appears to be a much more straightforward, versatile and predictable appraoch compared to other studies. Additionally, polymer-grafted AuNRs should be more robust and thus less affected by environmental factors such as temperature, solvent quality and impurities.

5.2 Fabrication of CTAB-capped Gold Nanorods

Generally, CTAB-capped AuNR are synthesized *via* a seed-mediated growth process.[78,90,249,250] The mechanism of the formation of AuNR in aqueous solution along with the role of CTAB and silver-ions is discussed in literature intensivly (see Chapter 2).[82]
In this work, AuNRs were synthesized *via* a seedless fabrication process reported by *ElSayed et al.*[89] and *Chen et al.*[87] These protocols were adapted to obtain a 10-fold upscaling. For a detailed description of the procedure see the Experimental Section 8. After three centrifugation–redispersion cycles the applied fabrication yielded small AuNRs with a length of (34 ± 5) nm and a diameter of (8.2 ± 1.1) nm. The respective TE micrograph and histogram of the as-obtained AuNRs are displayed in Figure 5.1.

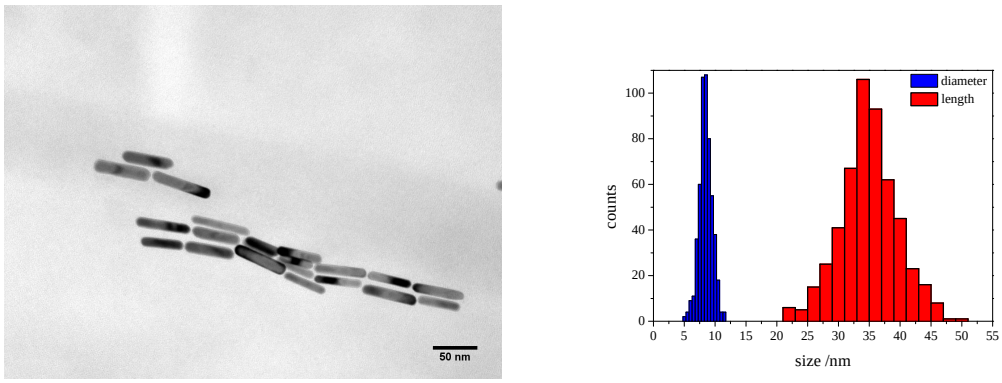

(a) **(b)**

Fig. 5.1: **(a)** Exemplary TE micrograph and **(b)** histogram of of CTAB-capped AuNRs after three centrifugation–redispersion cycles.

The TEM results (aspect ratio (AR) = 4.1) agree perfectly with results obtained *via* UV/vis (see Figure 5.2 **(a)**). The longitidunal LSPR band was found at ~810 nm which corresponds to an AR of 4.1 (according to the Equation 5.2 provided by *ElSayed et al.*:[77]

$$\lambda_{\text{long}} = 420 + 95\,\text{AR} \tag{5.2}$$

CTAB-capped AuNRs were further characterized by dynamic light scattering (DLS) measurements in aqueous solution (see Figure 5.2 **(b)**). Here, two distinct peaks can be observed in the intensity distribution diagram. The peak at ~40 nm corresponds to the hydrodynamic diameter of the AuNRs and therefore, to the translational diffusion. Due to the anisotropy of the NR a second peak at ~3 nm can be observed. This pseudo-peak is caused by the rotational diffusion of the AuNR and cannot be translated into a hydrodynamic diameter.

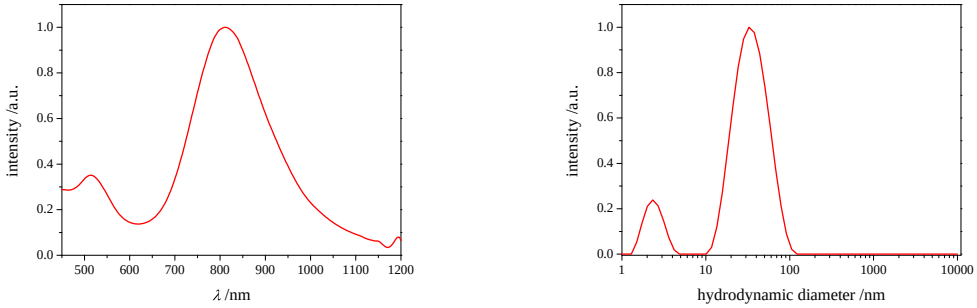

(a) **(b)**

Fig. 5.2: **(a)** UV/vis spectrum and **(b)** DLS results of of CTAB-capped AuNRs in nanopure water at 25 °C.

5.3 Polymerizations Using the RAFT-Process

In the following section the synthetic route to obtain macromolecular material for further experiments is presented. Polymers were fabricated using the RAFT-process (see Chapter 2) which offers great control over the average molecular weight (M_n) along with low dispersities ($Đ < 1.3$). RAFT-agents were equipped with either one or three branched trithiocarbonate (TTC) functionalities which yielded linear or 3-arm star-polymers, respectively.
The use of NIPAM containing RAFT-polymers in nanoparticle functionalization has been studied extensively over the past ten years.[12,14,16,17,19,67] Due to its adequate solubility in both various organic solvents and water poly(NIPAM) is favorable for NP-functionalization approaches. Generally, poly(NIPAM) is considered as smart polymer due to its lower critical solution temperature

(LCST) in water at 32 °C ($M_n > 10^4\,g\,mol^{-1}$).[178,179]
The decoration of AuNRs with NIPAM-containing polymers was reported in literature already. In the approach of *Niidome et al.* AuNRs undergo a multistep functionalization process to yield a NIPAM-shell on the gold surface.[251,252] Accordingly, gold nanorods have to be pre-functionalized with PEG-SH first followed by a silica-coating and their functionalization with a silane-coupling agent. The NIPAM-network can be immobilized on the AuNRs using a crosslinker while the silica coating was etched away afterwards. In the appraoch of *Shen et al.* AuNRs were pre-functionalized with an ATRP-initiator followed by a grafting-from polymerization with NIPAM.[165]. Up to now, no grafting-to functionalization of gold nanorods using NIPAM-containing RAFT-polymers has been reported. Since the grafting-to approach is used in this work, AuNRs and the respective RAFT-polymers can be characterized separately from each other. Additionally, this approach offers further advantages such as step-efficiency and scalability compared with a grafting-from approach.

5.3.1 Fabrication of Linear NIPAM Homopolymers

To provide linear NIPAM RAFT-polymers containing one TTC group at the end of the polymeric chain, methyl-2-(((dodecylthio)carbonothioyl)thio)propanoate (l-CTA, see Figure 5.3) was used as RAFT-agent. Polymerizations were conducted in 1,4-dioxane at 60 °C using 1,1'-azobis(isobutyronitrile) (AIBN) as initiator. For a detailed description of the synthetic procedure see Experimental Section 8. The molecular weight was tuned by adjusting the monomer-to-RAFT ratio ($^{[M]}/_{[RAFT]}$). Simultaneously, the monomer-to-initiator ratio was held constant at $^{[M]}/_{[Initiator]} = 5800$. All polymers were purified by repeated precipitation (3×) in ice-cold diethyl ether. The results of the polymerization are summarized in Table 5.1. The yielded polymers reveal good control of the molecular weight distribution showing low dispersities (see Figure 5.4).

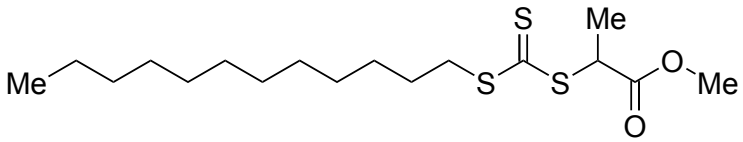

Fig. 5.3: Structure of the RAFT-agent (l-CTA) used to synthesize linear RAFT-polymers.

Tab. 5.1: Results of RAFT-polymerizations to provide linear polymers of different chain lengths for nanocrystal functionalization.

sample	$[M]/[RAFT]$ [α]	eq. of [β] 1,4-dioxane	time / h	conv. [γ] / %	$M_{n,SEC}$ / 10^3 g mol^{-1}	$Đ$
NIPAM-1	100	3	4	95	14	1.07
NIPAM-2	200	3	4	97	26	1.07
NIPAM-3	300	3	4	96	34	1.04
NIPAM-4	400	3	4	97	48	1.16
NIPAM-5	600	3	4	98	65	1.13
NIPAM-6	800	3	4	92	75	1.19
NIPAM-7	1000	3	4	93	89	1.18
NIPAM-8	1200	3	4	95	114	1.27
NIPAM-9	1400	3	4	94	134	1.36

[α] $[M]/[RAFT]$: ratio between monomer and RAFT-agent.

[β] Equivalents compared with amount of monomer.

[γ] The conversion was determined by gravimetry.

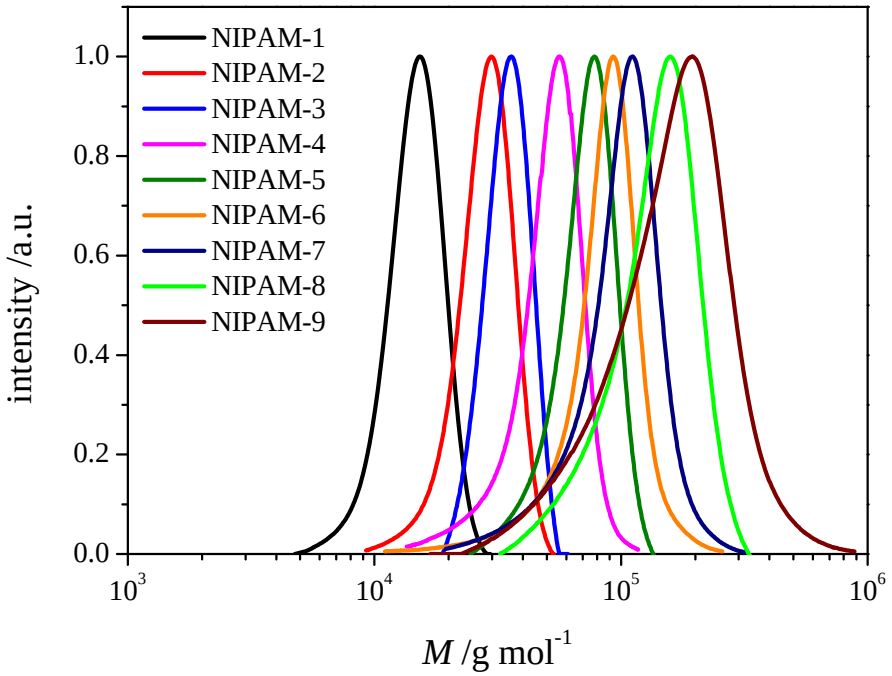

Fig. 5.4: Molecular weight distributions of different linear NIPAM RAFT-polymers.

5.3.2 Fabrication of 3-Arm Star NIPAM Homopolymers

To provide 3-arm star-RAFT-polymers containing one TTC group at the end of each arm, propane-1,2,3-triyl tris(2-(((propylthio)carbonothioyl) thio)propanoate) (star^3-RAFT, see Figure 8.4) was used as RAFT-agent. Since the leaving group (R-group) is attached to the inner core of the molecule, TTC groups remain their position on the outer sphere of the star-polymer during polymerization (R-group approach).[253] This end-group positioning is necessary for further functionalization experiments such as the grafting on metal nanocrystals.

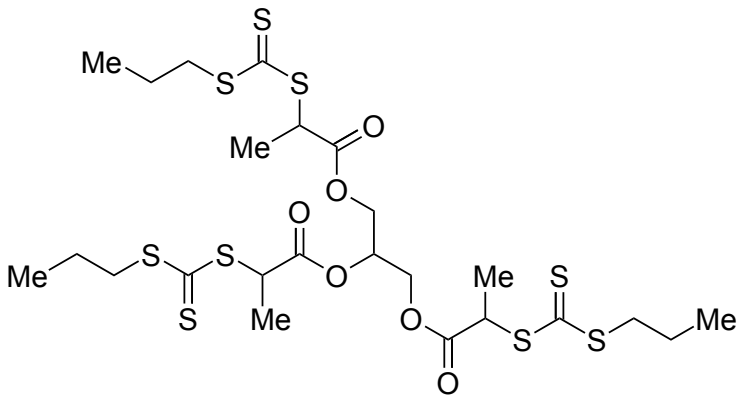

Fig. 5.5: Structure of the 3-arm star-RAFT-agent (star^3-RAFT) used to synthesize star-RAFT-polymers.

Tab. 5.2: Results of RAFT-polymerizations to provide 3-arm polymers of different chain length for nanocrystal functionalization.

sample	$^{[M]}/_{[RAFT]}$ $^{\alpha}$	eq. of dioxane $^{\beta}$	time / h	conv. $^{\gamma}$ / %	$M_{n,\mathrm{SEC}}^{\delta}$ / $10^3\,\mathrm{g\,mol^{-1}}$	$Đ$
star^3-1	350	4	4	69	35	1.07
star^3-2	450	4	4	77	51	1.07
star^3-3	600	4	4	76	71	1.07
star^3-4	900	4	4	84	100	1.08
star^3-5	2000	4	4	60	141	1.23
star^3-6	2750	4	4	60	169	1.36

$^{\alpha}$ $^{[M]}/_{[RAFT]}$: ratio between monomer and RAFT-agent.

$^{\beta}$ Equivalents compared with amount of monomer.

$^{\gamma}$ The conversion was determined by gravimetry.

$^{\delta}$ $M_{n,\mathrm{SEC}}$ values were corrected for 3-arm polymers.[254,255]

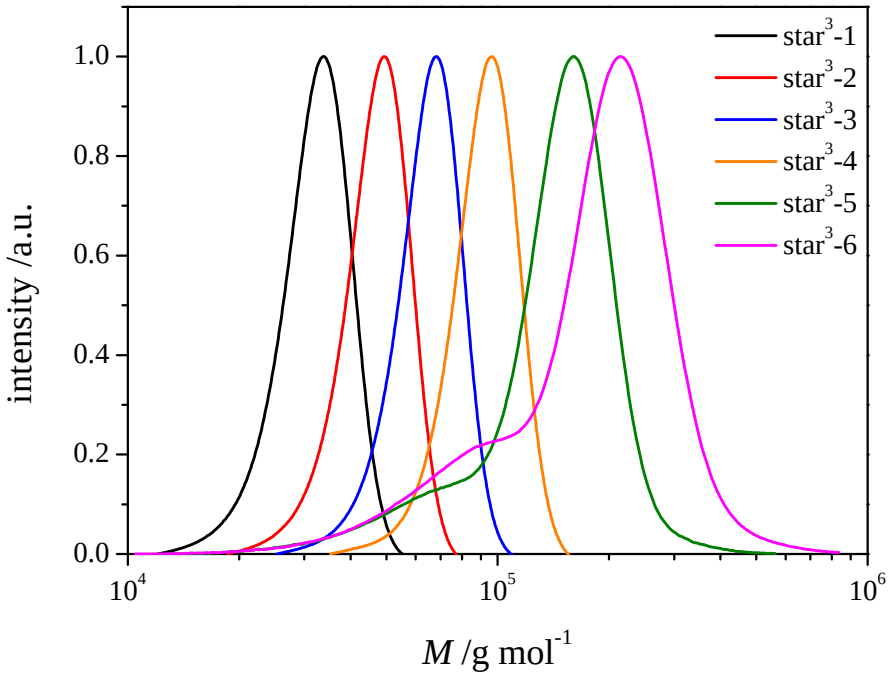

Fig. 5.6: Molecular weight distributions of different 3-arm star NIPAM RAFT-polymers.

Similar to the synthesis of the linear polymers, polymerizations were also conducted in 1,4-dioxane at 60 °C using AIBN as initiator. For a detailed description of the synthetic procedure see Experimental Section 8. Accordingly, the molecular weight was tuned by adjusting the monomer-to-RAFT ratio. The monomer-to-initiator ratio was kept constant at $^{[M]}/_{[Initiator]} = 10000$. The results of the polymerizations are shown in Table 5.2. Similar to their linear counterparts, 3-arm star polymers reveal good control of the molecular weight distribution with low dispersities (see Figure 5.6). Average molecular weight values obtained from size exclusion chromatography (SEC) were corrected using a correction factor of 1.16 for 3-arm star-polymers determined by *Boschmann* and *Vana*.[254,255] This takes into account, that the hydrodynamic radius of star-polymers is reduced, opposed to linear polymers of the same molecular weight.

5.4 Synthesis of Polymer–Metal Nanohybrids

Ebeling and *Vana* established a general strategy to functionalize spherical gold nanoparticles with NIPAM RAFT-polymer applying a grafting-to approach.[12,67] This method has been transferred to several other systems such as AgNPs,[19] PdNCubes[21] and planet–satellite structures[14] within the past years. Due to its inherent aurophilicity, TTC groups act as bidentate anchors on precious metal surfaces forming core–shell structures with tunable shell thicknesses through a variable average molecular weight of the grafted polymer.

5.4.1 Functionalization of AuNRs Using Linear NIPAM Homopolymers

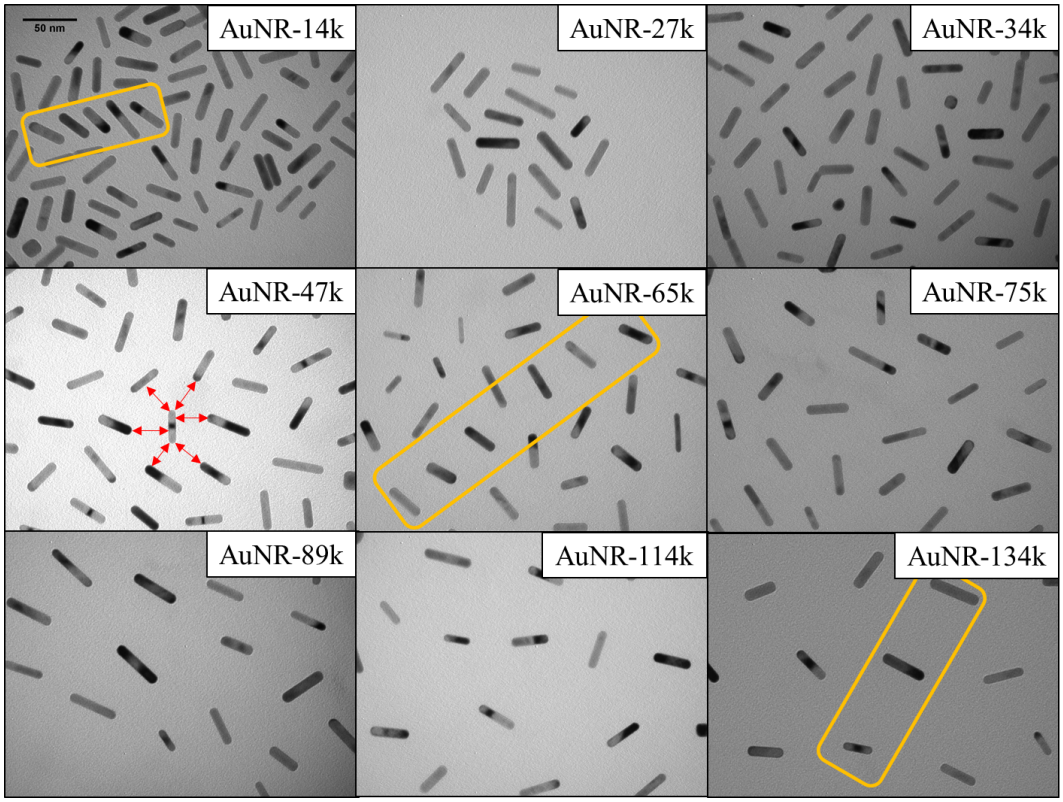

Fig. 5.7: TE micrographs of AuNRs functionalized with NIPAM RAFT-polymers with various chain lengths. Scalebar (50 nm) is valid for all micrographs.

These as-prepared CTAB-capped AuNRs were functionalized by linear RAFT-polymers of different chain lengths. In a typical experiment, the respective polymer was solved in ethanol and subsequently added to the AuNR sol under ultrasonication at room temperature. For a more detailed description see Chapter 8. Three centrifugation–redispersion cycles were conducted using ethanol to separate functionalized AuNRs from CTAB and excess polymer. Conventional poly(NIPAM) is only capable of forming weak bonds to the gold surface through its nitrogen or oxygen atom of the amide group.[256] The TTC groups are essential to offer sufficient colloidal stability over several months. After the centrifugation–redispersion steps, nanohybrids were redispersed in EtOH. For analyses with the transmission electron microscope (TEM), aliquots were drop-cast on a TEM grid with an amorphous carbon film and a copper mesh. The respective samples were subsequently covered with a glass vial to ensure a slow evaporation of the solvent. For a detailed description of the procedure see Experimental Section 8.

Tab. 5.3: Results of the TE micrograph evaluation of AuNRs functionalized with linear RAFT-polymers.

sample	polymer	$M_{n,\mathrm{SEC}}$ / $10^3\,\mathrm{g\,mol^{-1}}$	$Đ$	no. of distances	spacing / nm
AuNR-14k	NIPAM-1	14	1.07	272	9 ± 2
AuNR-26k	NIPAM-2	26	1.07	260	16 ± 3
AuNR-34k	NIPAM-3	34	1.04	477	19 ± 4
AuNR-48k	NIPAM-4	48	1.16	547	26 ± 4
AuNR-65k	NIPAM-5	65	1.13	632	31 ± 5
AuNR-75k	NIPAM-6	75	1.19	300	37 ± 6
AuNR-89k	NIPAM-7	89	1.18	302	46 ± 8
AuNR-114k	NIPAM-8	114	1.27	200	56 ± 10
AuNR-134k	NIPAM-9	134	1.36	610	68 ± 14

The obtained TE micrographs of polymer-grafted gold nanorods are depicted in Figure 5.7. It cleary shows that with different average molecular weights of the RAFT-polymers, interparticle distances between the AuNRs can be precisely tuned. Due to particles' anisotropy interparticle spacing was determined as

shortest distance between adjacent NRs (see Figure 5.7: red arrows). The accumulated results of TEM evaluations are given in Table 5.3 and visualized in Figure 5.8.

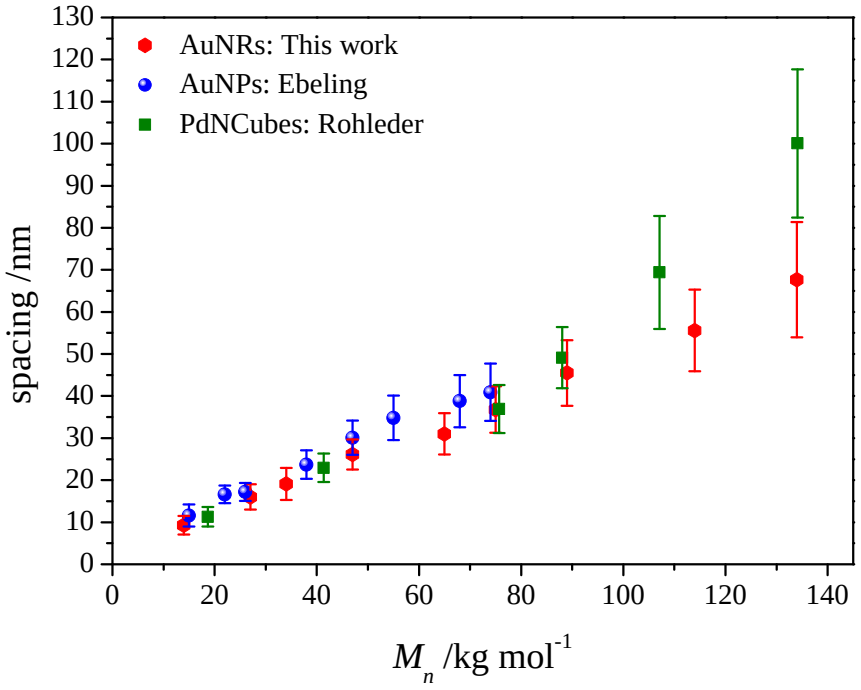

Fig. 5.8: Plot of the interparticle spacing of gold nanorods (hexagon) compared to spherical AuNPs (sphere) and Pd nanocubes (cube) while each is functionalized with different NIPAM RAFT-polymers of various average molecular weights.

Using polymers with an average molecular weight between 14 $\times$ 10^3 g mol^{-1} to 134 $\times$ 10^3 g mol^{-1} interparticle distances ranged from 9 nm to 68 nm. The standard deviation was found to be rather constant between 15 - 20 %. Regarding SERS applications, small interparticle distances are of greater interest to create near-field hot-spots at NR-NR junctions (see Equation 5.1). As mentioned above spacings have to be in a similar scale with the diameter of the AuNRs to gain effective plasmonic coupling between adjacent NRs. The nanohybrids presented here fullfill this key requirement. Compared to the studies of *Ebeling* and *Rohleder* where spherical AuNPs and PdNCubes were coated with NIPAM

RAFT-polymers respectively in similar approaches, interparticle spacings for polymer-grafted AuNRs is slightly decreased at similar average molecular weights (see Figure 5.8).[12,21,67]
Due to the high curvature at tips of the NR, the polymer brush could be more fanned out opposed to the flatter longside, leading to a more pronounced interpenetration of adjacent nanohybrids and consequently shorter distances. As opposed to spherical NPs the grafting density should therefore not be homogeneous over the entire AuNR. *Kumacheva et al.* could show that sulfur-containing ligands can be specifically anchored towards certain facets of the nanorods due to different binding energies with the respective surface facets.[245,257,258] Therefore, it appears obvious that grafting densities may be inhomogeneous over the anisotropic gold NR. These effects could also play a crucial role for the array of these nanohybrids. Along the whole molecular weight spectrum it appears that small areas of multiple nanohybrids are arranged preferentially in a slightly distorted side-by-side alignment rather than a T-shape orientation (see Figure 5.7: yellow boxes). This could be caused by the larger shell-surface area available along the long axis of the nanorod and therefore more potential interactions sites for two adjacent nanohybrids during the drop-casting process. However, opposed to works of *Ebeling*[12,67] and *Rohleder*[21] no specific hexagonal arrangement was obeserved which is most likely caused by the anisotropy of the NR and therefore of the polymer shells. This can be visualized by atomic force microscopy (AFM) since it reveals the outside of the polymer shells rather than the AuNR cores in TEM. Similar to the sample preparation for TEM analysis, a silicon wafer was drop-cast with a nanohybrid solution of sample AuNR-75k. Using this preparation approach no close-packed lattice occured even though the same nanohybrid solution as in TEM was used. Similar results were obtained by *Ebeling* in the AFM analysis of spherical AuNP functionalized with NIPAM RAFT-polymers.[67] All polymer-grafted AuNRs were found to be completely isolated (see Figure 5.9 **(a)**) which could be caused by more pronounced interactions (eg. van-der Waals, dipole–dipole, hydrogen bonding, etc.) of the polymer shell with the silicon wafer surface in AFM compared to the amorphous carbon film in TEM. Both AFM images in Figure 5.9 display that the polymer shell is not spherical which can help explaining the fact that no hexagonal pattern is formed. Due to its isotropy nanohybrids of spherical gold NPs orientation between at least two adjacent

nanohybrids is not relevant. However, considering polymer-grafted AuNRs, the orientation during the evaporation process in a drop-casting approach becomes significant.

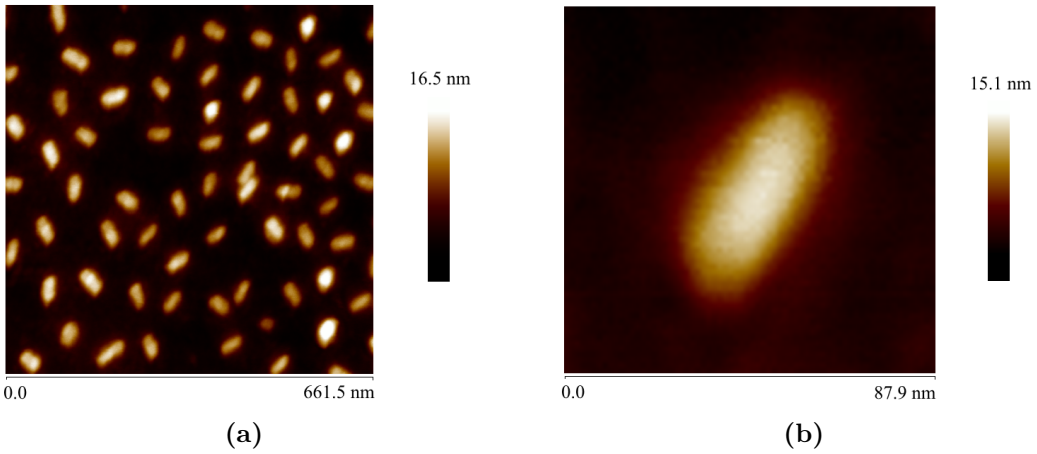

Fig. 5.9: Atomic force microscopy images of the nanohybrid sample AuNR-75k at different magnifications: **(a)** overview over several nanohybrids and **(b)** isolated nanohybrid.

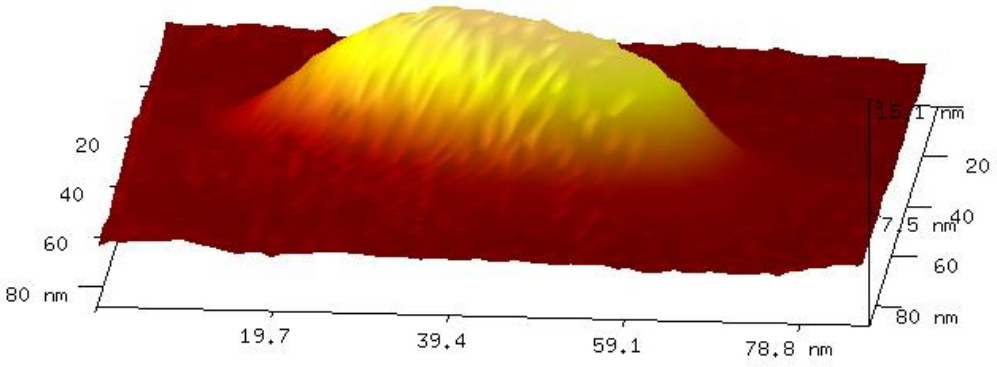

Fig. 5.10: 3D AFM images of an isolated nanohybrid of the sample AuNR-75k.

Figure 5.10 displays the 3D image of the isolated nanohybrid from Figure 5.9 **(b)**. The respective height profiles of the nanohybrid along the two axes

of the nanorod ($34 \times 8\,\mathrm{nm}$) are depicted in Figure 5.11. In this specific case, the polymer shell thickness (distance between nanorod surface and end of the polymer shell in Figure 5.11 **(a)** and **(b)**) agrees very well with half the average interparticle distance obtained from TEM (see Table 5.3: $^{37 \pm 6\,\mathrm{nm}}/_{2}$).

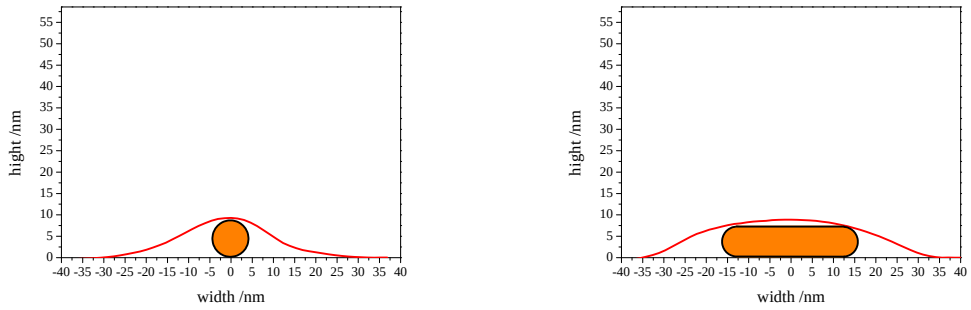

(a) **(b)**

Fig. 5.11: Height profiles of an isolated nanohybrid from sample AuNR-75k **(a)** along the short axis **(b)** along the long axis of the gold nanorod.

To evaluate its solution properties of polymer-grafted gold nanorods dynamic light scattering (DLS) experiments of nanohybrids dispersed in EtOH were conducted. DLS is a common technique to investigate diffusional constants of particles. Generally, diffusion coefficients are highly dependent on the mass, shape, and surface chemistry since all parameters determine the particle–solvent interaction and consequently the Brownian motion. If particles obey the Stokes–Einstein equation, then a hydrodynamic diameter can be extracted.[259] In this context, AuNRs have been studied extensively in the literature.[260–262] Due to their rod-like shape, two peaks can be observed for AuNRs in the intensity distribution fit. They can be assigned to two different relaxation modes occurring for rod-shaped particles: (i) translational diffusion and (ii) the rotational diffusion of the nanorods. A common mistake in DLS analyses of these anisotropic particles is to assign the low-range intensity distribution peak to small particle impurities. However, due to the anisotropy of nanorods, the Stokes–Einstein equation is not obeyed. Therefore, only diffusion coefficients can be determined, while hydrodynamic diameters cannot be extracted. Consequently, it did not appear sufficient enough to take the

intensity peak of the translational diffusion as an accurate measure for the actual size of the particles. However, studies from literature suggest that the peak corresponding to the rotational diffusion is characteristic for the dimensions of the particle. *Liu et al.* showed that the rotational diffusion is highly affected by the aspect ratio of the NRs (AuNR length was held constant), while the translational diffusion was nearly unchanged, even though the mass of the particle increased with an increasing aspect ratio.[262]

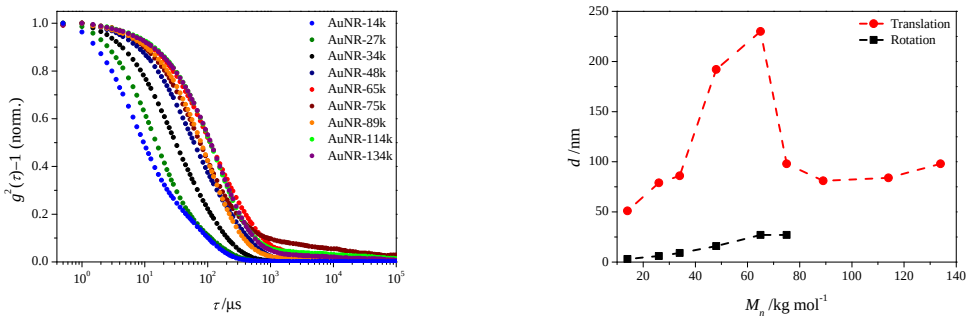

(a) **(b)**

Fig. 5.12: **(a)** Correlation data obtained from DLS experiments in EtOH at 25 °C of AuNR nanohybrids with various average molecular weights grafted onto the gold surface (for clarity purposes: correlation data were normalized) **(b)** Illustration of the hydrodynamic diameter of AuNR nanohybrids (**Red:** Translational contribution and **Black:** Pseudo rotational contribution).

In the present work, CTAB-capped AuNRs were functionalized by NIPAM-polymers with various average chain lengths. Figure 5.12 **(a)** shows the correlation data of these Au nanohybrids. A general trend of increasing correlation times with increasing average molecular weight of the polymer grafted to the AuNR surface can be assigned. In Figure 5.12 **(b)** the average hydrodynamic diameter of the nanohybrids is depicted. For nanohybrids with polymers in the range of 14-75 $\times$ 10^3 g mol^{-1} both relaxation (translation and rotation) processes can be observed. For polymers above this threshold only one relaxation process (translational diffusion) could be extracted from DLS data. Generally, the pseudo-diameter assigned to the rotational diffusion increases the higher the molecular weight grafted onto the AuNR surface which corresponds to a lowered diffusivity. It appears plausible that the longer the polymer chain

is the more hindered the rotation of the AuNRs becomes within the solvent and therefore relaxation times are increased (see Scheme 5.1).

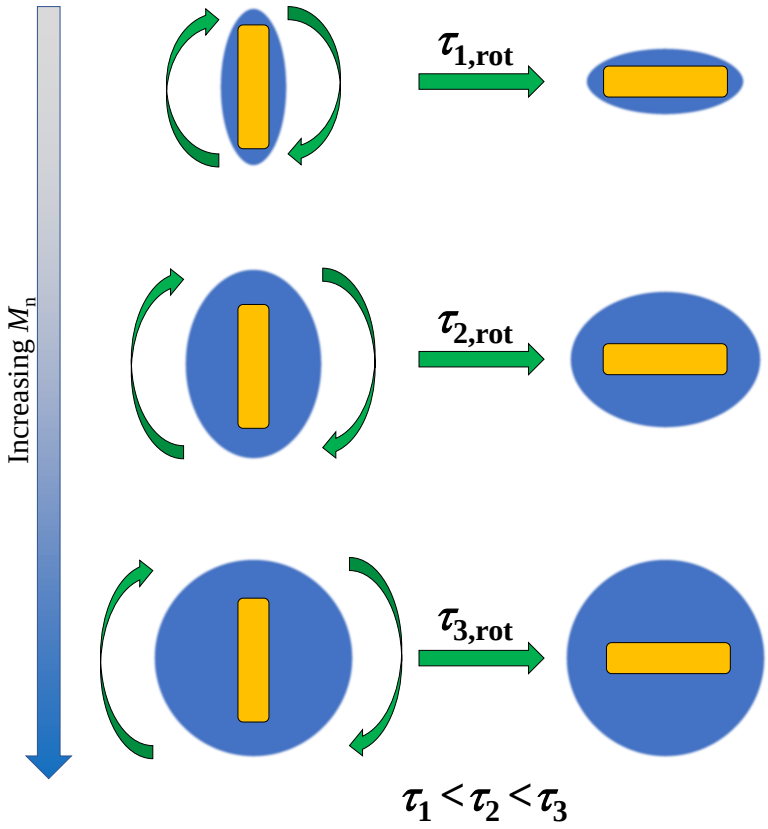

Scheme 5.1: Illustration of the rotational diffusion-time (τ_{rot}) evolution of AuNR nanohybrids in solution with increasing average molecular weight of the grafted polymer.

For nanohybrids with polymers of an average molecular weight of $> 89 \times 10^3\,\mathrm{g\,mol^{-1}}$ no rotational information can be obtained any further. Interestingly, the translational diffusion of AuNR nanohybrids does not decrease over the whole molecular weight range of polymers grafted onto the surface. However, it was observed that for polymers in in the range from 14-65 $\times$ $10^3\,\mathrm{g\,mol^{-1}}$ the diffusivity decreases corresponding to an increase in hydrodynamic diameter, followed by an acceleration of the diffusion with polymers of $75 \times 10^3\,\mathrm{g\,mol^{-1}}$ and $89 \times 10^3\,\mathrm{g\,mol^{-1}}$ while for polymers with $114 \times 10^3\,\mathrm{g\,mol^{-1}}$ and $134 \times 10^3\,\mathrm{g\,mol^{-1}}$

diffusion is slowed down again. This behavior is contra-intuitive since larger polymers should increase the overall size of the nanohybrid and therefore slow down the diffusion. However, as mentioned above, *Liu et al.* obtained similar results where the translational diffusion was not necessarily correlated to the size of the NR.[262] These observations illustrate that translational diffusion is not able to provide an accurate measure regarding the hydrodynamic diffusion in DLS analysis. It can only be assumed that by grafting different average chain lengths onto AuNRs not only the mass of the overall nanohybrid is changed but also its shape and its interaction with the solvent (EtOH). Therefore, it is possible that the rotational diffusion may affect the translational diffusion. Further theoretical studies are required to give more information about the rotational and translational behavior of AuNR nanohybrids in solution.

5.4.2 Functionalization of AuNRs Using 3-Arm Star NIPAM Homopolymers

The functionalization of gold-, silver- and palladium nanopartilces with star RAFT-polymers was presented by *Rossner*[14,16] *Peng*[19,243] and *Rohleder.*[21] Compared to linear RAFT-polymers, they offer the opportunity to attach further particles onto the outer sphere of the nanohybrid. Due to the steric demand of the polymer coil, not all arms of the polymer can be immobilized on the metal core. Consequently, free TTC groups remain unbound and are thus available to capture other metal nanoparticles that show an affinity to sulfur groups (gold, silver, palladium, etc.). As a result, mono- and bimetallic planet–satellite nanohybrids could be prepared.[14,16,19,21]
The synthesis of 3-arm NIPAM RAFT-polymers is shown in Section 5.3. The functionalization procedure is identical to the procedure described for linear NIPAM homopolymers (see detailed description in Chapter 8). After three centrifugation–redispersion steps, nanohybrids were dissolved in ethanol. TEM samples were prepared *via* drop-casting of the respective nanohybrid solutions and subsequently analyzed. Exemplary micrographs are shown in Figure 5.13. Observations are very similar to those obtained for linear NIPAM RAFT-polymer (see Figure 5.7). The evaluation of TE micrographs is given in Table 5.4. By altering the average molecular weight of the grafted polymer between $35 \times 10^3\,\mathrm{g\,mol^{-1}}$ and $169 \times 10^3\,\mathrm{g\,mol^{-1}}$ NR–NR spacing could be tuned between

10 nm and 52 nm. Similar to their linear counterparts, areas with nanohybrids in a partially distorted side-by-side alignment could be observed.

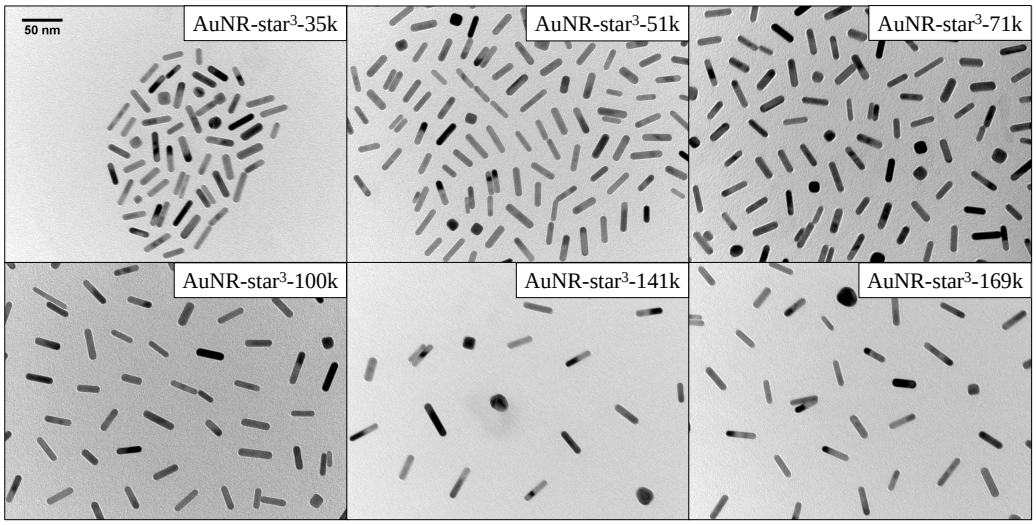

Fig. 5.13: TE micrographs of AuNRs functioanlized with 3-arm star RAFT-polymers with various chain lengths. Scalebar (50 nm) is valid for all micrographs.

Tab. 5.4: Results of the TE micrograph evaluation of AuNRs functionalized with 3-arm star RAFT-polymers.

sample	polymer	$M_{n,\mathrm{SEC}}$ / $10^3\,\mathrm{g\,mol^{-1}}$	$Đ$	no. of distances	spacing / nm
AuNR-star^3-35k	star^3-1	35	1.07	404	10 ± 2
AuNR-star^3-51k	star^3-2	51	1.07	485	16 ± 3
AuNR-star^3-71k	star^3-3	71	1.07	497	19 ± 4
AuNR-star^3-100k	star^3-4	100	1.08	427	29 ± 6
AuNR-star^3-141k	star^3-5	141	1.23	140	40 ± 10
AuNR-star^3-169k	star^3-6	169	1.36	346	52 ± 10

According to AuNRs functionalized with linear NIPAM RAFT-polymers, nanohybrids were analyzed by DLS measurements. In Figure 5.14 **(a)** correlation

data of 3-arm star polymer-grafted AuNRs are shown. Here, correlation curves shift to longer correlation times which is generally consistent with an increasing shell thickness observed in TEM. Similar to their linear equivalent, a direct translation of diffusion constants into hydrodynamic diameters is not possible. Again, evaluation of the translational diameter revealed a non-intuitive maximum of the hydrodynamic diameter for AuNR-star^3-71k. However, pseudo-diameters for rotational diameters increase throughout the whole molecular weight spectrum despite the AuNR-star^3-169k sample. This is consistent with the model depicted in Scheme 5.1.

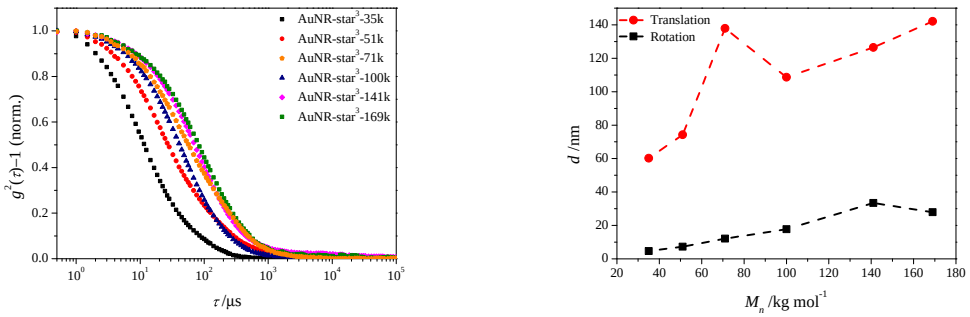

(a) **(b)**

Fig. 5.14: **(a)** Correlation data obtained from DLS experiments in EtOH at 25 °C of AuNR nanohybrids with various 3-arm star polymers grafted onto the gold surface (correlation data were normalized for clarity purposes) **(b)** Illustration of the hydrodynamic diameter of AuNR nanohybrids (**Red:** Translational contribution and **Black:** Pseudo rotational contribution).

5.4.3 Fabrication of AuNR-Planet–AuNP-Satellite Structures

As already described above, metal nanocrystals functionalized with star RAFT-polymers can be further decorated with other metal nanoparticles forming mono- or bimetallic planet–satellite structures with tunable distances.[14,16,19,21] Up to this point, the use of AuNRs has not been studied in the context of adjustable planet–satellite distances. This however, may be of great interest since *Shao et al.* demonstrated by theoretical calculations that the electric field intensity of AuNR–AuNP heterodimers is significantly enhanced at the lower-energy peak

at their surface junctions.[29] Opposed to homodimers of AuNRs where their orientation plays a crucial role such planet–satellite heterostructures always create hot-spots in the gap-region independently where the the AuNP is placed around the NR.[263]
Up to now, only few studies addressed bottom-up approaches to fabricate AuNR-planet–AuNP-satellite heterostructures. *Pierrat et al.* were able immobilize spherical gold nanoparticles (AuNPs) onto poly(ethylene glycol) (PEG)-grafted AuNRs.[264] However, AuNPs were always located in very close proximity to the AuNR surface and PEG did not offer distance scaling through this process. In a similar approach, *Greiner et al.* immobilized H_2N-poly(NIPAM)-SH onto AuNRs.[265] The polymer served as glue to bind the gold nanoparticles but AuNPs were again found in close vicinity to the rod surface. However, *Raessi et al.* showed that a DNA linkage between gold nanorods and smaller gold nanoparticles as satellites can keep the satellites away from the nanorod surface.[213] However, planet–satellite distances were not tunable in this approach while the fabrication of specific DNA linkers is highly laborious and cost-intensive. A hierarchical approach to fabricate such structures using gold nanorods and gold nanoparticle with a multifunctional star RAFT-polymer linker appeared to be the more straightforward, variable and economical strategy.

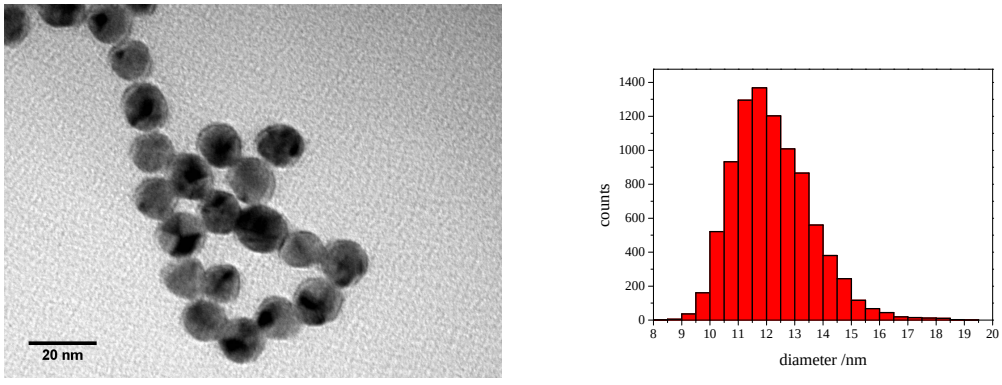

(a) **(b)**

Fig. 5.15: (a) Exemplary TE micrograph of citrate-capped AuNPs fabricated *via* the *Turkevich*-method and **(b)** the respective histogram of AuNPs.[21]

Therefore, satellites had to be fabricated with an exchangeable surfactant. The *Turkevich*-method to yield citrate-capped AuNPs was thus chosen to obtain

quasi-spherical, polycrystalline gold nanoparticles in aqueous solution.[62–66] Accordingly, AuNPs were fabricated by adding a sodium citrate solution to a refluxing $HAuCl_4$-solution. A detailed description of the procedure is presented in the Experimental Section 8. TE microscopy analysis revealed nanoparticles of 12 ± 1 nm in diameter (see Figure 5.15).

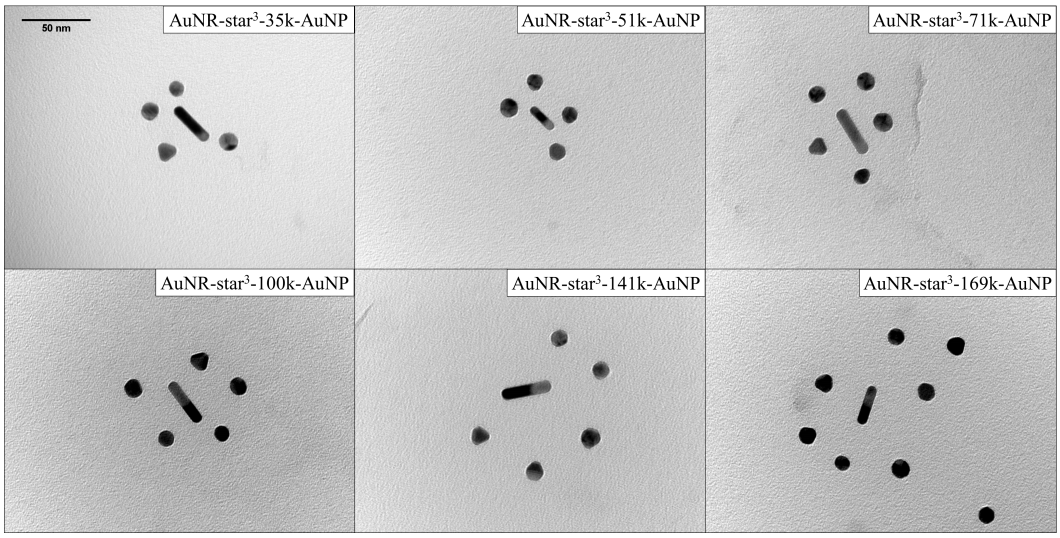

Fig. 5.16: TE micrographs of individual AuNR-planet–AuNP-satellite-nanostructures functionalized with different 3-arm star-RAFT-polymers with various chain lengths. Scalebar (50 nm) is valid for all micrographs.

Once these suitable satellites were synthesized, AuNPs were added to AuNRs capped with different 3-arm star RAFT-polymers. In a typical experiment, AuNR nanohybrids were dissolved in ethanol and an excess of citrate-capped AuNPs (~12 nm) was added under ultrasonication. After 30 min of incubation the linear RAFT-polymer NIPAM-4 ($M_n = 48 \times 10^3$ g mol^{-1}) was added to shield the outer sphere of the satellites. Studies of *Rossner* and *Peng* demonstrated that the addition of linear polymer is crucial to avoid nanohybrid aggregation and to ensure its easy redispersion.[170,243] After further 30 min, two centrifugation–redispersion steps were conducted (ethanol, 500 *g*, 1 h, 5 °C) to remove unbound AuNPs and the excess of linear polymer NIPAM-4. Exemplary TE micrographs of planet–satellite structures are given in Figure 5.16 and Figure 5.17.

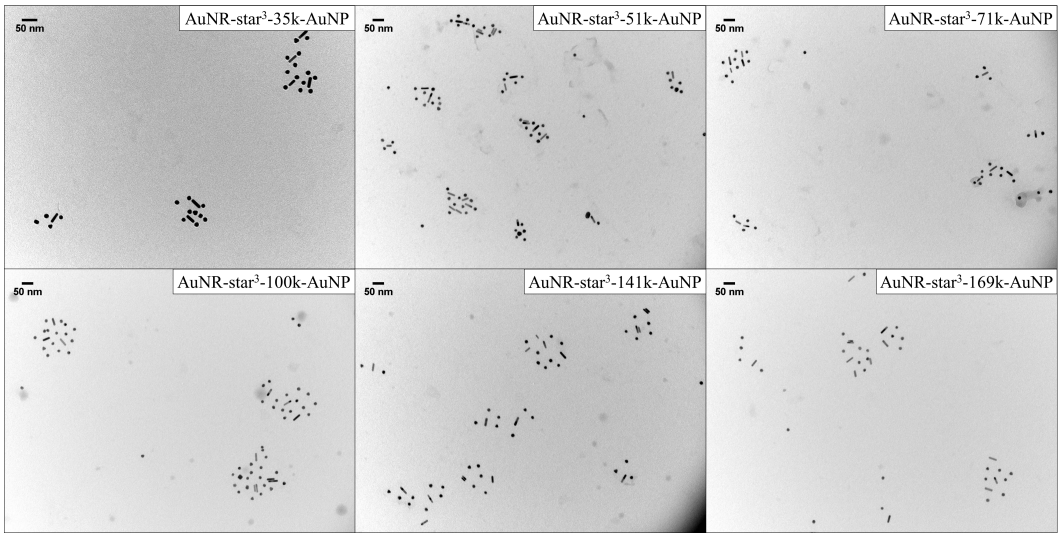

Fig. 5.17: TE micrographs of AuNR-planet–AuNP-satellite-nanostructures functionalized with different 3-arm star-RAFT-polymers with various chain lengths.

It could be shown that AuNR nanohybrids offer sufficient quantities of free TTC groups on the outer sphere of the shell to attach further particles. The AuNPs were distributed homogeneously around the AuNR-planet with no preferential binding side. As shown in Table 5.5, planet–satellite distances can be tuned through an adjustment of the average molecular weight of the star polymer. Similar to AuNR homoassemblies, short interparticle distances are of higher interest to create near-field hot-spots within the gap-region.[29] The planet–satellite nanohybrids display spacings down to a comparable scale with respect to AuNR diameter which is ideal to induce plasmonic coupling between planet and satellites.

The spacings of AuNRs functionalized with 3-arm star polymers observed in TEM is determined by the thickness of two adjacent polymer shells. Therefore, planet–satellite distances should be found at approximately half the values of these nanohybrids, intuitively. As seen in Figure 5.18 and by comparing the spacing shown in Tables 5.4 and 5.5 the spacing-ratios of the respective Pd-polymer-nanohybrids and the Pd-planet–Au-satellite structures, range from 0.47 - 0.61. Taking into account the standard deviations up to ~20% ratios stay in good agreement with the expected values.

Tab. 5.5: Results of the TE micrograph evaluation of planet–satellite distances between AuNRs functionalized with 3-arm star RAFT-polymers and spherical AuNPs.

sample	polymer	$M_{n,\mathrm{SEC}}$ / 10^3 g mol^{-1}	$Đ$	no. of distances	spacing / nm
AuNR-star^3-35k-AuNP	star^3-1	35	1.07	123	6 ± 2
AuNR-star^3-51k-AuNP	star^3-2	51	1.07	134	8 ± 2
AuNR-star^3-71k-AuNP	star^3-3	71	1.07	102	13 ± 4
AuNR-star^3-100k-AuNP	star^3-4	100	1.08	126	17 ± 4
AuNR-star^3-141k-AuNP	star^3-5	141	1.23	131	24 ± 6
AuNR-star^3-169k-AuNP	star^3-6	169	1.36	106	26 ± 5

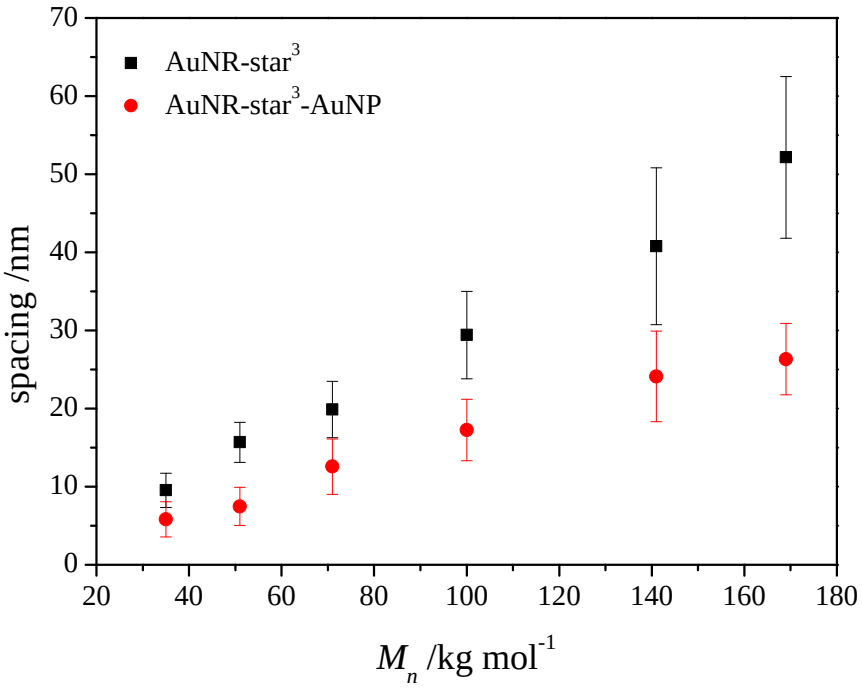

Fig. 5.18: Plot of the interparticle spacing of gold nanorods functionalized with different NIPAM 3-arm star RAFT-polymers and AuNR-core–AuNP-satellite nanohybrids.

Planet–satellite structures were further analyzed by dynamic light scattering experiments. Due to the complex structure of these nanohybrids no evaluation of hydrodynamic diameters was conducted. However, correlation data can give relative evidence between different samples about their size. As seen in Figure 5.19 AuNRs functionalized with 3-arm star RAFT-polymers were compared to their equivalents which were decorated with further gold nanoparticles. In general, correlation curves shift to longer correlation times indicating a decrease in the diffusional constant as a result from an increased nanohybrid size. By comparing planet–satellite nanohybrids among themselves (see Figure 5.20) it can be noticed that the correlation curves shift towards longer correlation times along larger polymers grafted between planet and satellites. This observation is plausible since larger particles show prolonged correlation times. However, sample AuNR-star^3-169k-AuNP appeared to have smaller nanohybrids (trend between $\tau = 1 - 100\,\mu s$) and larger aggregates ($\tau > 1000\,\mu s$). The first regime may be determined by planet–satellite structures and free, unbound gold nanoparticles functionalized by NIPAM-4 while the second regime may originate from nanohybrid–nanohybrid linkage through the AuNP satellites.

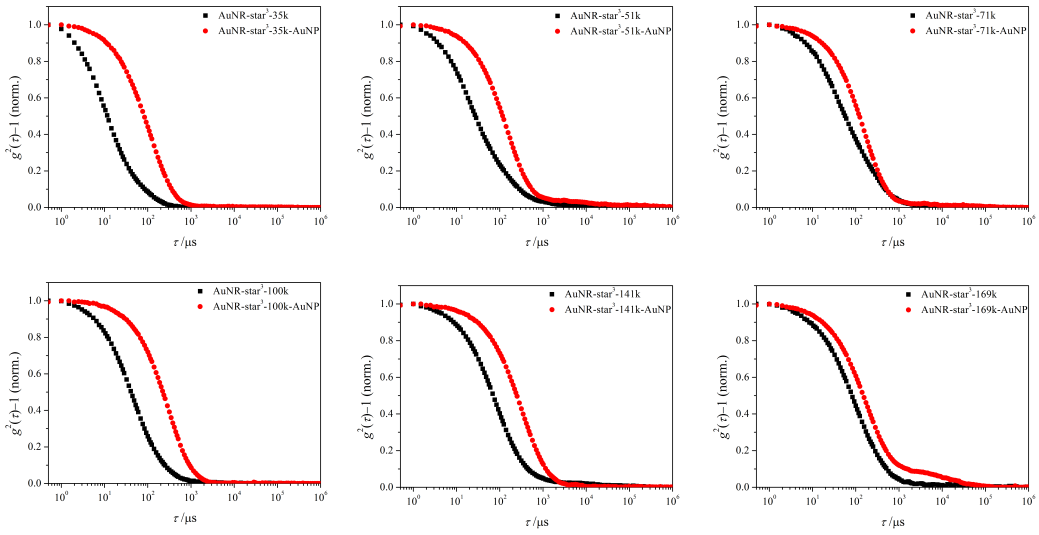

Fig. 5.19: Correlation data obtained from DLS experiments in EtOH at 25 °C of AuNR functionalized with 3-arm star RAFT-polymer compared to their planet–satellite-nanostructures (correlation data were normalized for clarity purposes)

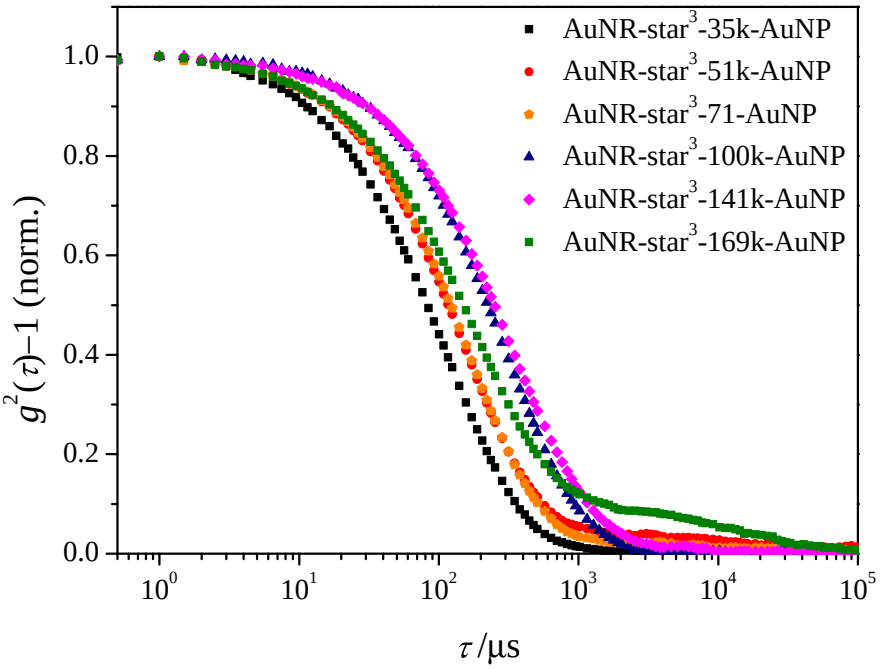

Fig. 5.20: Correlation data obtained from DLS experiments in EtOH at 25 °C of AuNR-planet–AuNP-satellite-nanostructures with different polymeric linker lengths (correlation data were normalized for clarity purposes)

The optical properties in solution were investigated by UV/vis-spectroscopy. In Table 5.6 evaluation data of UV/vis measurements of citrate-capped AuNPs, AuNR-star^3-nanohybrids and AuNR-star^3-nanohybrids decorated with AuNPs are given. Generally, the transverse LSPR of planet-satellite structures is red-shifted by about 6 nm when compared to spherical AuNPs and 2 nm compared to polymer-functionalized AuNRs. The respective longitudinal LSPR blue-shifts between 2 nm to 12 nm with respect to their polymer-coated counterparts. The red-shift of λ_{trans} can be attributed to an increase of refractive index from water (1.33) to ethanol (1.36) since the citrate-capped AuNPs were measured in aqueous solution.[266] *Mulvaney et al.* studied the influence of refractive index (RI) on the LSPR of gold nanoparticles. They could show that higher RIs lead to larger λ_{LSPR} which is at the same time in excellent agreement with the Mie theory (see Chapter 2).[100] Opposed to that, the blue-shift of λ_{long} can not be

assigned to the change of refractive index. Plasmonic coupling between AuNR-core and AuNP-satellites may be the reason for this observation.[29,98] However, a clear trend along the different polymer linker lengths can not be assigned even though the blue-shift for the samples AuNR-star^3-141k and AuNR-star^3-169k is slightly smaller than for the other samples which would follow the trend of the plasmonic ruler Equation 5.1. Here, the coupling decays exponentially with the center of mass distance. In this context, *Rossner* evaluated planet–satellite structures from citrate-capped AuNPs and Brust–Schiffrin AuNPs (see Chapter 2) with different star polymer linker lengths between 23-63 $\times$ $10^3\,\mathrm{g\,mol^{-1}}$ by small angle X-ray scattering (SAXS).[170] It could be shown that in solution planet–satellite distances do not strictly scale with increasing average molecular weight of the grafted star polymer even though TEM analyses suggested otherwise. This might help explaining the similar shifts of λ_{long} along different linker lengths and thus different planet–satellite distances. Exemplary UV/vis spectra of citrate-capped AuNPs, AuNR-star^3-35k and AuNR-star^3-35k-AuNP are given in Figure 5.21.

Tab. 5.6: Results of the UV/vis evaluation between citrate-capped AuNPs, AuNR-star^3-nanohybrids and AuNR-star^3-nanohybrids decorated with AuNPs.

sample	polymer	$M_{n,\mathrm{SEC}}$ / $10^3\,\mathrm{g\,mol^{-1}}$	$^{\alpha}\Delta\lambda_{\mathrm{trans}}$ / nm	$\Delta\lambda_{\mathrm{long}}$ / nm
AuNR-star^3-35k-AuNP	star^3-1	35	6/2	−8
AuNR-star^3-51k-AuNP	star^3-2	51	6/2	−12
AuNR-star^3-71k-AuNP	star^3-3	71	6/2	−8
AuNR-star^3-100k-AuNP	star^3-4	100	6/2	−12
AuNR-star^3-141k-AuNP	star^3-5	141	6/4	−6
AuNR-star^3-169k-AuNP	star^3-6	169	6/2	−2

$^{\alpha}$ The first value corresponds to the difference between planet–satellite structures and planet nanohybrids while the second value corresponds to the difference between planet–satellite structures and gold nanoparticles.

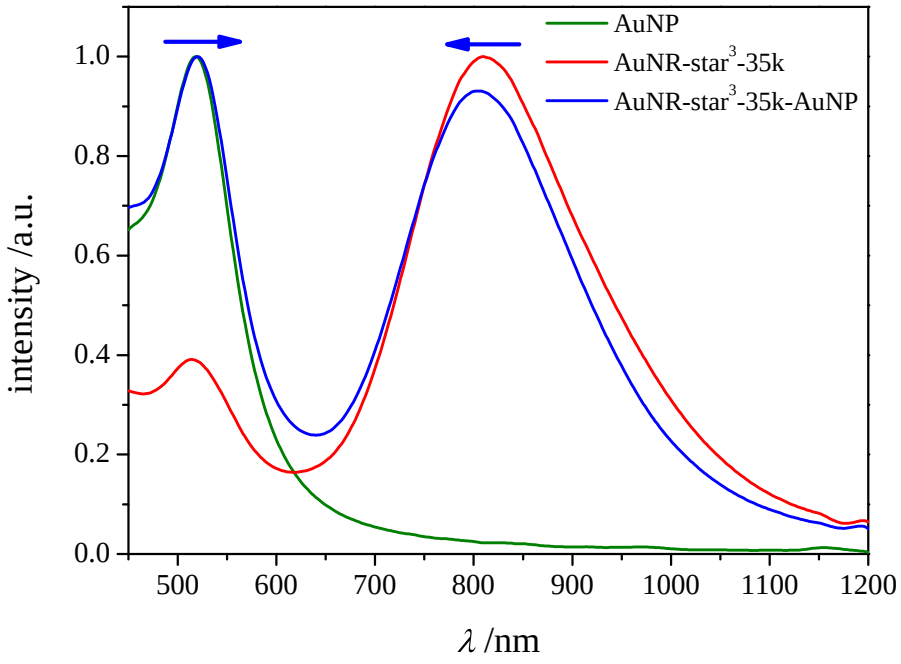

Fig. 5.21: UV/vis spectra of citrate-capped AuNPs (green), AuNR-star^3-35k (red) and AuNR-star^3-35k-AuNP (blue). All spectra were normalized to their respective maximum.

5.5 Summary and Conclusion

Within this chapter, effective and straightforward routes towards polymer-grafted gold nanorods with variable shell thicknesses were established. This was achieved by the RAFT-polymerization of *N*-isopropyl acrylamide using both monofuctional and 3-arm star RAFT-agents. The inherently formed trithiocarbonate groups served as anchoring ligands on AuNR surfaces while macromolecules with various molecular weights enabled variable sizes of these nanohybrids. By drop-casting 2D nanoarrays of AuNR–polymer nanohybrids could be formed with tunable interparticle spacings along different polymer chain lengths. Here, slightly distorted side-by-side alignments with respect to the AuNR-core were arranged preferentially.
Gold nanorods functionalized by 3-arm star RAFT-polymers could be further

applied in a hierarchical self-assembly approach using 13 nm spherical gold nanoparticles to yield planet–satellite nanostructures. Since not all arms of the star polymer are bound to the AuNR surface, the outer sphere of the nanohybrid shell beared enough free TTC groups to covalently link multiple AuNPs. TEM evaluations have shown that the spacings between AuNR-planet and AuNP-satellites were precisely tuned by the average chain length of the macromolecular linker. Along all chain lengths a blue-shift of the longitudinal LSPR of gold nanorods was observed indicating a plasmonic coupling between the planet and satellites.

Overall, highly step-efficient and straightforward approaches to yield nano-assemblies focussing on the tuning of the optical and plasmonic properties of AuNRs were presented. The advantages of this approach include its flexible tunability, highly reliable syntheses and facilitated processability, which are demonstrated by successful fabrications of a series of well-defined nanostructures with targeted properties.

6 Copolymer-Grafted Gold Nanorods as Stimuli Responsive Hybrid Material

The content of the following chapter has already been published by the author of this work and results were adapted with permission of the journal and the authors. [267]

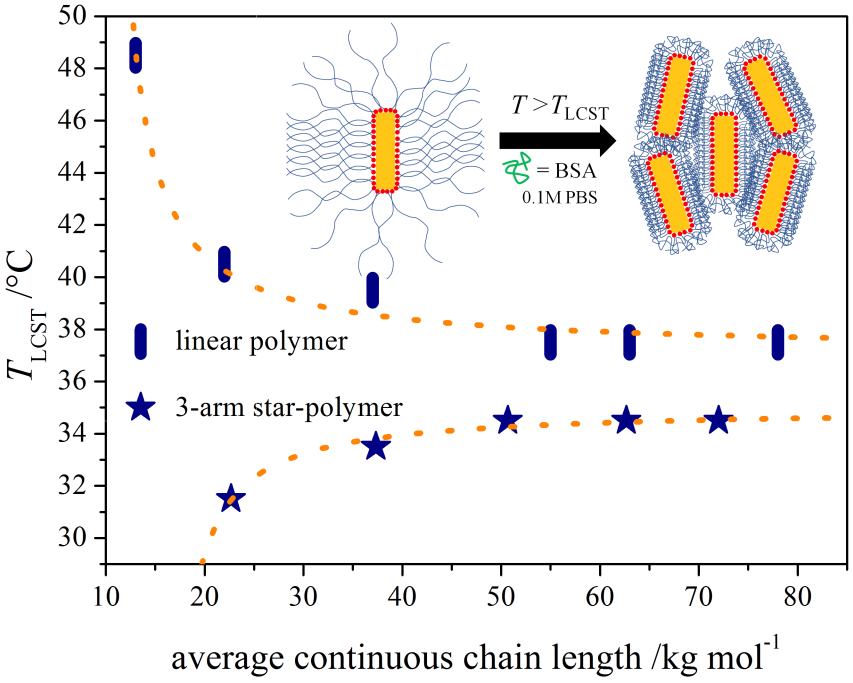

6.1 Introduction and State of the Art

The treatment and cure of cancer are one of the major challenges in medicine. General therapy strategies range from straightforward removal of early-stage

tumors to chemo- and radiotherapy of advanced-stage tumors. The greatest obstacle in chemotherapy using small molecular drugs is based on the lack of tumor selectivity and therefore selective toxicity.[268] This is caused by the renal clearance threshold for macromolecules and quantum dots. If their size becomes smaller than $40\,\mathrm{kg\,mol^{-1}}$ or $\sim 5\,\mathrm{nm}$, then blood circulation times are significantly decreased, and hence, drugs are excreted more quickly.[269,270] However, the directed accumulation of blood-injected drugs and particles into specific parts of the human body is inevitable to decrease dosages and thus potential therapeutic side effects. In this regard, studies of *Matumura* and *Maeda* opened to door for a more tumor specific therapy by discovering and describing the so called *Enhanced Permeability and Retention* (EPR) effect.[271,272] It is based on an mutated blood vessel architecture in tumors resulting in an enhancement in vascularity and permeability. This ensures an sufficient supply of oxygen, minerals and other nutrients which leads to the fast growth of tumors. Simultaneously, the retention time in tumor tissue is drastically increased opposed to healthy tissue due to an inefficient lymphatic drainage.[273] The EPR effect is not only size or molecular weight dependent but also on the surface chemistry (including biocompatibility and surface charge) of the respective molecule or particle.[274] Since the vascular endothelial luminal surface (barrier between blood and tissue) carries negative charges anionic or neutral agents are expected to have longer blood circulation times. Therefore, a very common approach in tumor drug functionalization relies on the functionalization with polyethylene glycol (PEG) of molecules or particles.[275–280] PEGylated particles offer a hydrated water barrier which results in sufficient steric hindrance to phagocytes (cells that clear the body from dead cells, bacteria and other potential harmful particles) and prolonged circulation times compared to their unfunctionalized counterparts. However, another phenomenon occurs called the PEG-dilemma. Here, PEG-specific antibodies (immunoglobulin M) are vitalized by PEGylated agents and increase their clearance through the liver.[281] Consequently, other functionalization approaches are inevitable to overcome this PEG-dilemma concerning tumor targeted treatment. Up to now, a common strategy is to immobilize DNA linkers onto particles, which still lacks scalability and tunability accompanied by high costs.[213,282,283]

In this context, nanoparticle-mediated photothermal therapy (PTT) has emerged

great attention within the last years.[84,284] In combination with the EPR effect it allows selective hyperthermia of tumor tissue. Among other inorganic particles, gold nanoparticles (AuNP) are known to absorb light and convert this energy into heat through various non-radiative processes.[77] When a certain oscillating electromagnetic wave hits a metal NP the conduction band electrons start a coherent oscillation which leads to a charge separation of with respect to the ionic lattice. The amplitude of the dipole oscillation reaches its maximum at a certain frequency called localized surface plasmon resonance (LSPR, see Section 2.1.2.3). Within this oscillation electron–electron collisions occur leading to a loss of coherency and electrons with high temperatures (~1000 K). Through electron–phonon-relaxation processes hot electrons transfer their energy to the metal lattice. This energy can be ablated to the surrounding medium within hundreds of picoseconds which leads to its increase in temperature. This electron–phonon-coupling can be utilized in PTT to destroy cancer cells.

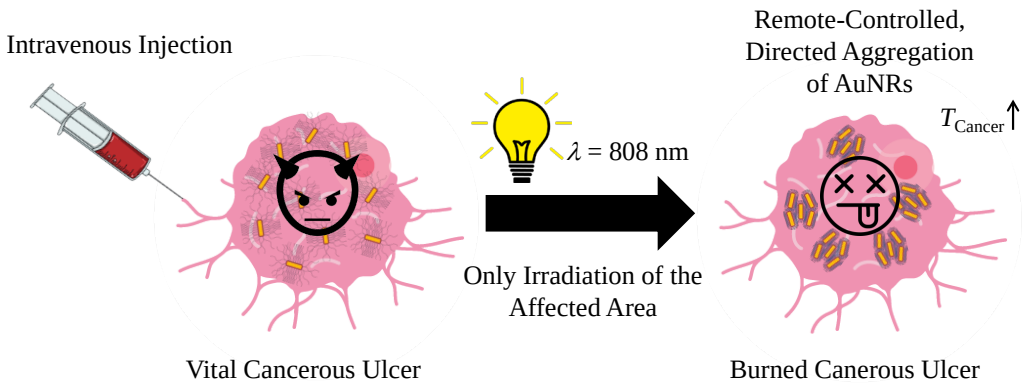

Scheme 6.1: General concept of photothermal-responsive nanohybrids applied in photothermal therapy treating near-surface cancer ulcers.

However, it is required that the human body is sufficiently transparent to let the light pass through its tissue to the respective NP. Basically, the body offers two optical windows in the near-infrared range: 1st 650–950 nm and

2nd 1000–1350 nm.[285] The LSPR of spherical AuNPs ranges between 517–575 nm depending on the size of the particle which makes them unsuitable for PTT. However, the LSPR is not only affected by the size of NP but also on the shape. For example, gold nanocages[72], gold nanoshells[73] and gold nanorods[286] (AuNRs) are known to have tunable LSPRs from red to the near-infrared. These optical properties are mainly determined by the aspect ratio (AR) between length and diameter of the NR.[78] Accordingly, AuNRs possess two distinct LSPRs: a strong longitidunal band along the long axis and a weaker transverse band along the short axis. Due to lower polarizability of LSPR the transverse band is nearly independent on the aspect ratio and occurs at ~520 nm similar to the band of spherical AuNPs. However, the larger the aspect ratio the more red-shifted the LSPR of the longitdunal band.[78] Consequently, AuNRs are well suited for PTT applications due to their tunable optical properties. Therefore, AuNRs have been applied in many *in vitro* and *in vivo* studies already.[84–87] However, decorating AuNRs with an uncharged, responsive polymer has not been performed and may be ideal for a more directed accumulation within certain parts of the body such as cancerous ulcers (see Scheme 6.1). For getting closer to real biomedical applications, it also appears beneficial to perform the studies in biological media instead of in pure water, and we thus investigated the AuNR system in a simulated blood fluid (SBF).

6.2 Polymerizations Using the RAFT-Process

The reversible addition−fragmentation chain transfer polymerization (RAFT-polymerization) is a powerful tool to fabricate tailored polymeric materials with highly accurate architectures and topologies and therefore defined properties and functionalities.[152–154] The use of *N*-isopropyl acrylamide (NIPAM, see Figure 8.1) containing RAFT-polymers in nanoparticle functionalization was studied extensively over the past ten years.[12–17,287]
Here, aurophilic trithiocarbonates were used as anchor groups to immobilize polymers onto noble-metal surfaces. Due to its adequate solubility in various organic solvents and water, poly(NIPAM) is favorable for NP functionalization approaches. In general, poly(NIPAM) is considered as a smart thermoresponsive polymer due to its lower critical solution temperature (LCST) in water at 32 °C for $M_n > 10^4$ g mol^{-1}.[178,179] However, pure poly(NIPAM) is only restrictively

applicable *in vivo* due to its LCST below physiologically relevant temperatures. Therefore, the copolymerization with another monomer may be a suitable approach to shift the LCST above 37 °C.[193] In this context, acrylamide (AAM, see Figure 8.1) appeared to be an adequate candidate as a comonomer due to its high water solubility and similar polymerization kinetics compared to NIPAM, i.e., reactivity ratios in the copolymerization system are close to one.[193] All polymerizations in this work were conducted using an 85:15 feed ratio between NIPAM and AAM assuming the same ratio within the resulting polymeric chain (see Figure 6.1).[193]

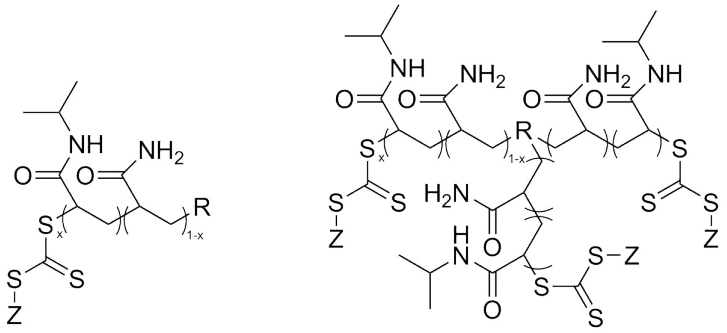

Fig. 6.1: General molecular structures of poly(NIPAM)-*co*-poly(AAM) RAFT copolymers with one trithiocarbonate (TTC) group (l-CoPo) or three TTCs (star^3-CoPo) attached to the chain ends.

6.2.1 Fabrication of Linear NIPAM-*co*-AAM-Copolymers

Linear NIPAM-*co*-AAM RAFT-polymers containing one TTC group at the end of the polymeric chain were synthesized using methyl-2-(((dodecylthio)carbonothioyl)thio)propanoate (l-CTA, see Figure 5.3) as linear chain transfer agent CTA. For a detailed description of the synthetic procedure, see the Experimental Section. The results of the polymerization are summarized in Table 6.1. Copolymers reveal good control over the molecular weight distribution showing low dispersities (Figure 6.2). Additionally, LCST values in nanopure water were determined by dynamic light scattering. Generally, LCST values of poly(NIPAM) in water are investigated at polymer concentrations between 1

and 15 mg mL^{-1}, where the phase diagram shows a plateau and the true LCST is not significantly dependent on the polymer concentration.[288] It should be noted, however, that the exact concentrations for the respective LCSTs of the copolymers were not determined in this work so that reported LCST values may be understood as estimates. However, to provide sufficient comparability, all samples were measured at a copolymer concentration of 5 mg mL^{-1}, which is considered to be close to the critical concentration also of the copolymer. For linear copolymers, LCSTs appeared to be independent of the molecular weight in nanopure water (see Table 6.2) whereas the hydrodynamic diameter of the copolymers increased in general with greater chain lengths of the copolymer.

Tab. 6.1: Results of RAFT-polymerizations to provide linear polymers of different chain lengths for nanocrystal functionalization.

sample	$[M]/[RAFT]$ $^{\alpha}$	eq. of $^{\beta}$ 1,4-dioxane	time / h	conv. $^{\gamma}$ / %	$M_{n,SEC}$ / 10^3 g mol^{-1}	$Đ$
l-CoPo-13k	100	4	4	87	13	1.07
l-CoPo-22k	200	4	4	84	22	1.07
l-CoPo-37k	400	4	4	84	37	1.04
l-CoPo-55k	600	4	4	79	55	1.16
l-CoPo-63k	800	4	4	74	63	1.13
l-CoPo-78k	1200	4	4	58	78	1.19

$^{\alpha}$ $[M]/[RAFT]$: ratio between monomer and RAFT-agent.
$^{\beta}$ Equivalents compared with amount of monomer.
$^{\gamma}$ The conversion was determined by gravimetry.

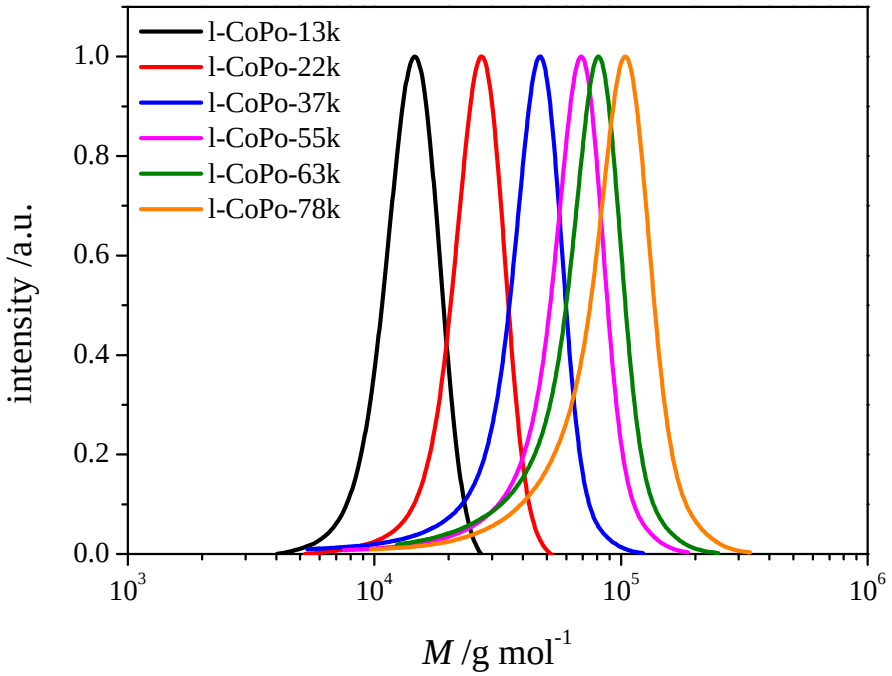

Fig. 6.2: Molecular weight distributions of different linear NIPAM-*co*-AAM-copolymers.

Tab. 6.2: Results of DLS measurements of linear NIPAM-*co*-AAM-copolymers in nanopure water including the LCST values and the hydrodynamic diameter at 37 °C.

sample	$M_{n,\mathrm{SEC}}$ / 10^3 g mol^{-1}	d_{hydro} @ 37 °C / nm	T_{cloud} / °C
l-CoPo-13k	13	18	45 – 46
l-CoPo-22k	22	20	45 – 46
l-CoPo-37k	37	29	45 – 46
l-CoPo-55k	55	67	45 – 46
l-CoPo-63k	63	56	45 – 46
l-CoPo-78k	78	52	45 – 46

6.2.2 Fabrication of 3-arm Star NIPAM-*co*-AAM-Copolymers

Tab. 6.3: Results of RAFT-polymerizations to provide 3-arm star copolymers of different chain lengths for nanocrystal functionalization.

sample	$[M]/[RAFT]$ $^{\alpha}$	eq. of $^{\beta}$ 1,4-dioxane	time / h	conv. $^{\gamma}$ / %	$M_{n,SEC}$ $^{\delta}$ / 10^3 g mol^{-1}	$Đ$
star^3-CoPo-35k	300	4	4	93	35	1.07
star^3-CoPo-56k	500	4	4	96	56	1.04
star^3-CoPo-76k	700	4	4	94	76	1.16
star^3-CoPo-94k	900	4	4	88	94	1.13
star^3-CoPo-108k	1200	4	4	81	108	1.19

$^{\alpha}$ $[M]/[RAFT]$: ratio between monomer and RAFT-agent.
$^{\beta}$ Equivalents compared with amount of monomer.
$^{\gamma}$ The conversion was determined by gravimetry.
$^{\delta}$ $M_{n,SEC}$ values were corrected for 3-arm polymers.[254,255]

To provide 3-arm star-RAFT-polymers containing a TTC group at the end of each arm, propane-1,2,3-triyl tris(2-(((propylthio)carbonothioyl)thio)propanoate) (star^3-CTA, see Figure 8.4) was used as a star-RAFT-agent. Since the leaving group (R-group) is attached to the inner core of the molecule, TTC groups remain in their position in the outer sphere of the star polymer during polymerization (R-group approach).[253] This is necessary for further functionalization experiments to enable the grafting onto the gold nanorod surface. Polymerizations were conducted similar to the synthesis of the linear polymers. The results of the polymerizations are shown in Table 6.3. Similar to their linear counterparts, 3-arm star polymers also reveal good control over the molecular weight distribution (Figure 6.3). However, LCSTs in nanopure water occur at lower values and show a molecular weight dependency (see Table 6.4). This may possibly be explained by the less hydrophilic core in the center of the star polymers and their Z-groups at the chain end (see Figure 8.4). The smaller the polymeric chain, the more pronounced is this effect.[191,192] In contrast

to NIPAM homopolymers, the chain length dependency diminishes only at larger repeating units (r.u.) per arm (this work: r.u. = 175−230, *Plummer et al.*: r.u. ≥ 70).[192] Nevertheless, both copolymer systems show LCSTs above physiologically relevant temperatures. As seen in Table 6.4 hydrodynamic diameter increase with greater chain length, even though this effect is not as pronounced as for the linear copolymers.

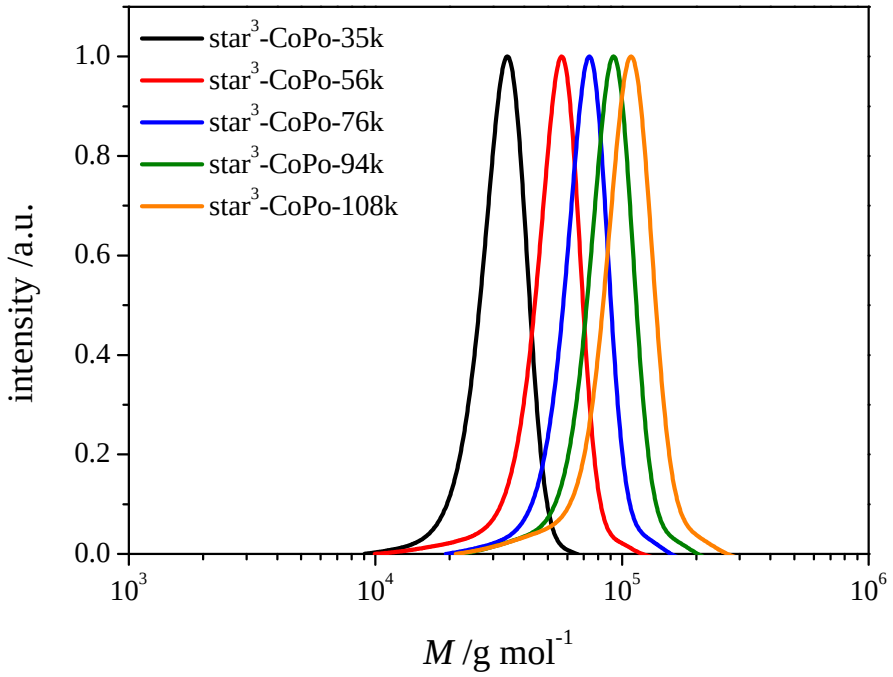

Fig. 6.3: Molecular weight distributions of different 3-arm star NIPAM-*co*-AAM-copolymers.

Tab. 6.4: Results of DLS measurements of 3-arm star NIPAM-*co*-AAM-copolymers in nanopure water including the LCST values and the hydrodynamic diameters at 37 °C.

sample	$M_{n,\mathrm{SEC}}$ / $10^3\,\mathrm{g\,mol^{-1}}$	d_{hydro} @ 37 °C / nm	T_{cloud} / °C
star^3-CoPo-35k	35	9	38 – 39
star^3-CoPo-56k	56	13	40 – 41
star^3-CoPo-76k	76	15	42 – 43
star^3-CoPo-94k	94	18	42 – 43
star^3-CoPo-108k	108	21	42 – 43

6.3 Synthesis of Copolymer-Grafted Gold Nanorods

6.3.1 Fabrication of Gold Nanorods

The fabrication of gold nanorods is described in Chapter 5 already and yielded rods with a length of 34 ± 5 nm and a diameter of 8.2 ± 1.1 nm leading to an aspect ratio of 4.1. These dimensions are in the same order of magnitude as those described in literature for an enhanced cellular uptake. The optimum for CTAB-capped AuNRs was found at an aspect ratio (AR) of ~4 (55×14 nm) compared to AuNRs with lower ARs.[86] For PEGylated AuNRs an aspect ratio of ~4 (41×10 nm) may be ideal to inhibit unspecific uptake and ensure slower blood clearance.[280]

The TEM results (AR = 4.1) agree well with results obtained via UV/vis (see Figure 5.2 **(a)**). The longitudinal surface plasmon resonance band was found at $\lambda_{\mathrm{long}} \sim 810$ nm, which corresponds to an AR of 4.1 (according to the equation provided by *El-Sayed et al.*: $\lambda_{\mathrm{long}} = 420 + 95\,\mathrm{AR}$).[77] These optical properties are highly favorable for in vivo applications due to the LSPR band at ~810 nm, which occurs in the first optical window of the human body.

6.3.2 Functionalization of AuNRs Using NIPAM-*co*-AAM-Copolymers

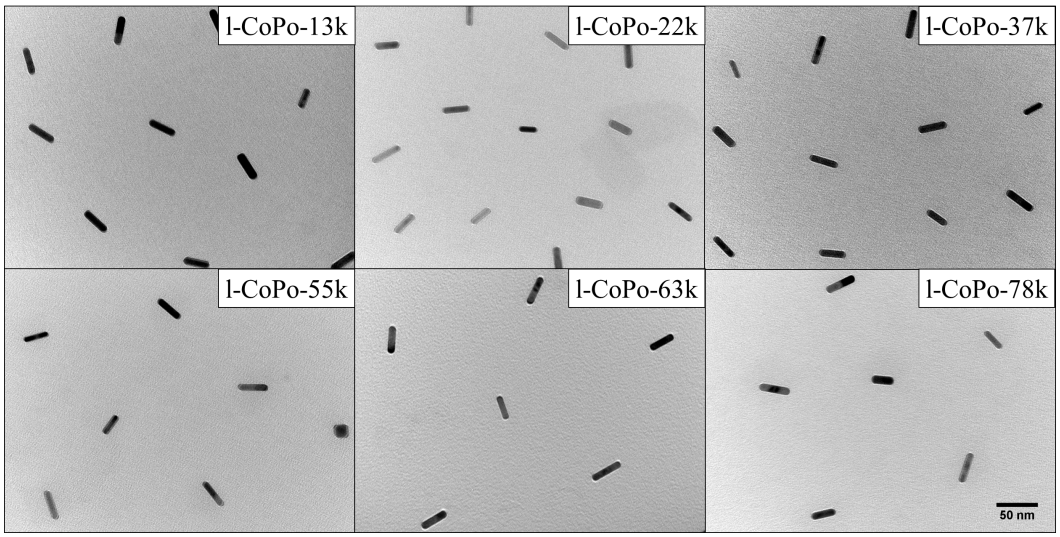

Fig. 6.4: TE micrographs of AuNRs functioanlized with linear NIPAM-*co*-AAM-polymers with various chain lengths. Scalebar (50 nm) is valid for all micrographs.

As we demonstrated previously, citrate-capped AuNPs can easily be functionalized by RAFT-polymers in grafting-to approaches.[12–14,16,17,19] Resulting grafting densities were generally found to be 0.2–0.4 RAFT anchor groups per nm^2.[16] Up to now, no direct grafting-to functionalization of gold nanorods using NIPAM-containing RAFT-polymers has been reported (see also Chapter 5).[165,251,252] Thus, AuNRs and the respective RAFT-polymers can be characterized separately from each other. Additionally, this approach offers a higher step efficiency and scalability than grafting-from strategies. For a detailed description of the functionalization procedure, see the Experimental Section 8. In general, ethanol solutions of the respective polymer were added to CTAB-capped Au nanorod solutions to destabilize the CTAB bilayer around the nanoparticle and functionalize the vacant surface site instantly with the polymeric material. The successful fabrication of individual core–shell nanostructures can be visualized by transmission electron microscopy (TEM). Here, TEM grids were drop-cast with aqueous solutions of the respective nanohybrids (see Figures 6.4 and 6.6).

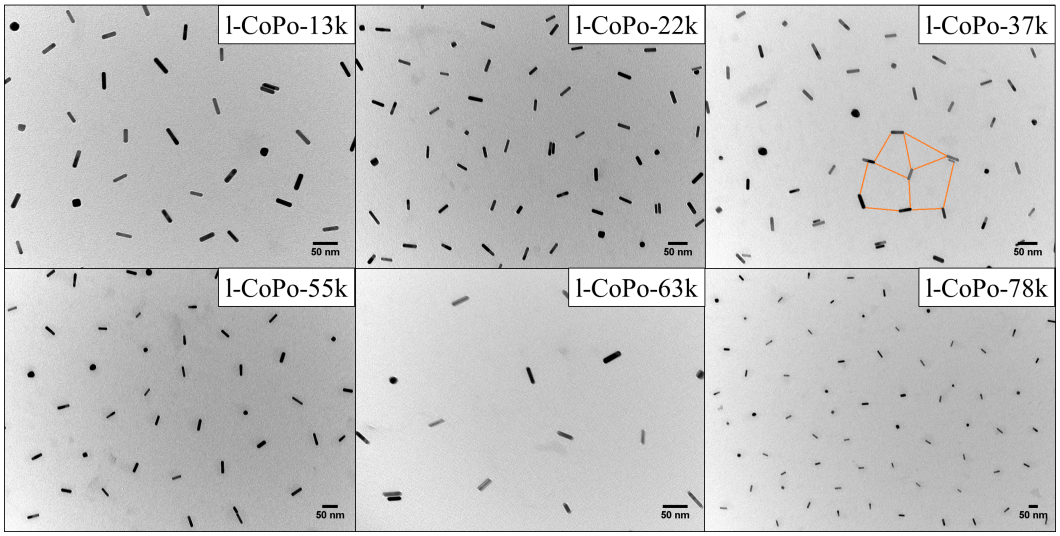

Fig. 6.5: Further TE micrographs of AuNRs functioanlized with linear NIPAM-*co*-AAM-polymers with various chain lengths.

Further micrographs are depicted in Figures 6.5 and 6.7. Due to its low electron density compared to the gold nanorods, the polymer shell cannot be seen directly. However, it keeps the AuNRs at specific distances depending on the molecular weight of the polymer grafted to the gold surface. By grafting different chain lengths to the gold nanorod, core distances can be tuned between 60 nm and 160 nm for linear copolymers and 70−120 nm for 3-arm star copolymers (for evaluation, see Figure 6.8). Previous studies could show that not all arms of star polymers are bound to the nanoparticle surface.[14,16] Compared to ~13 nm AuNPs functionalized with RAFT NIPAM homopolymers, spacings between Au nanorods are significantly increased at similar M_n values of the grafted poly(NIPAM).[12,14] *Ebeling et al.* showed that nanohybrid arrays can be formed by drop-casting using a volatile, organic solvent. This is likely to have less interaction with the polymer shell than water, which is used in this work. Generally, NIPAM polymers are well-known to swell in the presence of water, which may stretch the shell chains and therefore increase nanorod–nanorod spacings.[289,290] To the best of our knowledge, this is the first time that distances between small Au nanorods could be tuned over a wide range when different chain lengths were grafted onto the NR surface (see also Chapter 5).[106,107,245,291] Other Au nanorods functionalized with thermoresponsive shells could not be arranged into self-assembled nanostructures with a uniform spacing.[165,184] So

far, 2D arrays of AuNRs were only fabricated under the aid of prefabricated surfaces or matrices and by controlling the Debye length of AuNRs.[211,246–248]

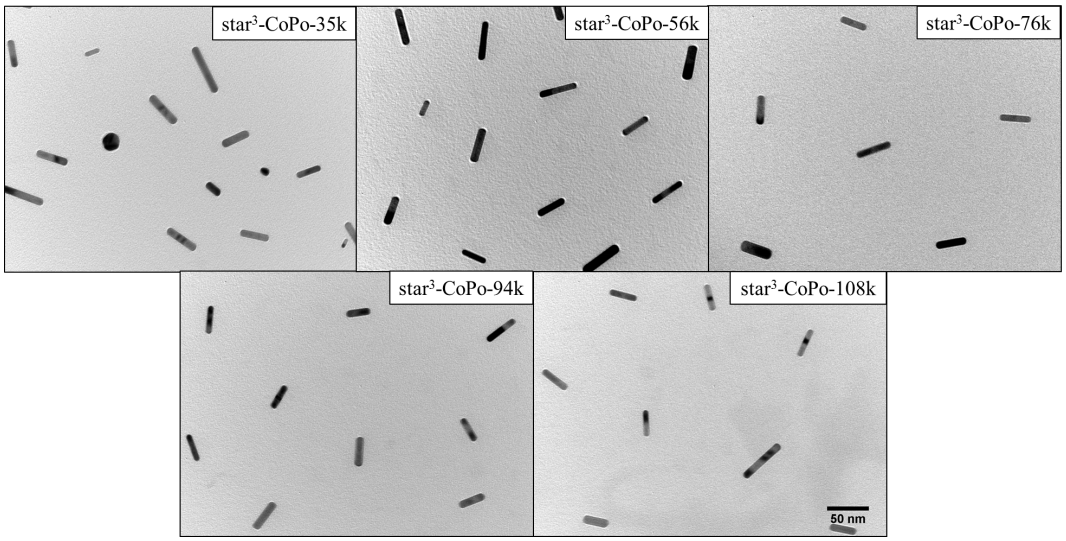

Fig. 6.6: TE micrographs of AuNRs functioanlized with 3-arm star NIPAM-*co*-AAM-polymers with various chain lengths. Scalebar (50 nm) is valid for all micrographs.

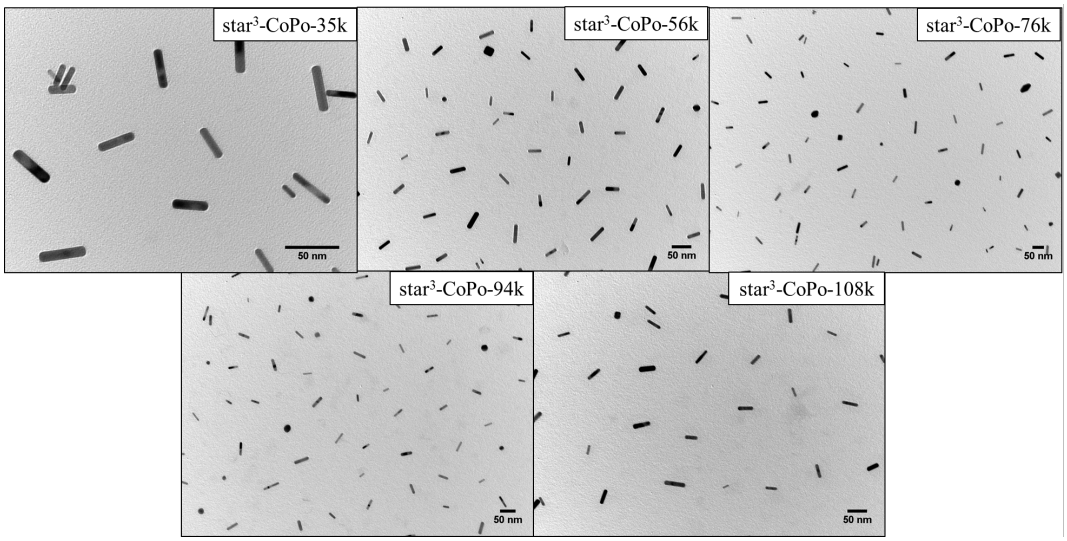

Fig. 6.7: Further TE micrographs of AuNRs functioanlized with 3-arm star NIPAM-*co*-AAM-polymers with various chain lengths.

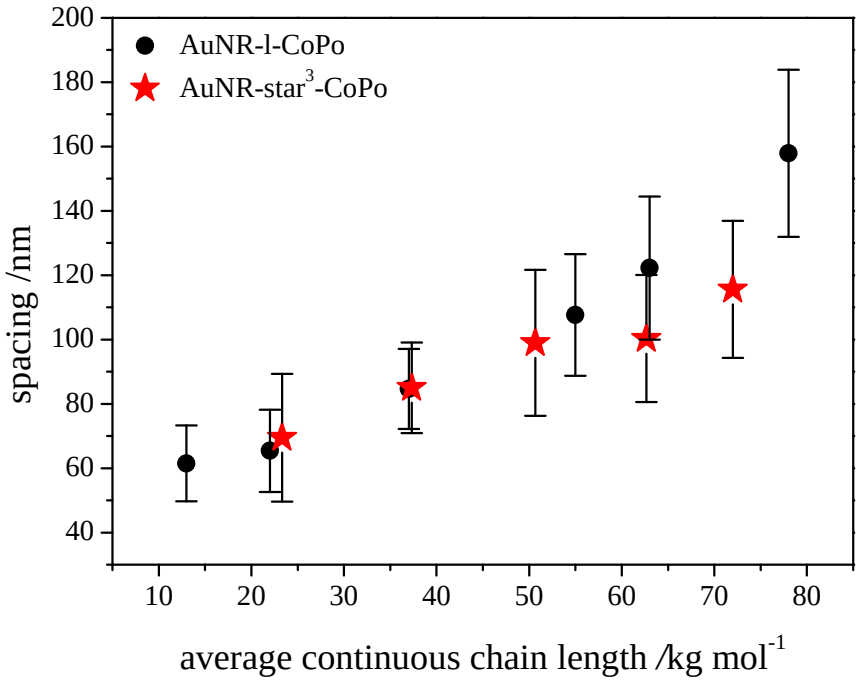

Fig. 6.8: Evaluation of AuNR spacing for linear (black) and 3-arm star-copolymers (red). M_n values for star-polymers were multiplied by $^2/_3$ obtaining the average continuous chain length to make both copolymer systems more comparable.

6.4 Solution Properties of Polymer–Metal Nanohybrids

6.4.1 Solution Properties of Nanohybrids in Pure Water

For further validation of the tunable size of the nanohybrids, size exclusion chromatography (SEC) measurements were performed. To mimic physiological conditions, experiments were conducted in water at 37 °C. Results are shown in Figure 6.9 (higher retention times correspond to smaller hydrodynamic diameters). For AuNRs functionalized with linear polymers, a clear shift of the peaks can be observed implicating the different dimensions of the respective nanohybrids. However, for 3-arm star nanohybrids, the trend is not as distinct

as for their linear counterpart. As seen in Figure 6.8 and reported in the literature,[16] the more arms a polymer has, the less is the absolute increase in nanohybrid shell size. When the molecular weight of the overall polymer is increased, monomeric units are distributed over three arms instead of one arm for monofunctional RAFT-polymers. Therefore, the absolute increase in size is not as pronounced as for linear copolymer nanohybrids. This can also be validated by comparing the hydrodynamic radii of pure linear and star^3 copolymers obtained from dynamic light scattering measurements (see Table 6.2 and Table 6.4). Here, the increase in hydrodynamic radius for 3-arm star copolymers at 37 °C is not as strong as for their linear counterpart, either.

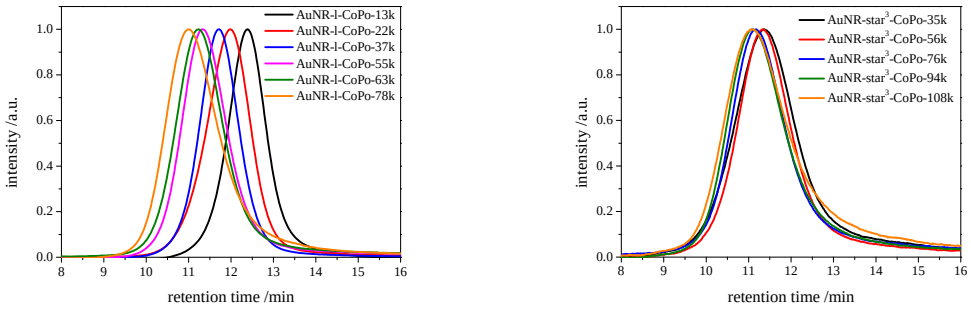

(a) **(b)**

Fig. 6.9: Size-exclusion chromatographs of linear **(a)** and 3-arm star **(b)** polymer nanohybrids in 0.05% NaN_3 aqueous solutions at 37 °C.

Dynamic light scattering is a common technique to investigate diffusional constants of particles. Generally, diffusion coefficients are highly dependent on the mass, shape, and surface chemistry since all parameters determine the particle–solvent interaction and consequently the Brownian motion. If particles obey the Stokes–Einstein equation, then a hydrodynamic diameter can be extracted.[259] In this context, AuNRs have been studied extensively in the literature.[260–262] Due to its rod-like shape, two peaks can be observed for AuNRs in the intensity distribution fit. They can be assigned to two different relaxation modes occurring for rod-shaped particles: (i) translational diffusion and (ii) the rotational diffusion of the nanorods. A common mistake in DLS analyses of these anisotropic particles is to assign the low-range intensity

distribution peak to small particle impurities. However, due to the anisotropy of nanorods, the Stokes–Einstein equation is not obeyed. Therefore, only diffusion coefficients can be determined, while hydrodynamic diameters cannot be extracted. Consequently, it is insufficient to take the intensity peak of the translational diffusion as an accurate measure for the actual size of the particles. However, studies from the literature suggest that the peak corresponding to the rotational diffusion is characteristic for the dimensions of the particle. *Liu et al.* showed that the rotational diffusion is highly affected by the aspect ratio of the NRs (AuNR length was held constant), while the translational diffusion was nearly unchanged, even though the mass of the particle increased with an increasing aspect ratio.[262] Consequently, only the rotational diffusion intensity peak shall be considered in the following (see Table 6.5).

Tab. 6.5: Pseudo rotational diameter of AuNRs functionalized with different linear and 3-arm star copolymers in nanopure water.[α]

sample	d_{rot} @ 25 °C / nm	d_{rot} @ 37 °C / nm
AuNR-l-CoPo-13k	4	4
AuNR-l-CoPo-22k	8	6
AuNR-l-CoPo-37k	10	8
AuNR-l-CoPo-55k	22	17
AuNR-l-CoPo-63k	26	19
AuNR-l-CoPo-78k	48	23
AuNR-star^3-CoPo-35k	15	14
AuNR-star^3-CoPo-56k	19	14
AuNR-star^3-CoPo-76k	21	21
AuNR-star^3-CoPo-94k	26	21
AuNR-star^3-CoPo-108k	35	30

[α] Larger diameters correspond to slower rotation velocities. All samples were applied to 5 centrifugation–redispersion cycles to remove any free polymer.

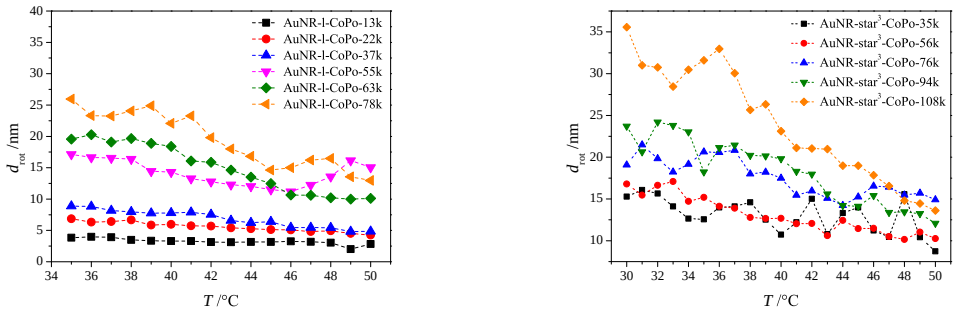

(a) **(b)**

Fig. 6.10: Dynamic light scattering experiments of linear polymer nanohybrids **(a)** and 3-arm star polymer nanohybrids **(b)** in nanopure water. The pseudo rotational diameters are plotted against temperature. All samples were applied to 5 centrifugation–redispersion cycles to remove any free polymer.

Here, an increase in pseudo rotational diameter is observed with increasing molecular weight of the grafted copolymer whereas this diameter decreases with increasing temperature. Lower diameters correspond to a higher rotational diffusion coefficient and hence higher rotation velocities of AuNRs. Figure 6.10 displays the pseudo rotational diffusion diameter of polymer-functionalized gold nanorods at different temperatures. In general, the "diameters" decrease with increasing temperature, while no distinct LCST can be observed. This can be attributed to a continuous collapse of the responsive polymer shell and therefore a less hindered rotation (Scheme 6.2).

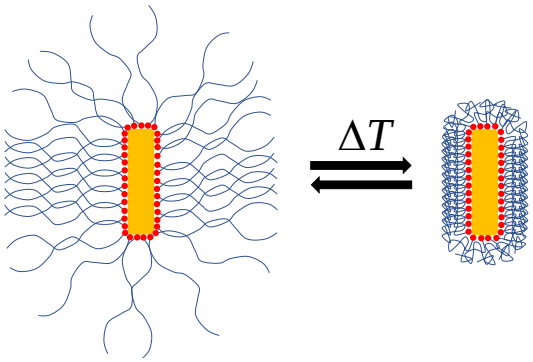

Scheme 6.2: Reversible shell collapse of gold nanohybrids upon heating/cooling in pure water.

Likewise, *Scherman et al.* described a similar behavior of poly(NIPAM)-functionalized gold nanoparticles.[292] Accordingly, the translational diffusion increased continuously with no sharp transition either. Similar to this work, the formation of aggregates was suppressed if no free macromolecular species were present. In the presence of a free polymer, a cooperative effect between the free and grafted polymer of the nanohybrid occurs leading to an aggregation of nanohybrids. Therefore, five centrifugation–redispersion cycles were conducted in this study to remove any residual copolymer. If no free polymer is present, then shell collapse is reversible (see Figure 6.11). Switching between 50 and 25 °C leads to either desorption or absorption of water from or into the copolymer shell. Both nanohybrid systems show that the differences between collapsed and swollen states become more pronounced with longer grafted polymer chains. This appears plausible since the overall size of the shell becomes larger with increasing molecular weight of the copolymer. This may result in more amide moieties available for H-bonded water molecules and consequently an enhanced swelling of the shell.

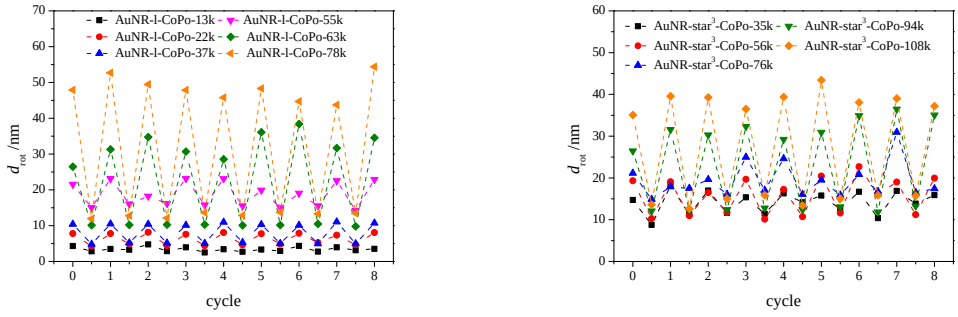

(a) **(b)**

Fig. 6.11: Temperature cycles of linear polymer nanohybrids **(a)** and 3-arm star polymer nanohybrids **(b)** in nanopure water switching between 25 °C (0, 1, and 2,...) and 50 °C (0.5, 1.5, and 2.5,...). The pseudo rotational diameters are plotted against the cycle number.

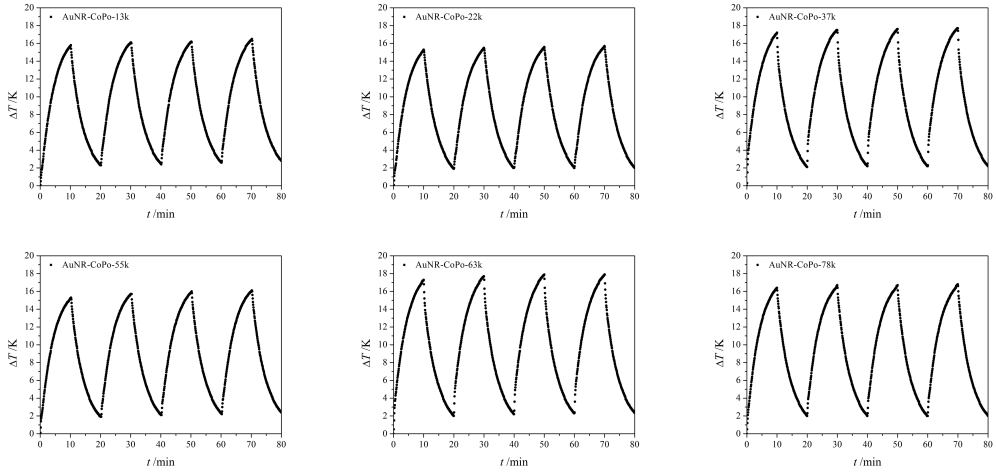

Fig. 6.12: Temperature profile of irradiated AuNRs functionalized with linear copolymers. Samples were illuminated for 10 min followed by a 10 min period without illumination. All samples were irradiated at an absorbance of at least ∼1.5 at 808 nm. To validate the performance of Au nanohybrids a control experiment was performed illuminating nanopure water only (see Figure 8.6).

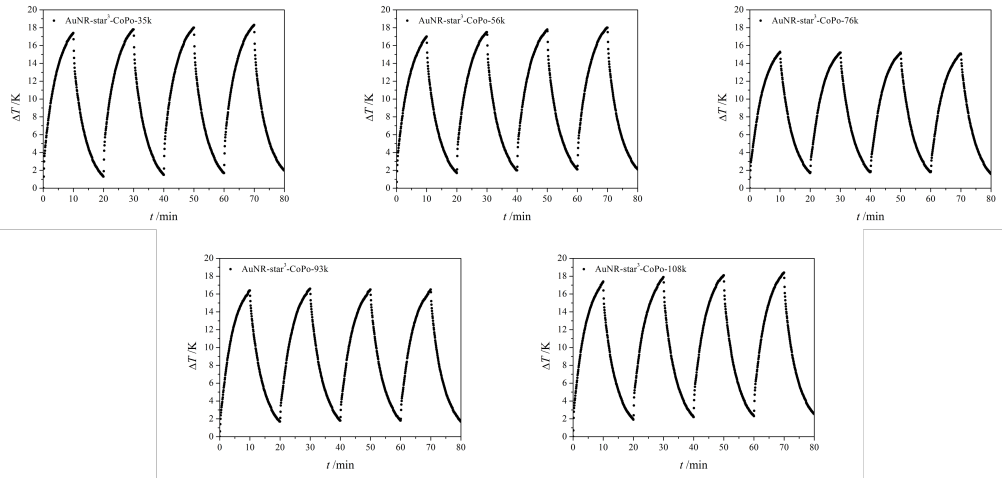

Fig. 6.13: Temperature profile of irradiated AuNRs functionalized with 3-arm star copolymers. Samples were illuminated for 10 min followed by a 10 min period without illumination. All samples were irradiated at an absorbance of at least ∼1.5 at 808 nm.

In DLS measurements, the desired temperatures were provided by a heating unit integrated in the DLS device. However, heat can also be generated *in situ* by illumination of the AuNR at the longitudinal LSPR using a laser diode (laser wavelength = 808 nm). The results of the respective cycles (see temperature *vs.* time curves in Figures 6.12 and 6.13) support the hypothesis that switching between collapsed and swollen states is reversible since the temperature increases do not become smaller along the cycles.

6.4.2 Solution Properties of Nanohybrids in a Simulated Blood Fluid

The most abundant protein in human blood plasma is human serum albumin (HSA, 35–50 mg mL^{-1}).[293] Its isoelectric point occurs at 4.7, which leads to a high negative charge under physiologically relevant conditions.[294,295] Due to its similar structure and properties, bovine serum albumin (BSA) is often used in laboratories instead of HSA.[296] To obtain an adequate simulated blood fluid (SBF), BSA was dissolved in a 0.1 M phosphate buffer (PBS). The ion concentrations and the pH level (pH = 7.5) are comparable to those present in human blood plasma.[297] Therefore, it appeared highly relevant to investigate the solution properties of gold nanohybrids under such conditions.[298] This should provide a more realistic forecast of how these core–shell structures would behave under physiological conditions.
Temperature-dependent DLS measurements were conducted to evaluate the influence of the buffer system and of BSA. Opposed to nanohybrids dispersed in nanopure water, nanohybrid aggregates were formed in the SBF above the LCST. This implies that the surface tension is significantly enhanced by buffer ions and BSA in contrast to nanopure water after surpassing the LCST. Aggregation is needed to reduce the surface area and therefore the free Gibbs energy. The respective correlation functions obtained from DLS before and after inducing the aggregation are depicted in Figures 6.14 and 6.15.

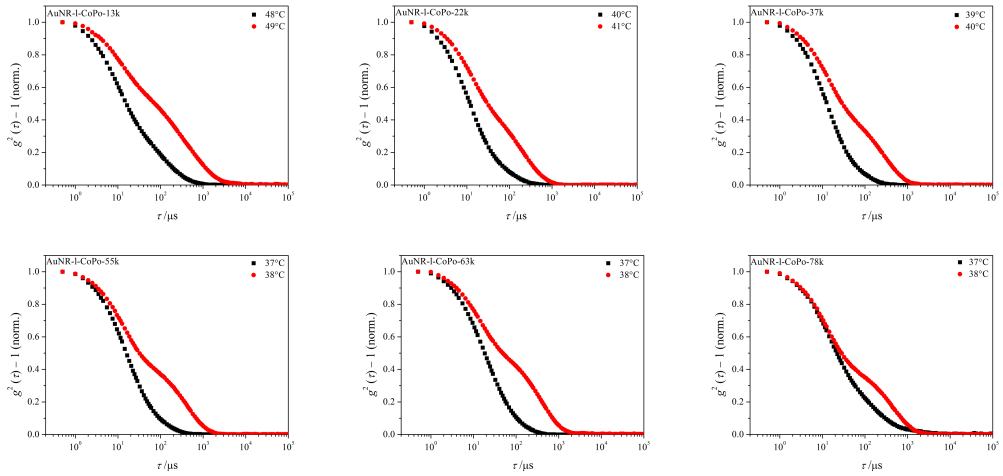

Fig. 6.14: Normalized correlation functions of AuNRs functionalized with linear copolymers before and after temperature-induced aggregation in buffered BSA (36 mg mL^{-1}) solutions. A clear shift in the correlation function is observed once aggregation has occurred.

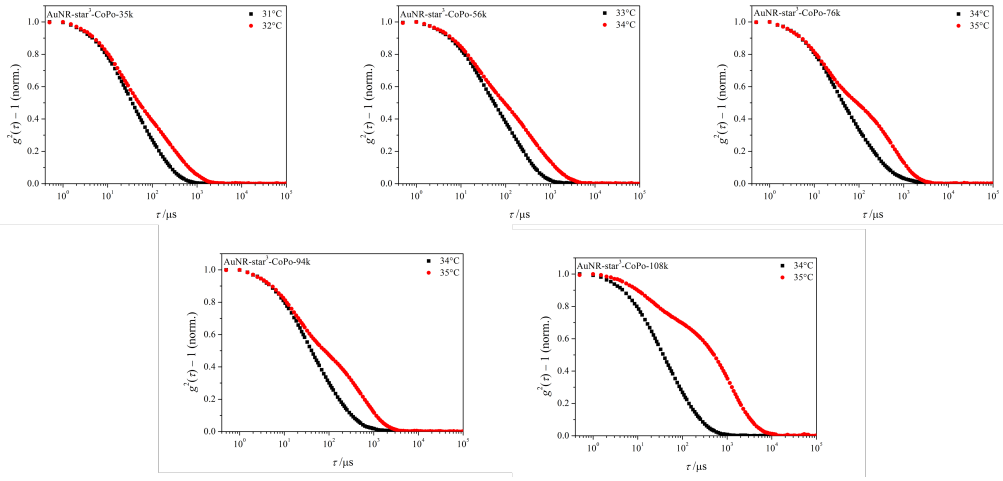

Fig. 6.15: Normalized correlation functions of AuNRs functionalized with 3-arm star copolymers before and after temperature-induced aggregation in buffered BSA (36 mg mL^{-1}) solutions. A clear shift in the correlation function is observed once aggregation has occurred.

Accumulated results are given in Figure 6.16. Here, a clear molecular weight dependence can be observed for both grafted copolymer systems. To evaluate the influence of BSA on the LCST, nanohybrid solutions with five different BSA concentrations (1–36 mg mL^{-1}) were investigated, while the nanohybrid concentration was held constant. Additionally, experiments with three different nanohybrid concentrations (corresponding to an absorbance $A = 0.3$–3.0 at λ_{long}) were performed at a constant BSA concentration. However, no influence on the respective LCSTs could be observed. For nanohybrids functionalized with linear polymers, LCST values become larger with decreasing average molecular weight, whereas LCST values for nanohybrids functionalized with 3-arm star polymers decrease at lower M_n. Both core–shell systems reach a certain limit where LCST values are no longer dependent on the molecular weight. The difference of 3 °C in the LCST between linear and star copolymer samples has already been observed with a free polymer in pure water (see Tables 6.2 and 6.4). Likewise, this can be explained by the less hydrophilic core and end-groups of the star polymer.

Tab. 6.6: Results of control experiments performing DLS measurements of both copolymer systems in 0.1 M phosphate buffer and BSA (36 mg mL^{-1}) for two different copolymer concentrations.

sample	T_{LCST} /°C @ 1 mg mL^{-1}	T_{LCST} /°C @ 0.1 mg mL^{-1}
l-CoPo-13k	46–47	50–52
l-CoPo-22k	40–41	44–46
l-CoPo-37k	38–39	41–42
l-CoPo-55k	37–38	40–41
l-CoPo-63k	37–38	39–41
l-CoPo-78k	37–38	38–40
star^3-CoPo-35k	34–35	37–39
star^3-CoPo-56k	36–37	37–39
star^3-CoPo-76k	36–37	37–39
star^3-CoPo-94k	36–37	37–39
star^3-CoPo-108k	36–37	37–39

Tab. 6.7: Results of control experiments performing DLS measurements of both copolymer systems in 0.1 M phosphate buffer for two different copolymer concentrations.

sample	T_{LCST} /°C @ 1 mg mL^{-1}	T_{LCST} /°C @ 0.1 mg mL^{-1}
l-CoPo-13k	46–47	47–48
l-CoPo-22k	41–42	41–42
l-CoPo-37k	39–40	39–40
l-CoPo-55k	37–38	37–38
l-CoPo-63k	37–38	37–38
l-CoPo-78k	37–38	37–38
star^3-CoPo-35k	34–35	35–36
star^3-CoPo-56k	35–36	36–37
star^3-CoPo-76k	36–37	36–37
star^3-CoPo-94k	36–37	36–37
star^3-CoPo-108k	36–37	36–37

Further measurements of the LCST were conducted for free copolymers in SBF and pure phosphate buffer solutions (see Tables 6.6 and 6.7). These data show that the behavior of the nanohybrids is mainly determined by the copolymer and influenced by the phosphate buffer, while it is not strongly affected by BSA. The hydrodynamic diameter obtained from DLS measurement of BSA in a buffered solution is depicted in Figure 6.17 indicating that no transition of the protein structure occurs within the considered temperature range up to ~50 °C. The influence of ions on the LCSTs of NIPAM-containing polymers and their respective mechanisms is described in the literature intensively.[190,195] However, previous studies do not provide suitable concepts for the contrary trends of the linear and star copolymer systems presented in this work. Based on theory proposed by *Cremer et al.* for the chain length dependency of the LCST of linear NIPAM homopolymers, an increased number of amide binding sites result in a lowered LCST.[190] Due to the sterically demanding isopropyl groups of two adjacent NIPAM units, amide–amide binding should be less facile in NIPAM homopolymers than the amide–amide binding for adjacent NIPAM

and AAM groups in the copolymer system presented in this work. Since amides in grafted polymers are possibly closer packed at higher molar masses, the effect should be increased in the long chain regime, which could explain the stronger chain length dependency with nanocomposites in contrast to linear NIPAM homopolymers.[190] However, the trend observed for 3-arm star copolymers (see Figure 6.16 **(b)**) cannot be explained by the same theory. Further studies are required to investigate this complex behavior in detail, which, however, is not the scope of this work.

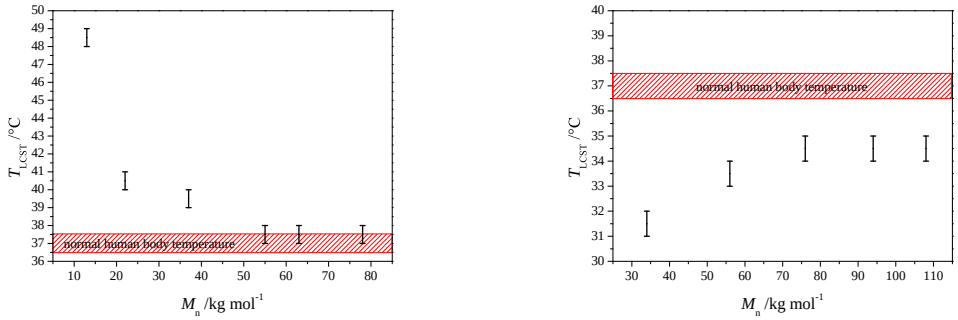

Fig. 6.16: LCSTs of linear polymer nanohybrids **(a)** and 3-arm star polymer nanohybrids **(b)** *vs.* the number average molar mass of the grafted polymer in buffered bovine serum albumin solutions (0.1 M PBS; BSA 36 mg mL^{-1}) obtained from DLS measurements.

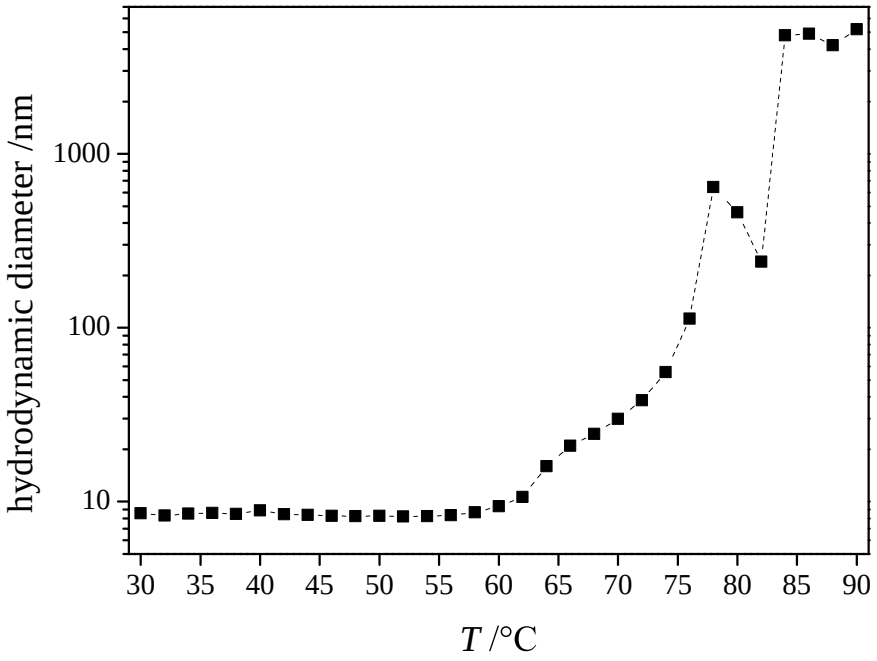

Fig. 6.17: Hydrodynamic diameter of BSA in a temperature range from 30–90 °C.

6.5 Remote-Controlled Aggregation of Polymer–Metal Nanohybrids

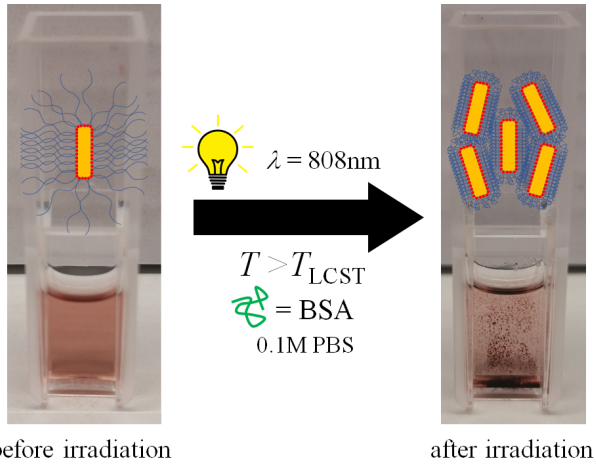

Scheme 6.3: Exemplary pictures of nanohybrids dispersed in the SBF before and after irradiation with a laser diode ($\lambda = 808$ nm at 300 mW).

Under healthy conditions, the human body is not able to generate a localized temperature increase over several degrees Celsius. Consequently, an external stimulus is required to trigger the shell response of gold nanohybrids and therefore its directed accumulation in certain parts of the body such as cancer ulcers. The intrinsic ability of gold nanorods to transfer light to heat can be utilized to provide this stimulus. AuNRs synthesized in this work (AR = 4.1, $\lambda_{long} = 810$ nm) are perfectly designed to absorb light within the first optical window of human tissues and convert the absorbed energy to heat, lifting the system to temperature above the LCST of the grafted polymer. Therefore, nanohybrids were irradiated with a laser diode at $\lambda = 808$ nm. Scheme 6.3 displays that the temperature response of Au nanohybrids, i.e., their aggregation/precipitation, can be remotely controlled by an external light supply.

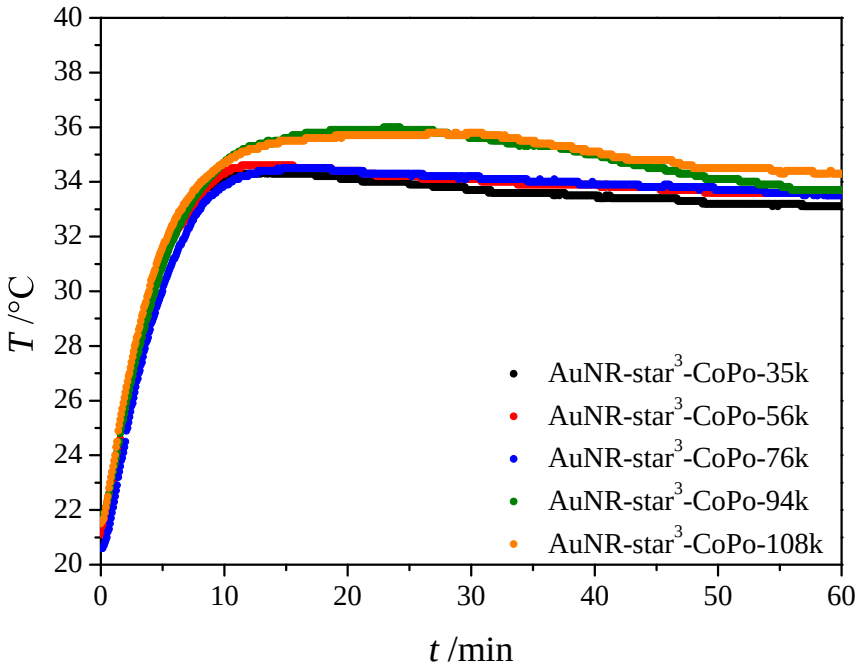

Fig. 6.18: Temperature profile of irradiated AuNRs functionalized with 3-arm star copolymers dispersed SBF. Solutions were irradiated by external light (300 mW, $\lambda = 808$ nm) for 60 min. The decrease in temperature is explained by the precipitation of aggregates (see Scheme 6.3) resulting in a decrease of absorbance within the illuminated area. AuNRs functionalized with linear copolymers were not investigated since the laser power was too weak to reach LCSTs for low M_n samples starting from room temperature.

Figure 6.18 shows the respective temperature profile of the nanohybrids dispersed in SBF within 60 min of irradiation. The increase in temperature triggered the aggregation of nanohybrids. Hence, the decrease in temperature after 15 min is explained by the precipitation of aggregates (see Scheme 6.3) resulting in a decrease of absorbance within the illuminated area.

6.6 Summary and Conclusion

In this chapter, core–shell nanostructures were fabricated by grafting various responsive RAFT copolymers on small gold nanorods. By simple drop-casting,

nanohybrids could be arranged into monolayered 2D self-assemblies with tunable nanorod–nanorod spacing depending on the chain length of the grafted copolymer. Dynamic light scattering experiments of aqueous nanohybrid solutions revealed that the rotational diffusion can serve as a relative measure for the size of the functionalized AuNRs. Measurements in pure water further demonstrated a continuous transition from a sponged to a more collapsed state along an increasing temperature indicating a gradual removal of incorporated water molecules out of the polymer shell. Opposed to that, nanohybrids dispersed in simulated blood fluids showed an abrupt LCST which could be tuned by altering the molecular weight and/or the topology of the copolymer even though the monomer composition was held constant. The aggregation of these nanohybrids in a simulated blood fluid could be triggered by irradiation at 808 nm in the optical window of human tissues due to the photothermal lifting above the LCST of the polymer shell. Overall, the presented approach offers a high potential for a remote-controlled, directed accumulation of gold nanorods in specific parts of the body and is therefore a promising candidate for photothermal therapeutics.

7 Final Conclusion and Outlook

As outlined in the preface, the initial aim of this thesis was to overcome the prejudice regarding the inherent viciousness assigned to polymers and small particulates. To demonstrate that both can be highly functional and useful in reality, distinct characteristics of metal nanoparticles and synthetic polymers were combined by developing tailor-made nanohybrids for the respective purpose. Specific applications in catalysis, hydrogen-storage, biosensing and photothermal cancer therapy could be addressed by making smart choices of suitable particles and macromolecules. Here, one determining factor to replace an established material with a new one relies on a superior performance. In addition, costs, production time and processability also play key roles in this context. Therefore, scalability and step-efficiency were always taken into account when paving a new route towards a functional hybrid material. Overall, it can be concluded, that all nanohybrid systems presented in this work are characterized by their outstanding and versatile performance along with their straightforward manufacturing process. In this regard, the RAFT-process has proved itself as an universal tool to tune the properties of polymeric materials and thus of polymer–metal nanohybrids by facile adjustment of parameters such as polymer composition, size and architecture.

In Chapter 3, an efficient design strategy to obtain a highly active, heterogeneous palladium nanocatalyst protected by a mesoporous silica shell was presented. Here, a great recyclability along with high yields in Heck-reactions were achieved. Future studies may address size-selective catalysis which provides specific routes for desired products in organic synthesis and petrochemical engineering.[299] Up to now, mostly zeolites and metal–organic frameworks (MOFs) are applied in these size discrimination syntheses since their pore sizes appear in a similar scale as small to medium sized organic molecules (< 1 nm, see Chapter 2).[122,300,301] Accordingly, *Huo et al.* encapsuled multiple small platinum nanoparticles into a zirconium-based MOF (pore size: 0.6 nm) and performed hydrogenation

reactions with olefins of different sizes.[302] The rate of conversion gradually decreased along the increasing molecular dimensions of the olefins. This concept may be transferred to the Pd–*m*Si nanohybrids presented in this thesis. Here, the pore sizes were found at ~4 nm which is too large to discriminate small organic reactants. Post-modification of these pores using tailored polymers may give rise to adjustable channel sizes towards the palladium core and thus to size/shape-selective catalysis depending on the polymer chain length. In this context, *Schmidt et al.* already demonstrated that NIPAM RAFT-polymers grafted to thin, mesoporous silica films could influence the transport of ions through these modified mesochannels.[163]

In Chapter 5 gold nanorods were coated with various RAFT-polymers of different topologies and arranged into 2D self-assemblies by a simple drop-casting technique. By taking further advantage of the high aurophilicity of sulfur, it is highly auspicious to use polymer-grafted gold nanorods as electrically conductive composite material within thin conductive polymer films. Here, future studies may address the immobilization of a conductive polymer like poly(3-hexylthiophene) (P3HT) bearing multiple sulfur-groups along the backbone.[303,304] The shape and size (34×8 nm) of the NRs fabricated in this thesis appear very promising to fit into lamellar structures (width = 11 nm) of microphase-separated P3HT-*b*-polystyrene block copolymers (P3HT-*b*-PS) similar to those fabricated by *Xiao et al.* and thus to enhance electric conductivities of its respective films.[305] Since the limiting factor in terms of electric conductivity of polymers originates from the interchain charge carrier transfer called *hopping*[306] gold nanocrystals could act as highly conductive wires between adjacent P3HT chains. Here, the cylindrical shape of NRs should be superior to overcome this obstacle opposed to spherical AuNPs.[307] Overall, this may compensate the loss in electric conductivity caused by the PS block which is needed for an enhanced processability of the material.[308,309] In this regard, first blending experiments were already conducted by the author using CTAB-capped gold nanorods and a modified P3HT. TEM and DLS analyses indicated the successful grafting approach of the conductive polymer onto the gold surface (see Figure 8.1 in Experimental Section 8).

In Chapter 6 it could be demonstrated that the agglomeration of gold nanohybrids can be triggered by an external NIR-stimulus in a simulated blood

fluid taking advantage of the lower critical solution temperature of the NIPAM-*co*-AAM copolymer grafted to the gold nanorod surface. Depending on the copolymer architecture and the molecular weight the LCST appeared to be tailorable over a wide temperature range. However, the mechanisms involved in the diverging behaviours between linear and 3-arm star polymers constructed from NIPAM and AAM builing units is not yet fully understood. Future studies may address further copolymer compositions with low and high ratios between both monomers to evaluate the role of acrylamide in the coil-to-globule transition upon heating. Chain length dependent investigations may provide further evidence about the influence of available inter- and intramolecular binding sites within this process. In this regard, the influence of the steric hindrance at the amide group of the comonomer to form hydrogen bonds could be investigated by using different comonomers. *N*-methyl acrylamide, *N*-ethyl acrylamide or *N*-*N*-dimethyl acrylamide would be potential candidates to increase the steric demand gradually at the amide group. Additional insights could be obtained by altering the end-groups of star copolymers to validate the hydrophobic effect on the LCST behavior. For this, the number of arms could be varied using 2-,3-,4- or 6-arm star RAFT-agents or more hydrophilic Z- and R-groups could to be linked to the initial star RAFT-agent. In general, other kosmotropic and chaotropic anions from the *Hofmeister* series of various concentrations could also be used to obtain further knowledge about the mechanism of the coil-to-globule transition of the respective copolymers.

Overall, this thesis has provided straightforward routes towards multiple novel nanohybrid materials with outstanding performances while giving new impulses for fundamental research and practical applications.

8 Experimental Section

8.1 Chemicals

If not indicated otherwise chemicals were purchased commercially from Sigma-Aldrich, Acros Organics, Fluka or ABCR. These chemicals were used without any further purification steps. AIBN was recrystallized from methanol at 30 °C obtaining thin needles and stored at 4 °C. *N*-Isopropyl acrylamide (see Figure 8.1 **(a)**) was recrystallized from toluene/hexane (3:1) twice and stored at 4 °C. The purity of recrystallized compounds was verified by NMR-spectroscopy. Nanopure water (type I) was obtained from a Millipore water purification system at an electrical resistivity of 18.2 MΩ cm.

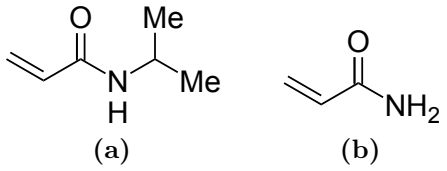

(a) **(b)**

Fig. 8.1: Chemical structure of **(a)** *N*-isopropylacrylamide (NIPAM) and **(b)** acrylamide (AAM) used as monomers in RAFT-polymerizations.

PEG-silanes with an average molecular weight $M_n = 5{,}000\,\mathrm{g\,mol^{-1}}$ and $M_n = 20{,}000\,\mathrm{g\,mol^{-1}}$ (see Figure 8.2) were purchased from Sigma-Aldrich.

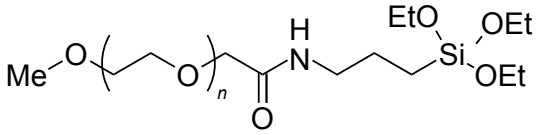

Fig. 8.2: Chemical structure of polyethylene glycol silane (PEG-silane).

Methyl-2-(((dodecylthio)carbonothioyl)thio)propanoate (l-CTA, see Figure 8.3) was received from *Christian Rossner* from the *Vana* group.

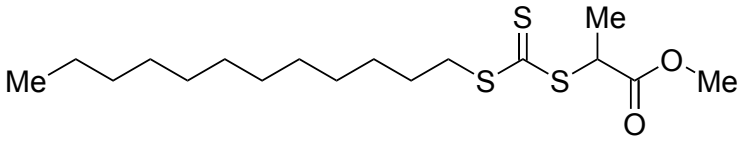

Fig. 8.3: Chemical structure of the RAFT-agent (l-CTA) used to synthesize linear RAFT-polymers.

Propane-1,2,3-triyl tris(2-(((propylthio)carbonothioyl)thio)propanoate) (star^3-CTA, see Figure 8.4) was received from *Christian Rossner* from the *Vana* group.

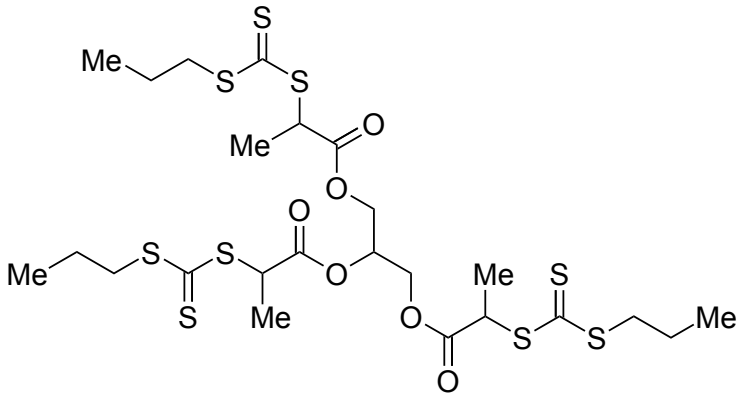

Fig. 8.4: Chemical structure of the 3-arm star-RAFT-agent (star^3-RAFT) used to synthesize 3-arm star RAFT-polymers.

8.2 Procedures

8.2.1 Synthesis of Metal Nanoparticles

Prior to any metal nanoparticle synthesis any glassware including the stirring bar and stoppers were cleaned using *aqua regia* and rinsed by demineralized water, acetone and nanopure water, respectively. Then the equipment was oven-dried at 130 °C over night.

8.2.1.1 Synthesis of CTAB-capped AuNRs

According to methods provided by *El-Sayed et al.* and *Chen et al.* small AuNRs were fabricated by a seedless growth method.[87,89]

Therefore, cetyltrimethylammoniumbromide (CTAB, 3.644 g, 10 mmol) was dissolved under smooth stirring (150 rpm) in nanopure water (95 mL) at 28 °C. Subsequently, the flask was covered in aluminum foil protecting the solution from any radiation. Afterwards, an aqueous 10 mM $HAuCl_4 \cdot 3\,H_2O$ solution (5 mL) was added followed by $AgNO_3$ (4 mM, 3 mL) solved in water. To this mixture concentrated hydrochloric acid (120 µL) was introduced. Under elevated stirring (300 rpm) a 85.8 mM solution of an aqueous solution of ascorbic acid (750 µL) was added. Once the solution turned from orange, to yellow to colorless an ice-cold aqueous solution of $NaBH_4$ (25 mM, 30 µL) was given to the solution. After 10 s, stirring was reduced to 150 rpm and maintained for 5 h. To purify CTAB-capped AuNRs 20 mL of the AuNR-sol were centrifuged at 15,000 *g* for 30 min at 35 °C. Afterwards, the supernatant was discarded and the precipitate was redispersed in a 2 mM CTAB solution (15 mL, 40 °C). Then two further centrifugation–redispersion cycles were conducted. After the third centrifugation step the precipitate was redispersed in nanopure water (30 mL, 40 °C).

8.2.1.2 Synthesis of Citrate-capped Au-NPs

The basic strategy to synthesize gold nanoparticles capped by citrate ions was established by *Turkevich et al.*[62] Studies by *Ebeling* and *Vana* improved this procedure.[12,67]
In a general synthesis, $HAuCl_4 \cdot 3\,H_2O$ (19.7 mg, 50 µmol) was added to boiling nanopure water (96 mL) under vigorous stirring. A boiling solution of sodium citrate (57.3 mg, 194 µmol) in water was given to the gold solution and stirred for further 15 min. Afterwards the solution was cooled down to room temperature slowly. The final red solution was stored in PP tubes in the dark at room temperature.

8.2.1.3 Synthesis of CTAB-capped PdNCubes

According to *Xu et al.* palladium nanocubes (PdNCubes) can be synthesized using CTAB as capping agent and ascorbic acid as reducing agent.[32,58]
CTAB (45.5 mg, 12,5 mmol, 2500 eq.) was solved in nanopure water (10 mL) and heated at 95 °C for 5 min. Under vigorous stirring, 0.5 mL of an aqueous 10 mM H_2PdCl_4 solution (1.25 mg, 0.005 mmol, 1.0 eq.) was added. Meanwhile,

a freshly prepared aqueous solution of acorbic acid (100 mM) was also heated at 95 °C. After 5 min 80 µL of the ascorbic acid solution (1.41 mg, 0.008 mmol, 1.6 eq.) was given to the metal solution. After 10 s the solution turned from orange to brown. The reaction was allowed to proceed for further 30 min. The as-obtained solution was stored in PP tubes in the dark at room temperature. Attempts to scale up the reaction were successful using the 10-fold amount of each chemical.

8.2.1.4 Seed-Mediated Growth of Larger PdNCubes

According to *Xu et al.* the 18 nm PdNCubes can be further applied to a seed-mediated growth to obtain larger PdNCubes. Hereby, the size can be tuned by the ratio between seed- and feed solution.[32,58]
Therefore, an aqueous 10 mM H_2PdCl_4 solution (1.25 mL) was added to a 50 mM CTAB water solution (50 mL) at 40 °C and stirred for 30 min. Then different volumes (2000 µL for 39 nm or 400 µL for 67 nm PdNCubes) of the as-obtained 18 nm PdNCubes were given to the feed solution and stirred for further 5 min. Afterwards, a freshly-prepared 100 mM ascorbic acid solution (250 µL) was added under stirring (400 rpm for further 10 s). The resulting solution was incubated at 40 °C for at least 18 h and shut down by centrifugation at 30 °C for 20 min (7000 *g* for 39 nm and 3000 *g* for 67 nm PdNCubes). The respective precipitate was redispersed in a 2 mM CTAB solution (20 mL, 40 °C) and stored in the dark.

8.2.2 Synthesis of Mesoporous Silica Coating on PdNCubes

Matsuura and *Gorelikov* outlined a general procedure to coat CTAB-capped nanoparticles with a mesoporous silica shell.[215] This single-step synthesis procedure was performed using AuNRs and CdSe/ZnS quantum dots. This approach was adapted to CTAB-capped PdNCubes.
To remove the excess of surfactant (CTAB) from the as-obtained PdNCubes 20 −25 mL of the Pd-sol were centrifuged at 15,000 *g* at 30 °C for 30 min. After discarding the supernatant the precipitate was redispersed in nanopure water (10 mL) to yield a concentration of $\sim 10^{15}$ particles per liter. Under smooth shaking a 0.1 M solution of NaOH (100 µL) was added. Afterwards, two

injections of pure TEOS ($2 \times 6\,\mu L$) were introduced at 30 min time intervals under gentle vortexing. Then, the mixture was incubated for 2 days without moving at room temperature.

8.2.3 PEG-Functionalization of Pd–*m*Si-Nanohybrids and Preparation of the Nanocatalytic System

The respective PEG-silane ($M_n = 5{,}000\,g\,mol^{-1}$ and $M_n = 20{,}000\,g\,mol^{-1}$) was solved in a mixture of ethanol and nanopure water (10:1, $10\,mg\,mL^{-1}$). Then, 1 mL of this solution was given directly to the Pd–*m*Si nanohybrid solution under ultrasonication. The mixture was incubated over night under vigorous shaking. Afterwards, two aliquots were combined to yield ~2.6 mg palladium per sample (determined by ICP-MS). To remove the solvent the mixture was centrifuged at 12,000 *g* (30 °C) for 60 min and the supernatant was discarded. The precipitate was redispersed in methanol under ultrasonication. PEG-2000 (1 g) was solved in this solution and the whole mixture was precipitated into a Teflon tube filled with an excess of cold diethyl ether. This suspension was centrifuged for 20 min (5 °C) at 6,000 *g* and the supernatant was discarded afterwards. To remove residuals of diethyl ether the sample was dried under reduced pressure, purged with an argon stream and then transferred to the glove box (argon).

8.2.4 Heck-Cycles Using Pd–*m*Si–PEG-5k as Nanocatalyst

A typical synthesis was conducted as follows: To the Pd–*m*Si-PEG-5k (~2.6 mg palladium, 0.024 mmol, 0.044 eq.) dispersed in PEG-2000 (1.0 g, 1.0 mol, 1800 eq.) *p*-iodoanisole (130 mg, 0.56 mmol, 1.0 eq.), ethyl acrylate (110 mg, 1.1 mmol, 2.0 eq.) and sodium phosphate (180 mg, 1.1 mmol, 2.0 eq.) were given. The Teflon tube was then transferred to an aluminum bead bath and heated at 110 °C for 24 h. The mixture was vigorously stirred over the period of the reaction. To shut down the reaction the tube was removed from the bath and cooled down. Afterwards, diethyl ether (20 mL) was added to the mixture and stirred for 15 min to extract the product. The suspension was centrifuged at 10 °C for 20 min at 6,000 *g*. The supernatant was removed by a syringe and

passed through a PTFE filter (pore size: 0.45 µm) before the diethyl ether and the residual ethyl acrylate was removed in vacuo. This extraction process was conducted two further times. The Pd–*m*Si–PEG-5k nanocatalyst and the PEG-2000 was recovered and degassed afterwards. Finally, the mixture was transferred to the glove box again to conduct the next Heck-reaction. Likewise, seven further catalysis–recovery-cycles were performed.

8.2.5 RAFT-polymerization Procedures

To obtain polymeric material the monomer, the respective RAFT-agent and 1,4-dioxane were given into a glass vial. A solution of AIBN in 1,4-dioxane was prepared which was then transferred to the monomer–RAFT-solution. After sealing the vial with a septum the solution was purged with argon for 30 minutes. The solution was put into a heating block at 60 °C for certain time periods, respectively. To shut down the reaction the solution was subjected to the ambient air and precipitated in cold diethyl ether. The suspension was centrifuged for 20 minutes at 5 °C, decanted and solved in acetone afterwards. This centrifugation procedure was repeated two further times.

8.2.6 Synthesis of Polymer–Metal Nanohybrids

The functionalizations of metal nanocrystals were performed in 50 mL PP tubes according to an adapted procedure published by *Ebeling* and *Vana*.[12,67] Therefore, 10 mg of the respective RAFT-polymer was solved 5 mL nanopure water and added to the respective metal-sol (5 mL of the purified AuNR sol, 5 mL of the as-obtained PdNCube sols) under smooth shaking. Afterwards, 20 mg of the polymer were solved in ethanol (5 mL) and given to the respective sol under the aid of ultrasonication (37 kHz, 80 W) at room temperature. The mixture was incubated over night in the dark at room temperature. The polymer–metal nanohybrids were separated from excess polymer and capping agents by at least three centrifugation–redispersion steps.
For the PdNCubes with different sizes, *g*-force had to be adapted to the respective size of the nanocube to avoid aggregation. For the PdNCube seeds a force of 8,000 *g*, for 39 nm-NCubes 3,000 *g* and for 67 nm-NCubes 1,500 *g* was applied at 15 °C for 2 h each. Pd nanohybrids were dispersed in ethanol to yield concentrations of $\sim 0.6\,\mathrm{mg\,ml^{-1}}$ after these cycles.

For AuNRs functionalized with NIPAM homopolymer centrifugational force was set at 8,000 g for all samples at 5 °C for 2 h. Finally, the precipitate was redispersed in EtOH (2 mL).
The copolymer-grafted AuNRs were separated from the excess polymer and capping agents by five centrifugation–redispersion steps (each: 5 °C, 10,000 g, and 4 h). Samples were redispersed in nanopure water (20 mL) under cautious (5 s intervals) ultrasonication (37 kHz, 80 W) between the cycles. After the last step, samples were redispersed in nanopure water (1.2 mL) and stored in the dark.
To functionalize CTAB-capped gold nanorods with P3HT-OH 10 mg of the polymer was solved in THF and added to the purified AuNR sol (4 mL) under ultrasonication. The mixture was incubated over night and purified by two centrifugation–redispersion cycles in THF (15 °C, 2,000 g, and 1 h).

8.2.7 Synthesis of AuNR-Planet−AuNP-Satellite Structures

To 0.2 mL of a AuNR solution functionalized with 3-arm star RAFT-polymers, 4.8 mL ethanol were added. Under ultrasonification 2.6 mL of the AuNP-solution (∼ 13 nm) were given to the mixture and incubated for 30 min. To prevent aggregation of the nanohybrids, 5 mL of a 5 mg mL^{-1} solution of the linear RAFT-polymer NIPAM-3 in ethanol were added and incubated for further 30 min. To separate free Au-NPs and linear RAFT-polymer from planet–satellite nanohybrids three centrifugation–redispersion steps (2×, 500 g, 1 h, 5 °C) were performed.

8.2.8 Future Perspective: Poly(3-hexylthiophene)-Coated AuNRs

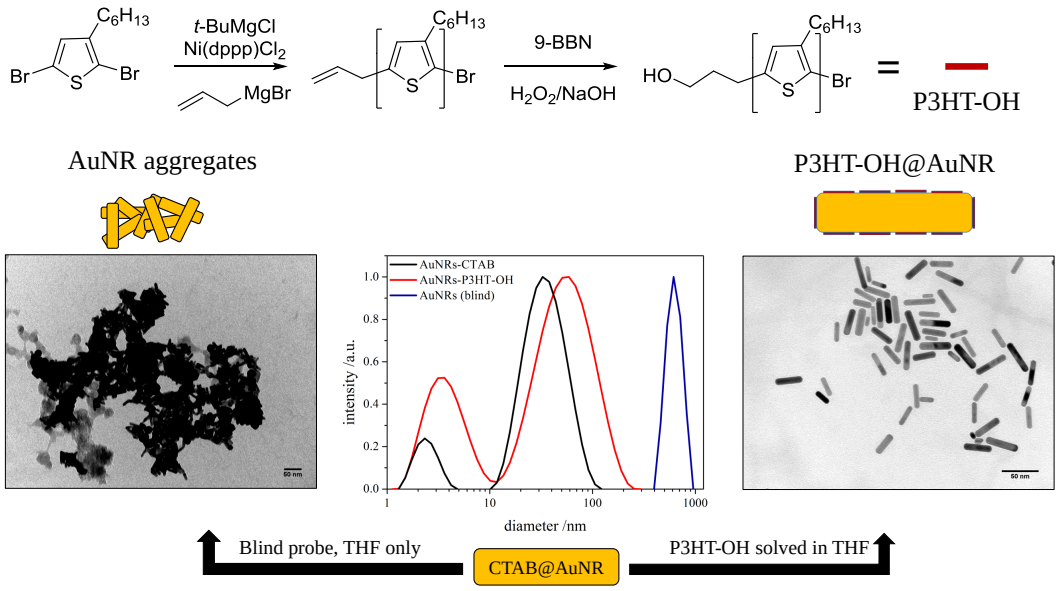

Scheme 8.1: Synthesis route of poly(3-hexylthiophene) terminated with an alcohol group (P3HT-OH), TEM images and DLS distributions of P3HT-OH-grafted AuNRs *versus* a blind probe. DLS results demonstrate the successful immobilization of P3HT-OH onto AuNRs since both rotational and translational diffusion components are still present whereas the blind probe shows a high degree of agglomeration.

Poly(3-hexylthiophene) terminated with an alcohol group (P3HT-OH) was provided by *Stella Weber* from the *Vana* group. As depicted in Scheme 8.1 P3HT-OH was synthesized over a Grignard metathesis of 2,5-dibromo-3-hexylthiophene and subsequently functionalized with an allylmagnesium bromide and transformed by a hydroboration to yield an alcohol group for further modification steps. The average molecular weight was determined at 6,000 $g\,mol^{-1}$ with a dispersity $Đ = 1.23$. The obtained polymer could be applied in a functionalization approach using gold nanorods from aqueous solution. The P3HT-OH was solved in THF (2 mL, 4 $mg\,mL^{-1}$) and given directly to the gold sol (4 mL). Afterwards, two centrifugation–redispersion cycles (15 °C, 2000 g, 90 min) were applied to remove CTAB and the excess of P3HT-OH. TEM and DLS results indicate a successful immobilization of

P3HT-OH onto the gold surface. The P3HT-OH grafted onto AuNRs should offer the needed dispersibility in bulk P3HT while preventing the formation of larger NR aggregates.

8.3 Instruments

8.3.1 Size-Exclusion Chromatography (SEC)

SEC measurements of polymers were conducted at 45 °C using DMAc as eluent containing 0.1 % LiBr on a Agilent 1260 Infinity SEC system. The device consists of a PSS GRAM precolumn (8×50 mm, particle size: 5 µm), three separation columns (PSS SDV, 8×300 mm, particle size: 5 µm, pore size: 30 Å, 10^3 Å und 10^3 Å), an Agilent RI detector and an Agilent UV/vis detector operating at $\lambda = 310$ nm. Experiments were performed at a flow rate of 0.8 mL min^{-1} using PMMA standards with low dispersities. All samples were prepared using a concentration of ~ 5 g L^{-1} and filtered through a 0.45 µm PTFE filter before injecting the respective solution into the system.
SEC measurements of polymer–metal nanohybrids were conducted at 37 °C using nanopure water as eluent containing 0.05 % NaN_3. Experiments were performed by *Stella Weber* on an UltiMate 3000 from Thermo Fisher Scientific. The device consists of an UltiMate LPG-3400SD HPLC pump, an UltiMate WPS-3000TSL autosampler and separation column (PolySep-GFC-P 5000, 7.8×300 mm) from Thermo Scientific Dionex. A Thermo Scientific UltiMate VWD-3400RS UV/vis detector was used operating at $\lambda = 520$ nm. Experiments were performed at a flow rate of 0.6 mL min^{-1}. All samples were prepared by filtering the respective solution through a 0.8 µm cellulose filter before injecting into the system.

8.3.2 Transmission Electron Microscopy (TEM)

TEM analyses were performed on a Philips CM 12 TEM operating at an acceleration voltage of 120 kV and an emission current of $3 - 4 \times 10^6$ A. The focused electron spot has a diameter of 10^{-6} m. Within the condenser lens a 5×10^{-5} m aperture was used. To block all scattered electrons a aperture with a diameter of 2×10^{-5} m was employed. An Olympus 1376 × 1032 pixel CCD

camera served as detector. All samples were prepared by drop-casting and slow evaporation of the solvent. Therefore, samples were given on a Plano 200 mesh copper TEM grid with an amorphous carbon film. These grids were cast by one drop using a Eppendorf-pipette ($\sim 20\,\mu L$). The grid was immediately covered by a glass vial to ensure slow evaporation. TE micrographs were analyzed by the software ImageJ.

8.3.3 Dynamic Light Scattering (DLS)

DLS measurements were performed on a Malvern Zetasizer Nano S system using a wavelength of 633 nm at a scattering angle of 173 °. Diluted samples of the nanohybrids were prepared 24 h prior measurements and left in the dark without moving. Samples were measured 12 times for 60 s each at 25 °C after a 120 s equilibration period within the analyzer.

8.3.4 Nuclear Magnetic Resonance (NMR)

Nuclear magnetic resonance (NMR) spectra were taken on a Bruker AMX-300. Samples were prepared in the respective deuterated solvent ($\sim 20\,mg\,mL^{-1}$). Each spectrum was referenced to the residual signal of the solvent.

8.3.5 Atomic Force Microscopy (AFM)

Atomic force microscopy (AFM) experiments were performed on a Veeco/Digital multimode 8 AFM instrument equipped with a NanoScope V controller. Measurements were conducted using the software Nanoscope (version 8.15) while operating within the "ScanAsystHR in Air" mode. As cantilever a SCANASYST-AIR-HR (silica tip on nitride arm, resonance frequency: $130 \pm 30\,kHz$, spring constant: $0.4\,N\,m^{-1}$, tip radius: 0.995 nm, Bruker AFM Probes) was used. AFM experiments were conducted by *Torsten Fornefeld*. To process obtained micrographs the software NanoScope Analysis (version 1.40) was used.

8.3.6 Inductively Coupled Plasma Mass Spectrometry (ICP-MS)

Inductively Coupled Plasma Mass Spectrometry (ICP-MS) measurements were performed on a ThermoFisher Scientific iCAP-Q ICPMS equipped with a Peltier-cooled cyclonic quartz glass spray chamber and a PFA microconcentric nebulizer operating at a flow rate of $100\,\mu L\,min^{-1}$. Solutions to be analyzed were supplied with an Elemental Scientific SC-FAST system which was connected to an Elemental Scientific SC-DX autosampler. Palladium-specific calibration measurements were conducted to guarantee an adequate data quality. ICP-MS measurements were conducted by *D. L. Hoffmann* and *Prof. M. Willbold* from the Isotope Geology Department of the Georg-August-University Göttingen. Heck-reaction samples were prepared by solving the catalysis product in diethyl ether (5 mL) and extracting potential residues of palladium with 0.5 M HCl ($5 \times 2\,mL$).

8.3.7 Light-Induced Heating

The device to perform light-induced heating experiments is depicted in Figure 8.5. It consists of a measuring unit, a control panel and thermometer. Samples are filled into a cuvette ($L = 1\,cm$, $d = 0.5\,cm$) which has a fixed position on the measuring unit. The respective laser diode is attached to an adjustable metal board so that the distance between the cuvette and the diode can be varied. Depending on the optical properties of the sample two different diodes can be used:

Tab. 8.1: Laser diodes used for light-induced heating experiments

	LCU80E053Ap/Dp LD-808	LCU80E061Ap LD-830
Lasing wavelength	$805 - 811\,nm$	$820 - 840\,nm$
Optical output	$0 - 300\,mW$	$0 - 300\,mW$
Parallel beam divergence	$8°$	$8° - 13°$
Perpendicular beam divergence	$28°$	$17° - 22°$

The sample temperature was measured *via* a VOLTCRAFT K202 thermometer and recorded over time using the respective SE305 software (version 3.7.0.0). Light-induced heating measurements were conducted in a 1×0.5 cm polypropylene cuvette filled with 0.55 mL of the respective sample. The distance between cuvette and diode was held constant at 2 cm which resulted in an illuminated area of approximately 1×0.5 cm. All experiments wer performed at a laser power of 300 mW. Figure 8.6 displays the temperature increase of nanopure water during 10 min of irradiation as control experiment.

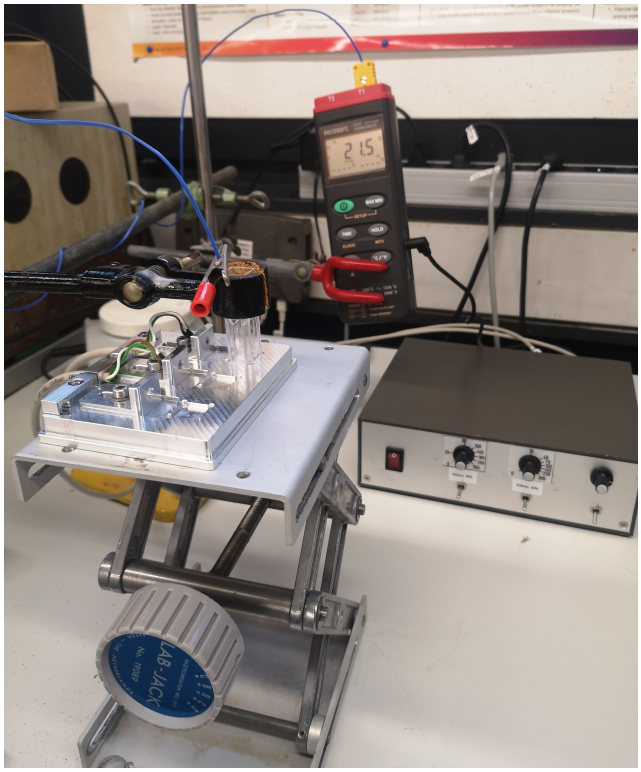

Fig. 8.5: Experimental setup to perform light-induced heating measurements.

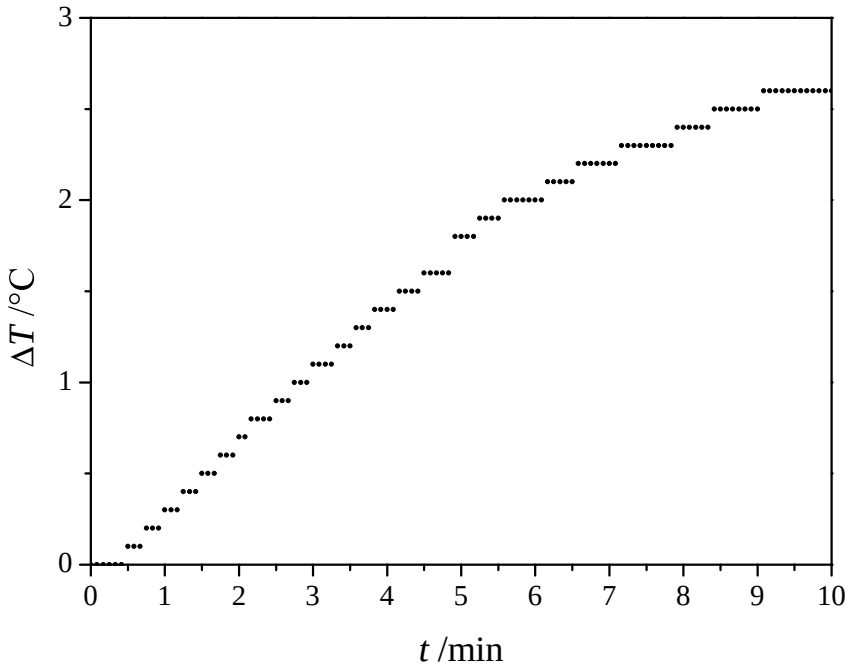

Fig. 8.6: Control experiment of nanopure water showing the temperature increase within 10 min of irradiation.

9 Bibliography

[1] G. Naumov, *Anthropos* **2013**, *108*, 97–116.

[2] M. T. Jerrentrup, *J. Philos. Cult. Rel.* **2020**, *49*, 20–28.

[3] L. Sasso, *Capital structure and corporate governance: the role of hybrid financial instruments*, *Vol. 21*, Kluwer Law International BV, **2013**.

[4] M. Kraushaar, D. Lambach, *ACPACS Occasional Paper* **2009**, *14*, 1–20.

[5] U. Keller, C. Enderle, T. Gödecke, G. Henning, *Diesel Hybrid–The Next Generation of Hybrid Powertrains by Mercedes-Benz*, Daimler AG, **2012**.

[6] N. Aich, J. Plazas-Tuttle, J. R. Lead, N. B. Saleh, *Environ. Chem.* **2014**, *11*, 609–623.

[7] M. Carus, *Renewable Carbon - Key to a Sustainable and Future-Oriented Chemical and Plastic Industry*, NOVA Institute, **2020**.

[8] A. L. Andrady, *Mar. Pollut. Bull.* **2011**, *62*, 1596–1605.

[9] C. M. Rochman, M. A. Browne, B. S. Halpern, B. T. Hentschel, E. Hoh, H. K. Karapanagioti, L. M. Rios-Mendoza, H. Takada, S. Teh, R. C. Thompson, *Nature* **2013**, *494*, 169–171.

[10] C. A. Pope III, D. W. Dockery, *J. Air Waste Manag. Assoc.* **2006**, *56*, 709–742.

[11] T. Banerjee, V. Murari, M. Kumar, M. Raju, *Atmos. Res.* **2015**, *164*, 167–187.

[12] B. Ebeling, P. Vana, *Macromolecules* **2013**, *46*, 4862–4871.

[13] C. Rossner, B. Ebeling, P. Vana, *ACS Macro Lett.* **2013**, *2*, 1073–1076.

[14] C. Rossner, P. Vana, *Angew. Chem. Int. Ed.* **2014**, *53*, 12639–12642.

[15] C. Rossner, V. Roddatis, S. Lopatin, P. Vana, *Macromol. Rapid Commun.* **2016**, *37*, 1742–1747.

[16] C. Rossner, Q. Tang, O. Glatter, M. Müller, P. Vana, *Langmuir* **2017**, *33*, 2017–2026.

[17] C. Rossner, P. Vana, O. Glatter, *Macromolecules* **2017**, *50*, 7344–7350.

[18] Q. Tang, C. Rossner, P. Vana, M. Mueller, *Biomacromolecules* **2020**, *21*, 5008–5020.

[19] W. Peng, C. Rossner, V. Roddatis, P. Vana, *ACS Macro Lett.* **2016**, *5*, 1227–1231.

[20] J. Wagner, W. Peng, P. Vana, *Polymers* **2018**, *10*, 407.

[21] D. Rohleder, MSc thesis, Georg-August University Goettingen, **2018**.

[22] Y. Cai, W. Peng, S. Demeshko, J. Tian, P. Vana, *Macromol. Rapid Commun.* **2018**, *39*, 1800226.

[23] A. N. Shipway, E. Katz, I. Willner, *Chem. Phys. Chem.* **2000**, *1*, 18–52.

[24] C. Wronski, *Brit. J. Appl. Phys.* **1967**, *18*, 1731.

[25] A. P. Alivisatos, *Science* **1996**, *271*, 933.

[26] A. P. Alivisatos, *J. Phys. Chem.* **1996**, *100*, 13226–13239.

[27] V. Colvin, M. Schlamp, A. P. Alivisatos *et al.*, *Nature* **1994**, *370*, 354–357.

[28] R. Narayanan, M. A. El-Sayed, *J. Phys. Chem. B* **2005**, *109*, 12663–12676.

[29] M. Shao, T. Yu, J. H. Odell, M. Jin, Y. Xia, *Chem. Commun.* **2011**, *47*, 6566–6568.

[30] G. Collins, M. Schmidt, C. O'Dwyer, J. D. Holmes, G. P. McGlacken, *Angew. Chem. Int. Ed.* **2014**, *53*, 4142–4145.

[31] Y. Sun, Y. Xia, *Science* **2002**, *298*, 2176–2179.

[32] W. Niu, L. Zhang, G. Xu, *ACS Nano* **2010**, *4*, 1987–1996.

[33] Z. Niu, Q. Peng, M. Gong, H. Rong, Y. Li, *Angew. Chem. Int. Ed.* **2011**, *123*, 6439–6443.

[34] B. K. Park, S. Jeong, D. Kim, J. Moon, S. Lim, J. S. Kim, *J. Colloid Interface Sci.* **2007**, *311*, 417–424.

[35] X. Huang, S. Tang, H. Zhang, Z. Zhou, N. Zheng, *J. Am. Chem. Soc.* **2009**, *131*, 13916–13917.

[36] Y. Wang, S. Xie, J. Liu, J. Park, C. Z. Huang, Y. Xia, *Nano Lett.* **2013**, *13*, 2276–2281.

[37] A. Biswas, I. S. Bayer, A. S. Biris, T. Wang, E. Dervishi, F. Faupel, *Adv. Colloid Interface Sci.* **2012**, *170*, 2–27.

[38] B. Bhushan, *Encyclopedia of Nanotechnology*, Springer Dordrecht, Netherlands, **2012**.

[39] V. R. Manfrinato, L. Zhang, D. Su, H. Duan, R. G. Hobbs, E. A. Stach, K. K. Berggren, *Nano Lett.* **2013**, *13*, 1555–1558.

[40] M. Grzelczak, J. Pérez-Juste, P. Mulvaney, L. M. Liz-Marzán, *Chem. Soc. Rev.* **2008**, *37*, 1783–1791.

[41] A. R. Tao, S. Habas, P. Yang, *Small* **2008**, *4*, 310–325.

[42] R. B. Grubbs, *Polym. Rev.* **2007**, *47*, 197–215.

[43] S.-W. Kim, J. Park, Y. Jang, Y. Chung, S. Hwang, T. Hyeon, Y. W. Kim, *Nano Lett.* **2003**, *3*, 1289–1291.

[44] V. K. LaMer, R. H. Dinegar, *J. Am. Chem. Soc.* **1950**, *72*, 4847–4854.

[45] R. Viswanatha, D. Sarma, *Nanomat. Chem.* **2007**, *1*, 139–170.

[46] P. W. Voorhees, *J. Stat. Phys.* **1985**, *38*, 231–252.

[47] B. Derjaguin, *Prog. Surf. Sci.* **1993**, *43*, 1–14.

[48] E. J. W. Verwey, J. T. G. Overbeek, *J. Colloid Sci.* **1955**, *10*, 224–225.

[49] G. Trefalt, M. Borkovec, *Overview of DLVO theory*, **2014**.

[50] S. Rucareanu, M. Maccarini, J. L. Shepherd, R. B. Lennox, *J. Mater. Chem.* **2008**, *18*, 5830–5834.

[51] C. E. McCold, Q. Fu, S. Hihath, J.-M. Han, Y. Halfon, R. Faller, K. van Benthem, L. Zang, J. Hihath, *Mol. Syst. Des. Eng.* **2017**, *2*, 440–448.

[52] V. Mazumder, S. Sun, *J. Am. Chem. Soc.* **2009**, *131*, 4588–4589.

[53] A. Pontes da Costa, D. R. Nunes, M. Tharaud, J. Oble, G. Poli, J. Rieger, *ChemCatChem* **2017**, *9*, 2167–2175.

[54] S. Shi, L. Zhang, J. Zhu, W. Zhang, Z. Cheng, X. Zhu, *Polym. Lett.* **2009**, *3*, 401–412.

[55] P. Ahmadian Namini, A. Babaluo, B. Bayati, *J. Nanosci. Nanotechnol.* **2007**, *3*, 37–44.

[56] S. Ogasawara, S. Kato, *J. Am. Chem. Soc.* **2010**, *132*, 4608–4613.

[57] R. Narayanan, M. A. El-Sayed, *J. Am. Chem. Soc.* **2003**, *125*, 8340–8347.

[58] W. Niu, Z.-Y. Li, L. Shi, X. Liu, H. Li, S. Han, J. Chen, G. Xu, *Cryst. Growth Des.* **2008**, *8*, 4440–4444.

[59] M. Brust, M. Walker, D. Bethell, D. J. Schiffrin, R. Whyman, *J. Chem. Soc. Chem. Commun.* **1994**, *1*, 801–802.

[60] T. Teranishi, M. Miyake, *Chem. Mater.* **1998**, *10*, 594–600.

[61] Y. Sun, L. Zhang, H. Zhou, Y. Zhu, E. Sutter, Y. Ji, M. H. Rafailovich, J. C. Sokolov, *Chem. Mater.* **2007**, *19*, 2065–2070.

[62] J. Turkevich, P. C. Stevenson, J. Hillier, *Discuss. Faraday Soc.* **1951**, *11*, 55–75.

[63] G. Frens, *Colloid Polym. Sci.* **1972**, *250*, 736–741.

[64] G. Frens, *Nature* **1973**, *241*, 20–22.

[65] K. C. Grabar, R. G. Freeman, M. B. Hommer, M. J. Natan, *Anal. Chem.* **1995**, *67*, 735–743.

[66] J. Kimling, M. Maier, B. Okenve, V. Kotaidis, H. Ballot, A. Plech, *J. Phys. Chem. B* **2006**, *110*, 15700–15707.

[67] B. Ebeling, PhD thesis, Georg-August University Goettingen, **2015**.

[68] N. R. Jana, L. Gearheart, C. J. Murphy, *Langmuir* **2001**, *17*, 6782–6786.

[69] S. Link, M. A. El-Sayed, *J. Phys. Chem. B* **1999**, *103*, 4212–4217.

[70] J. E. Millstone, S. Park, K. L. Shuford, L. Qin, G. C. Schatz, C. A. Mirkin, *J. Am. Chem. Soc.* **2005**, *127*, 5312–5313.

[71] T. K. Sau, C. J. Murphy, *J. Am. Chem. Soc.* **2004**, *126*, 8648–8649.

[72] S. E. Skrabalak, J. Chen, Y. Sun, X. Lu, L. Au, C. M. Cobley, Y. Xia, *Acc. Chem. Res.* **2008**, *41*, 1587–1595.

[73] C. Loo, A. Lin, L. Hirsch, M.-H. Lee, J. Barton, N. Halas, J. West, R. Drezek, *Technol. Cancer Res. Treatm.* **2004**, *3*, 33–40.

[74] P. K. Jain, M. A. El-Sayed, *J. Phys. Chem. C* **2007**, *111*, 17451–17454.

[75] C. Li, K. L. Shuford, Q.-H. Park, W. Cai, Y. Li, E. J. Lee, S. O. Cho, *Angew. Chem. Int. Ed.* **2007**, *119*, 3328–3332.

[76] M. Liu, P. Guyot-Sionnest, *J. Phys. Chem. B* **2005**, *109*, 22192–22200.

[77] X. Huang, M. A. El-Sayed, *J. Adv. Res.* **2010**, *1*, 13–28.

[78] X. Ye, C. Zheng, J. Chen, Y. Gao, C. B. Murray, *Nano Lett.* **2013**, *13*, 765–771.

[79] P. K. Jain, M. A. El-Sayed, *Chem. Phys. Lett.* **2010**, *487*, 153–164.

[80] J. Becker, A. Trügler, A. Jakab, U. Hohenester, C. Sönnichsen, *Plasmonics* **2010**, *5*, 161–167.

[81] L. Vigderman, B. P. Khanal, E. R. Zubarev, *Adv. Mat.* **2012**, *24*, 4811–4841.

[82] C. J. Orendorff, C. J. Murphy, *J. Phys. Chem. B* **2006**, *110*, 3990–3994.

[83] K.-Q. Lin, J. Yi, S. Hu, B.-J. Liu, J.-Y. Liu, X. Wang, B. Ren, *J. Phys. Chem. C* **2016**, *120*, 20806–20813.

[84] R. S. Riley, E. S. Day, *Nanomed. Nanobiotechnol.* **2017**, *9*, e1449.

[85] J. Stone, S. Jackson, D. Wright, *Nanomed. Nanobiotechnol.* **2011**, *3*, 100–109.

[86] Y. Qiu, Y. Liu, L. Wang, L. Xu, R. Bai, Y. Ji, X. Wu, Y. Zhao, Y. Li, C. Chen, *Biomaterials* **2010**, *31*, 7606–7619.

[87] J. Song, X. Yang, O. Jacobson, P. Huang, X. Sun, L. Lin, X. Yan, G. Niu, Q. Ma, X. Chen, *Adv. Mat.* **2015**, *27*, 4910–4917.

[88] Z. Li, H. Huang, S. Tang, Y. Li, X.-F. Yu, H. Wang, P. Li, Z. Sun, H. Zhang, C. Liu *et al.*, *Biomat.* **2016**, *74*, 144–154.

[89] M. R. Ali, B. Snyder, M. A. El-Sayed, *Langmuir* **2012**, *28*, 9807–9815.

[90] N. R. Jana, L. Gearheart, C. J. Murphy, *J. Phys. Chem. B* **2001**, *105*, 4065–4067.

[91] S. K. Meena, M. Sulpizi, *Angew. Chem. Int. Ed.* **2016**, *128*, 12139–12143.

[92] D. Kolb, M. Przasnyski, H. Gerischer, *J. Electroanal. Chem. Interf. Electrochem.* **1974**, *54*, 25–38.

[93] E. Herrero, L. J. Buller, H. D. Abruña, *Chem. Rev.* **2001**, *101*, 1897–1930.

[94] C. Sanchez, M. Del Popolo, E. Leiva, *Surf. Sci.* **1999**, *421*, 59–72.

[95] M. Rojas, C. Sanchez, M. Del Pópolo, E. Leiva, *Surf. Sci.* **2000**, *453*, 225–228.

[96] C. E. Mortimer, U. Müller, *Chemie: Das Basiswissen der Chemie*, Georg Thieme Verlag, **2007**.

[97] H. Schmidbaur, S. Cronje, B. Djordjevic, O. Schuster, *Chem. Phys.* **2005**, *311*, 151–161.

[98] S. K. Ghosh, T. Pal, *Chem. Rev.* **2007**, *107*, 4797–4862.

[99] V. Amendola, R. Pilot, M. Frasconi, O. M. Maragò, M. A. Iatì, *J. Phys.: Condens. Matter* **2017**, *29*, 203002.

[100] G. Mie, *Anal. Phys.* **1908**, *330*, 377–445.

[101] S. Nie, S. R. Emory, *Science* **1997**, *275*, 1102–1106.

[102] A. M. Michaels, J. Jiang, L. Brus, *J. Phys. Chem. B* **2000**, *104*, 11965–11971.

[103] C. J. Orendorff, L. Gearheart, N. R. Jana, C. J. Murphy, *Phys. Chem. Chem. Phys.* **2006**, *8*, 165–170.

[104] G. C. Schatz, *Acc. Chem. Res.* **1984**, *17*, 370–376.

[105] S. S. Acimovic, M. P. Kreuzer, M. U. González, R. Quidant, *ACS Nano* **2009**, *3*, 1231–1237.

[106] K. Liu, A. Ahmed, S. Chung, K. Sugikawa, G. Wu, Z. Nie, R. Gordon, E. Kumacheva, *ACS Nano* **2013**, *7*, 5901–5910.

[107] A. Lee, A. Ahmed, D. P. dos Santos, N. Coombs, J. I. Park, R. Gordon, A. G. Brolo, E. Kumacheva, *J. Phys. Chem. C* **2012**, *116*, 5538–5545.

[108] C. Wang, J. Chen, T. Talavage, J. Irudayaraj, *Angew.* **2009**, *48*, 2759–2763.

[109] K. G. Thomas, S. Barazzouk, B. I. Ipe, S. S. Joseph, P. V. Kamat, *J. Phys. Chem. B* **2004**, *108*, 13066–13068.

[110] S. Shibu Joseph, B. I. Ipe, P. Pramod, K. G. Thomas, *J. Phys. Chem. B* **2006**, *110*, 150–157.

[111] P. K. Jain, W. Huang, M. A. El-Sayed, *Nano Lett.* **2007**, *7*, 2080–2088.

[112] P. K. Jain, M. A. El-Sayed, *Nano Lett.* **2008**, *8*, 4347–4352.

[113] P. K. Jain, S. Eustis, M. A. El-Sayed, *J. Phys. Chem. B* **2006**, *110*, 18243–18253.

[114] A. M. Funston, C. Novo, T. J. Davis, P. Mulvaney, *Nano Lett.* **2009**, *9*, 1651–1658.

[115] J. Aizpurua, G. W. Bryant, L. J. Richter, F. G. De Abajo, B. K. Kelley, T. Mallouk, *Phys. Rev. B* **2005**, *71*, 235420.

[116] C. Tabor, D. Van Haute, M. A. El-Sayed, *ACS Nano* **2009**, *3*, 3670–3678.

[117] W. Stöber, A. Fink, E. Bohn, *J. Colloid Interface Sci.* **1968**, *26*, 62–69.

[118] A. E. Danks, S. R. Hall, Z. Schnepp, *Mat. Horiz.* **2016**, *3*, 91–112.

[119] R. Narayan, U. Y. Nayak, A. M. Raichur, S. Garg, *Pharmaceutics* **2018**, *10*, 118.

[120] R. Burwell, *Pure Appl. Chem.* **1975**, *46*, 71–90.

[121] T. Asefa, Z. Tao, *Can. J. Chem.* **2012**, *90*, 1015–1031.

[122] J. Liang, Z. Liang, R. Zou, Y. Zhao, *Adv. Mat.* **2017**, *29*, 1701139.

[123] A. Mehmood, H. Ghafar, S. Yaqoob, U. F. Gohar, B. Ahmad, *J. Dev. Drugs* **2017**, *6*, 1–14.

[124] J. S. Beck, J. Vartuli, W. J. Roth, M. Leonowicz, C. Kresge, K. Schmitt, C. Chu, D. H. Olson, E. Sheppard, S. McCullen *et al.*, *J. Am. Chem. Soc.* **1992**, *114*, 10834–10843.

[125] Q. Huo, R. Leon, P. M. Petroff, G. D. Stucky, *Science* **1995**, *268*, 1324–1327.

[126] D. Zhao, J. Feng, Q. Huo, N. Melosh, G. H. Fredrickson, B. F. Chmelka, G. D. Stucky, *Science* **1998**, *279*, 548–552.

[127] K. Schumacher, P. I. Ravikovitch, A. Du Chesne, A. V. Neimark, K. K. Unger, *Langmuir* **2000**, *16*, 4648–4654.

[128] K. J. Edler, *Aust. J. Chem.* **2005**, *58*, 627–643.

[129] M. J. Hollamby, D. Borisova, P. Brown, J. Eastoe, I. Grillo, D. Shchukin, *Langmuir* **2012**, *28*, 4425–4433.

[130] Z. Yi, L. F. Dumée, C. J. Garvey, C. Feng, F. She, J. E. Rookes, S. Mudie, D. M. Cahill, L. Kong, *Langmuir* **2015**, *31*, 8478–8487.

[131] A. M. El-Toni, M. A. Ibrahim, J. P. Labis, A. Khan, M. Alhoshan, *Intern. J. Mol. Sci.* **2013**, *14*, 11496–11509.

[132] M. Bouchoucha, M.-F. Cote, R. C.-Gaudreault, M.-A. Fortin, F. Kleitz, *Chem. Mater.* **2016**, *28*, 4243–4258.

[133] K. Ma, U. Werner-Zwanziger, J. Zwanziger, U. Wiesner, *Chem. Mater.* **2013**, *25*, 677–691.

[134] N. A. Zainala, S. Shukor, H. A. A. Wabb, K. Razakb, *Chem. Engin.* **2013**, *32*, 2245–2250.

[135] J. Kim, L. Kim, C. Kim, *Biomacromolecules* **2007**, *8*, 215–222.

[136] Y.-D. Chiang, H.-Y. Lian, S.-Y. Leo, S.-G. Wang, Y. Yamauchi, K. C.-W. Wu, *J. Phys. Chem. C* **2011**, *115*, 13158–13165.

[137] H. Yamada, C. Urata, H. Ujiie, Y. Yamauchi, K. Kuroda, *Nanoscale* **2013**, *5*, 6145–6153.

[138] K. Moeller, J. Kobler, T. Bein, *Adv. Funct. Mater.* **2007**, *17*, 605–612.

[139] Z.-A. Qiao, L. Zhang, M. Guo, Y. Liu, Q. Huo, *Chem. Mater.* **2009**, *21*, 3823–3829.

[140] M. Vallet-Regi, A. Rámila, R. Del Real, J. Pérez-Pariente, *Chem. Mater.* **2001**, *13*, 308–311.

[141] K. Yano, Y. Fukushima, *J. Mater. Chem.* **2004**, *14*, 1579–1584.

[142] A. Ganguly, T. Ahmad, A. K. Ganguli, *Langmuir* **2010**, *26*, 14901–14908.

[143] K. Moeller, T. Bein, *Chem. Mater.* **2017**, *29*, 371–388.

[144] M. Huang, L. Liu, S. Wang, H. Zhu, D. Wu, Z. Yu, S. Zhou, *Langmuir* **2017**, *33*, 519–526.

[145] C. P. Mehnert, *Chem. Commun.* **1997**, *22*, 2215–2216.

[146] M. Semsarilar, S. Perrier, *Nature Chem.* **2010**, *2*, 811–820.

[147] M. H. Stenzel, T. P. Davis, *J. Polym. Sci. Part A: Polym. Chem.* **2002**, *40*, 4498–4512.

[148] J. F. Quinn, R. P. Chaplin, T. P. Davis, *J. Polym. Sci. Part A: Polym. Chem.* **2002**, *40*, 2956–2966.

[149] V. Coessens, J. Pyun, P. J. Miller, S. G. Gaynor, K. Matyjaszewski, *Macromol. Rapid Commun.* **2000**, *21*, 103–109.

[150] J. S. Wang, K. Matyjaszewski, *Macromolecules* **1995**, *28*, 7901–7910.

[151] C. Hawker, A. W. Bosman, E. Harth, *Chem. Rev.* **2001**, *101*, 3661–3688.

[152] J. Chiefari, Y. K. Chong, F. Ercole, J. Krstina, J. Jeffery, T. P. T. Le, R. T. A. Mayadunne, G. F. Meijs, C. L. Moad, G. Moad, E. Rizzardo, S. H. Thang, *Macromolecules* **1998**, *31*, 5559–5562.

[153] G. Moad, E. Rizzardo, S. H. Thang, *Aust. J. Chem.* **2012**, *65*, 985–1076.

[154] G. Moad, R. T. Mayadunne, E. Rizzardo, M. Skidmore, S. H. Thang, *Macromol. Symp.* **2003**, *192*, 1–12.

[155] G. Moad, E. Rizzardo, S. H. Thang, *Polym. Int.* **2011**, *60*, 9–25.

[156] P. Vana, *Lecture: Introduction in Macromolecular Chemistry*, Georg-August University Goettingen, **2014**.

[157] R. T. A. Mayadunne, E. Rizzardo, J. Chiefari, J. Krstina, G. Moad, A. Postma, S. H. Thang, *Macromolecules* **2000**, *33*, 243–245.

[158] C. Barner-Kowollik, M. Buback, B. Charleux, M. L. Coote, M. Drache, T. Fukuda, A. Goto, B. Klumperman, A. B. Lowe, J. B. Mcleary, G. Moad, M. J. Monteiro, R. D. Sanderson, M. P. Tonge, P. Vana, *J. Polym. Sci. Part A: Polym. Chem.* **2006**, *44*, 5809–5831.

[159] R. Bäßler, *Polymer Coatings-A Guide to Chemistry, Characterization, and Selected Applications*, John Wiley & Sons, **2020**.

[160] M. Husemann, M. Morrison, D. Benoit, J. Frommer, C. M. Mate, W. D. Hinsberg, J. L. Hedrick, C. J. Hawker, *J. Am. Chem. Soc.* **2000**, *122*, 1844–1845.

[161] M. Ramstedt, N. Cheng, O. Azzaroni, D. Mossialos, H. J. Mathieu, W. T. Huck, *Langmuir* **2007**, *23*, 3314–3321.

[162] X. Ye, X. Jiang, B. Yu, J. Yin, P. Vana, *Biomacromolecules* **2012**, *13*, 535–541.

[163] S. Schmidt, S. Alberti, P. Vana, G. J. Soler-Illia, O. Azzaroni, *Chem.–Eur. J.* **2017**, *23*, 14500–14506.

[164] M. Karg, N. Schelero, C. Oppel, M. Gradzielski, T. Hellweg, R. von Klitzing, *Chem. - Eur. J.* **2011**, *17*, 4648–4654.

[165] Q. Wei, J. Ji, J. Shen, *Macromol. Rapid Commun.* **2008**, *29*, 645–650.

[166] H. Häkkinen, *Nat. Chem.* **2012**, *4*, 443.

[167] S. Slavin, A. H. Soeriyadi, L. Voorhaar, M. R. Whittaker, C. R. Becer, C. Boyer, T. P. Davis, D. M. Haddleton, *Soft Matter* **2012**, *8*, 118–128.

[168] L. Wu, U. Glebe, A. Böker, *Polym. Chem.* **2015**, *6*, 5143–5184.

[169] S. P. Pujari, L. Scheres, A. T. Marcelis, H. Zuilhof, *Angew. Chem. Int. Ed.* **2014**, *53*, 6322–6356.

[170] C. Rossner, PhD thesis, Goerg-August University Goettingen, **2016**.

[171] K. Ohno, K.-m. Koh, Y. Tsujii, T. Fukuda, *Macromolecules* **2002**, *35*, 8989–8993.

[172] K. Ohno, K. Koh, Y. Tsujii, T. Fukuda, *Angew. Chem. Int. Ed.* **2003**, *42*, 2751–2754.

[173] C. Barner-Kowollik, *Handbook of RAFT Polymerization*, John Wiley & Sons, **2008**.

[174] K. Hendrich, PhD thesis, Goerg-August University Goettingen, **2020**.

[175] K. Zhang, H. Chen, X. Chen, Z. Chen, Z. Cui, B. Yang, *Macromol. Mater. Eng.* **2003**, *288*, 380–385.

[176] Y. Maeda, T. Nakamura, I. Ikeda, *Macromolecules* **2002**, *35*, 217–222.

[177] H. G. Schild, D. A. Tirrell, *J. Phys. Chem.* **1990**, *94*, 4352–4356.

[178] M. Heskins, J. E. Guillet, *J. Macromol. Sci. - Chem.* **1968**, *2*, 1441–1455.

[179] E. I. Tiktopulo, V. N. Uversky, V. B. Lushchik, S. I. Klenin, V. E. Bychkova, O. B. Ptitsyn, *Macromolecules* **1995**, *28*, 7519–7524.

[180] J. Hu, H. Meng, G. Li, S. I. Ibekwe, *Smart Mater. Struct.* **2012**, *21*, 053001.

[181] M. R. Islam, Z. Lu, X. Li, A. K. Sarker, L. Hu, P. Choi, X. Li, N. Hakobyan, M. J. Serpe, *Anal. Chim. Acta* **2013**, *789*, 17–32.

[182] S. Ohya, Y. Nakayama, T. Matsuda, *Biomacromolecules* **2001**, *2*, 856–863.

[183] Y. Akiyama, A. Kikuchi, M. Yamato, T. Okano, *Langmuir* **2004**, *20*, 5506–5511.

[184] J. Liu, C. Detrembleur, M.-C. De Pauw-Gillet, S. Mornet, E. Duguet, C. Jérôme, *Polym. Chem.* **2014**, *5*, 799–813.

[185] H.-L. Wang, L.-Y. Liu, W.-Q. Kou, W.-F. Jiang, *Polym. Compos.* **2013**, *34*, 681–689.

[186] M. M. W. Muscatello, S. A. Asher, *Adv. Funct. Mater.* **2008**, *18*, 1186–1193.

[187] P. W. Atkins, J. De Paula, *Physikalische Chemie*, *Vol. 5*, John Wiley & Sons, **2013**.

[188] H. G. Schild, *Prog. Polym. Sci.* **1992**, *17*, 163–249.

[189] Y. Okada, F. Tanaka, *Macromolecules* **2005**, *38*, 4465–4471.

[190] Y. Zhang, S. Furyk, L. B. Sagle, Y. Cho, D. E. Bergbreiter, P. S. Cremer, *J. Phys. Chem. C* **2007**, *111*, 8916–8924.

[191] M. L. Ohnsorg, J. M. Ting, S. D. Jones, S. Jung, F. S. Bates, T. M. Reineke, *Polym. Chem.* **2019**, *10*, 3469–3479.

[192] R. Plummer, D. J. Hill, A. K. Whittaker, *Macromolecules* **2006**, *39*, 8379–8388.

[193] F. Eeckman, A. J. Moës, K. Amighi, *Eur. Polym. J.* **2004**, *40*, 873–881.

[194] F. Hofmeister, *Archiv für experimentelle Pathologie und Pharmakologie* **1888**, *24*, 247–260.

[195] Y. Zhang, S. Furyk, D. E. Bergbreiter, P. S. Cremer, *J. Am. Chem. Soc.* **2005**, *127*, 14505–14510.

[196] D. Rohleder, P. Vana, *RSC Adv.* **2020**, *10*, 26504–26507.

[197] J. R. Ludwig, C. S. Schindler, *Chem.* **2017**, *2*, 313–316.

[198] K. Nakajima, I. Daigo, K. Nansai, K. Matsubae, W. Takayanagi, M. Tomita, Y. Matsuno, *Resour. Conserv. Recycl.* **2018**, *133*, 369–374.

[199] O. Vidal, F. Rostom, C. François, G. Giraud, *Elements* **2017**, *13*, 319–324.

[200] T. W. Lyons, M. S. Sanford, *Chem. Rev.* **2010**, *110*, 1147–1169.

[201] L. Yin, J. Liebscher, *Chem. Rev.* **2007**, *107*, 133–173.

[202] L. Ackermann, *Chem. Rev.* **2011**, *111*, 1315–1345.

[203] I. Papagiannouli, M. Demetriou, T. Krasia-Christoforou, S. Couris, *RSC Adv.* **2014**, *4*, 8779–8788.

[204] S. Shi, L. Zhang, J. Zhu, W. Zhang, Z. Cheng, X. Zhu, *Express Polym. Lett.* **2009**, *3*, 401–412.

[205] M. T. Reetz, E. Westermann, *Angew. Chem. Int. Ed.* **2000**, *39*, 165–168.

[206] I. P. Beletskaya, A. N. Kashin, A. E. Litvinov, V. S. Tyurin, P. M. Valetsky, G. van Koten, *Organometallics* **2006**, *25*, 154–158.

[207] A. Biffis, P. Centomo, A. Del Zotto, M. Zecca, *Chem. Rev.* **2018**, *118*, 2249–2295.

[208] R. J. Kalbasi, M. Negahdari, *J. Mol. Struct.* **2014**, *1063*, 259–268.

[209] C. P. Mehnert, D. W. Weaver, J. Y. Ying, *J. Am. Chem. Soc.* **1998**, *120*, 12289–12296.

[210] C. J. Johnson, E. Dujardin, S. A. Davis, C. J. Murphy, S. Mann, *J. Mater. Chem.* **2002**, *12*, 1765–1770.

[211] D. Nepal, K. Park, R. A. Vaia, *Small* **2012**, *8*, 1013–1020.

[212] A. Indrasekara, R. C. Wadams, L. Fabris, *Part. Part. Syst. Charact.* **2014**, *31*, 819–838.

[213] V. Raeesi, L. Y. Chou, W. C. Chan, *Adv. Mat.* **2016**, *28*, 8511–8518.

[214] J. W. Hotchkiss, B. G. Mohr, S. G. Boyes, *J. Nanopart. Res.* **2010**, *12*, 915–930.

[215] I. Gorelikov, N. Matsuura, *Nano Lett.* **2008**, *8*, 369–373.

[216] C. Graf, D. L. Vossen, A. Imhof, A. van Blaaderen, *Langmuir* **2003**, *19*, 6693–6700.

[217] Y. Chen, H.-R. Chen, J.-L. Shi, *Acc. Chem. Res.* **2014**, *47*, 125–137.

[218] J. Chen, S. K. Spear, J. G. Huddleston, R. D. Rogers, *Green Chem.* **2005**, *7*, 64–82.

[219] D. E. Bergbreiter, J. Tian, C. Hongfa, *Chem. Rev.* **2009**, *109*, 530–582.

[220] N. R. Candeias, L. C. Branco, P. M. P. Gois, C. A. Afonso, A. F. Trindade, *Chem. Rev.* **2009**, *109*, 2703–2802.

[221] M. Vafaeezadeh, M. M. Hashemi, *J. Mol. Liq.* **2015**, *207*, 73–79.

[222] C. Luo, Y. Zhang, Y. Wang, *J. Mol. Catal. A: Chem.* **2005**, *229*, 7–12.

[223] L. Ackermann, R. Vicente, *Org. Lett.* **2009**, *11*, 4922–4925.

[224] R. F. Heck, J. Nolley Jr, *J. Org. Chem.* **1972**, *37*, 2320–2322.

[225] B. G. Pollet, S. S. Kocha, I. Staffell, *Curr. Opin. Electrochem.* **2019**, *16*, 90–95.

[226] V. Vogl, M. Åhman, L. J. Nilsson, *Climate Policy* **2021**, *21*, 78–92.

[227] S. K. Konda, A. Chen, *Materials Today* **2016**, *19*, 100–108.

[228] W. Hennings, S. Mischinger, J. Linssen, *Ener. Pol.* **2013**, *62*, 139–144.

[229] U. Eberle, M. Felderhoff, F. Schueth, *Angew. Chem. Int. Ed.* **2009**, *48*, 6608–6630.

[230] L. Schlapbach, *Nature* **2009**, *460*, 809–811.

[231] S. Dekura, H. Kobayashi, K. Kusada, H. Kitagawa, *ChemPhysChem* **2019**, *20*, 1158–1176.

[232] G. Li, H. Kobayashi, S. Dekura, R. Ikeda, Y. Kubota, K. Kato, M. Takata, T. Yamamoto, S. Matsumura, H. Kitagawa, *J. Am. Chem. Soc.* **2014**, *136*, 10222–10225.

[233] C. Lebouin, Y. Soldo, S. Grigoriev, M. Guymont, P. Millet, *Int. J. Hydrogen Energy* **2013**, *38*, 966–972.

[234] M. Yamauchi, R. Ikeda, H. Kitagawa, M. Takata, *J. Phys.Chem. C* **2008**, *112*, 3294–3299.

[235] S. Wagner, A. Pundt, *Int. J. Hydrogen Energy* **2016**, *41*, 2727–2738.

[236] S. Wagner, A. Pundt, *AIMS Mater. Sci.* **2020**, *7*, 399–419.

[237] A. Carson, F. Lewis, *Trans. Faraday Soc.* **1967**, *63*, 1453–1457.

[238] H. Noh, W. Luo, T. B. Flanagan, *J. Alloys Compd.* **1993**, *196*, 7–16.

[239] T. Kubota, Y. Kitajima, K. Asakura, Y. Iwasawa, *Bull. Chem. Soc. Jpn.* **1999**, *72*, 673–681.

[240] W. P. Zhou, A. Lewera, R. Larsen, R. I. Masel, P. S. Bagus, A. Wieckowski, *J. Phys. Chem. B* **2006**, *110*, 13393–13398.

[241] T. C. Narayan, F. Hayee, A. Baldi, A. L. Koh, R. Sinclair, J. A. Dionne, *Nat. Commun.* **2017**, *8*, 1–8.

[242] X. Zhang, J. Meng, B. Zhu, J. Yu, S. Zou, Z. Zhang, Y. Gao, Y. Wang, *Chem. Commun.* **2017**, *53*, 13213–13216.

[243] W. Peng, MSc thesis, Goerg-August University Goettingen, **2015**.

[244] H. Ko, S. Singamaneni, V. V. Tsukruk, *Small* **2008**, *4*, 1576–1599.

[245] K. Liu, N. Zhao, E. Kumacheva, *Chem. Soc. Rev.* **2011**, *40*, 656–671.

[246] M. J. Hore, R. J. Composto, *ACS Nano* **2010**, *4*, 6941–6949.

[247] S. K. Ocal, J. Patarroyo, N. B. Kiremitler, S. Pekdemir, V. F. Puntes, M. S. Onses, *J. Colloid Interface Sci.* **2018**, *532*, 449–455.

[248] H. J. Kim, W. Wang, W. Bu, M. M. Hossen, A. Londoño-Calderon, A. C. Hillier, T. Prozorov, S. Mallapragada, D. Vaknin, *Sci. Rep.* **2019**, *9*, 1–9.

[249] N. R. Jana, *Small* **2005**, *1*, 875–882.

[250] S. Eustis, M. El-Sayed, *J. Phys. Chem. B* **2005**, *109*, 16350–16356.

[251] T. Kawano, Y. Niidome, T. Mori, Y. Katayama, T. Niidome, *Bioconjug. Chem.* **2009**, *20*, 209–212.

[252] A. Shiotani, Y. Akiyama, T. Kawano, Y. Niidome, T. Mori, Y. Katayama, T. Niidome, *Bioconjug. Chem.* **2010**, *21*, 2049–2054.

[253] C. Barner-Kowollik, T. P. Davis, M. H. Stenzel, *Aust. J. Chem.* **2006**, *59*, 719–727.

[254] D. Boschmann, R. Edam, P. J. Schoenmakers, P. Vana, *Polymer* **2008**, *49*, 5199–5208.

[255] D. Boschmann, PhD thesis, Georg-August University Goettingen, **2008**.

[256] E. Kryachko, F. Remacle, *Nano Lett.* **2005**, *5*, 735–739.

[257] Z. Nie, D. Fava, E. Kumacheva, S. Zou, G. C. Walker, M. Rubinstein, *Nat. Mater.* **2007**, *6*, 609–614.

[258] L. Wang, Y. Zhu, L. Xu, W. Chen, H. Kuang, L. Liu, A. Agarwal, C. Xu, N. A. Kotov, *Angew.* **2010**, *49*, 5472–5475.

[259] A. Einstein, *Ann. d. Phys* **1905**, *111*, 5020–5025.

[260] J. Rodríguez-Fernández, J. Pérez-Juste, L. M. Liz-Marzán, P. R. Lang, *J. Phys. Chem. C* **2007**, *111*, 5020–5025.

[261] B. M. van der Zande, J. K. Dhont, M. R. Böhmer, A. P. Philipse, *Langmuir* **2000**, *16*, 459–464.

[262] H. Liu, N. Pierre-Pierre, Q. Huo, *Gold Bull.* **2012**, *45*, 187–195.

[263] L. Shao, K. C. Woo, H. Chen, Z. Jin, J. Wang, H.-Q. Lin, *ACS Nano* **2010**, *4*, 3053–3062.

[264] S. Pierrat, I. Zins, A. Breivogel, C. Sönnichsen, *Nano Lett.* **2007**, *7*, 259–263.

[265] Z. Fan, M. Tebbe, A. Fery, S. Agarwal, A. Greiner, *Part. Part. Syst. Charact.* **2016**, *33*, 698–702.

[266] L. M. Liz-Marzán, M. Giersig, P. Mulvaney, *Langmuir* **1996**, *12*, 4329–4335.

[267] D. Rohleder, P. Vana, *Biomacromolecules* **2021**, *22*, 1614–1624.

[268] J. Fang, H. Nakamura, H. Maeda, *Adv. Drug Delivery Rev.* **2011**, *63*, 136–151.

[269] H. S. Choi, W. Liu, P. Misra, E. Tanaka, J. P. Zimmer, B. I. Ipe, M. G. Bawendi, J. V. Frangioni, *Nat. B* **2007**, *25*, 1165–1170.

[270] M. Longmire, P. L. Choyke, H. Kobayashi, *Nanomedicine* **2008**, *3*, 703–717.

[271] Y. Matsumura, H. Maeda, *Cancer Res.* **1986**, *46*, 6387–6392.

[272] H. Maeda, *Adv. Enzyme Regul.* **2001**, *pp.*, 189–207.

[273] H. Maeda, J. Wu, T. Sawa, Y. Matsumura, K. Hori, *J. Controlled Release* **2000**, *65*, 271–284.

[274] S.-D. Li, L. Huang, *Mol. Pharm.* **2008**, *5*, 496–504.

[275] Q. Zhang, N. Iwakuma, P. Sharma, B. Moudgil, C. Wu, J. McNeill, H. Jiang, S. Grobmyer, *Nanotechnology* **2009**, *20*, 395102.

[276] M. Zhou, R. Zhang, M. Huang, W. Lu, S. Song, M. P. Melancon, M. Tian, D. Liang, C. Li, *J. Am. Chem. Soc.* **2010**, *132*, 15351–15358.

[277] D. Kim, S. Park, J. H. Lee, Y. Y. Jeong, S. Jon, *J. Am. Chem. Soc.* **2007**, *129*, 7661–7665.

[278] S. D. Perrault, C. Walkey, T. Jennings, H. C. Fischer, W. C. Chan, *Nano Lett.* **2009**, *9*, 1909–1915.

[279] W.-S. Cho, M. Cho, J. Jeong, M. Choi, H.-Y. Cho, B. S. Han, S. H. Kim, H. O. Kim, Y. T. Lim, B. H. Chung *et al.*, *Toxicol. Appl. Pharmacol.* **2009**, *236*, 16–24.

[280] F. Tatini, I. Landini, F. Scaletti, L. Massai, S. Centi, F. Ratto, S. Nobili, G. Romano, F. Fusi, L. Messori *et al.*, *J. Mat. Chem. B* **2014**, *2*, 6072–6080.

[281] T. Ishida, H. Kiwada, *Int. J. Pharm.* **2008**, *354*, 56–62.

[282] L. Y. Chou, F. Song, W. C. Chan, *J. Am. Chem. Soc.* **2016**, *138*, 4565–4572.

[283] S. Ohta, D. Glancy, W. C. Chan, *Science* **2016**, *351*, 841–845.

[284] L. C. Kennedy, L. R. Bickford, N. A. Lewinski, A. J. Coughlin, Y. Hu, E. S. Day, J. L. West, R. A. Drezek, *Small* **2011**, *7*, 169–183.

[285] A. M. Smith, M. C. Mancini, S. Nie, *Nat. Nanotechnol.* **2009**, *4*, 710.

[286] X. Huang, I. H. El-Sayed, W. Qian, M. A. El-Sayed, *J. Am. Chem. Soc.* **2006**, *128*, 2115–2120.

[287] C. Rossner, O. Glatter, O. Saldanha, S. Koester, P. Vana, *Langmuir* **2015**, *31*, 10573–10582.

[288] Y. Zhang, S. Furyk, L. B. Sagle, Y. Cho, D. E. Bergbreiter, P. S. Cremer, *J. Phys. Chem. C* **2007**, *111*, 8916–8924.

[289] A. Nykänen, M. Nuopponen, P. Hiekkataipale, S.-P. Hirvonen, A. Soininen, H. Tenhu, O. Ikkala, R. Mezzenga, J. Ruokolainen, *Macromolecules* **2008**, *41*, 3243–3249.

[290] M. Philipp, V. Körstgens, D. Magerl, C. Heller, Y. Yao, W. Wang, G. Santoro, S. V. Roth, P. Müller-Buschbaum, *Langmuir* **2015**, *31*, 9619–9627.

[291] J. W. Hotchkiss, A. B. Lowe, S. G. Boyes, *Chem. Mater.* **2007**, *19*, 6–13.

[292] S. T. Jones, Z. Walsh-Korb, S. J. Barrow, S. L. Henderson, J. del Barrio, O. A. Scherman, *ACS Nano* **2016**, *10*, 3158–3165.

[293] S. Sugio, A. Kashima, S. Mochizuki, M. Noda, K. Kobayashi, *Protein Eng.* **1999**, *12*, 439–446.

[294] S. N. Krylov, N. J. Dovichi, *Anal. Chem.* **2000**, *72*, 111–128.

[295] W. W. Quigley, N. J. Dovichi, *Anal. Chem.* **2004**, *76*, 4645–4658.

[296] S. Ge, K. Kojio, A. Takahara, T. Kajiyama, *J. Biomater. Sci. Polym. Ed.* **1998**, *9*, 131–150.

[297] N. Nezafati, F. Moztarzadeh, S. Hesaraki, *Biotechnol. Bioprocess Eng.* **2012**, *17*, 746–754.

[298] Y. Hiruta, Y. Nagumo, Y. Suzuki, T. Funatsu, Y. Ishikawa, H. Kanazawa, *Colloids Surf. B* **2015**, *132*, 299–304.

[299] C. Fang, L. Liu, J. Weng, S. Zhang, X. Zhang, Z. Ren, Y. Shen, F. Meng, B. Zheng, S. Li *et al.*, *Angew. Chem. Int. Ed.* **2021**, *60*, 976–982.

[300] C. Martínez, A. Corma, *Coord. Chem. Rev.* **2011**, *255*, 1558–1580.

[301] Q.-R. Fang, D.-Q. Yuan, J. Sculley, J.-R. Li, Z.-B. Han, H.-C. Zhou, *Inorg. Chem.* **2010**, *49*, 11637–11642.

[302] W. Zhang, G. Lu, C. Cui, Y. Liu, S. Li, W. Yan, C. Xing, Y. R. Chi, Y. Yang, F. Huo, *Adv. Mat.* **2014**, *26*, 4056–4060.

[303] Z. Yin, Q. Zheng, *Adv. Energy Mater.* **2012**, *2*, 179–218.

[304] G. Kaur, R. Adhikari, P. Cass, M. Bown, P. Gunatillake, *RSC Adv.* **2015**, *5*, 37553–37567.

[305] X. Yu, K. Xiao, J. Chen, N. V. Lavrik, K. Hong, B. G. Sumpter, D. B. Geohegan, *ACS Nano* **2011**, *5*, 3559–3567.

[306] S. Roth, H. Bleier, W. Pukacki, *Faraday Discuss. Chem. Soc.* **1989**, *88*, 223–233.

[307] L. Zhai, R. D. McCullough, *J. Mater. Chem.* **2004**, *14*, 141–143.

[308] M. C. Iovu, C. Rockford Craley, M. Jeffries-El, A. B. Krankowski, R. Zhang, *Macromolecules* **2007**, *40*, 4733–4735.

[309] A. Britze, V. Möllmann, G. Grundmeier, H. Luftmann, D. Kuckling, *Macromol. Chem. Phys.* **2011**, *212*, 679–690.

10 Appendix

10.1 Abbreviations

9-BBN 9-borabicyclo(3.3.1)nonane

A absorbance

α dipolar polarizability

AA acrylic acid

AAM acrylamide

AIBN 1,1'-azobis(isobutyronitrile)

ALD atomic layer deposition

AR aspect ratio

ATRP atom transfer radical polymerization

AuNP gold nanoparticle

AuNR gold nanorod

BSA bovine serum albumin

c velocity of light

C_0 saturation concentration within the nucleation process

$C_{\mathbf{S}}$ saturation concentration after the Oswald ripening

CCD charge-coupled device

CSIRO *Commonwealth Scientific and Industrial Research Organisation*

CTA chain transfer agent

CTAB cetyltrimethylammoniumbromide

CTAC cetyltrimethylammoniumchloride

CTATOS cetyltrimethylammoniumtosylate

D physical size of a nanoparticle

d doublet

$d_{\mathbf{hydro}}$ hydrodynamic diameter

$d_{\mathbf{p\text{-}p}}$ interparticle distance of adjacent particle cores

$d_{\mathbf{rot}}$ pseudo rotational, hydrodynamic diameter

$d_{\mathbf{trans}}$ translational, hydrodynamic diameter

δ chemical shift in NMR spectroscopy

$\boldsymbol{Đ}$ dispersity

DDA discrete dipole approximation

DL double layer

DLS dynamic light scattering

DLVO Derjaguin, Landau, Verwey, Overbeek

DMAc *N,N*-dimethylacetamide

DMF dimetylformamide

DMSO dimethylsulfoxide

DP degree of polymerization

dppp 1,3-bis(diphenylphosphino)propane

$\vec{E}$ electric field

$\vec{E_0}$	electric field amplitude
ε_0	dielectric constant in vacuum
$\varepsilon_{\mathbf{m}}$	dielectric constant of a surrounding medium
$E_{\mathbf{NF}}$	electric near-field
$E_{\mathbf{p}}$	induced electric field inside a nanoparticle
$\varepsilon_{\mathbf{p}}$	dielectric constant of a particle
$\varepsilon_{\mathbf{p,\ i}}$	imaginary dielectric constant of a nanoparticle
$\varepsilon_{\mathbf{p,\ r}}$	real dielectric constant of a nanoparticle
EELS	electron energy loss spectroscopy
EPR	enhanced permeability and retention
eq.	equivalent
ETEM	environmental transmission electron microscope
EtOH	ethanol
et al.	*et alii* (and others)
etc.	*et cetera* (and so on)
fcc	face-centered cubic
Fig.	figure
FRP	free radical polymerization
g	gravitational force
γ	inelastic collision frequency of electrons
$\Delta G_{\mathbf{mix}}$	free mixing enthalpy
$\Delta H_{\mathbf{mix}}$	mixing enthalpy

HPLC	high performance liquid chromatography
HSA	human serum albumin
$\mathbf{I^{\bullet}}$	initiator fragment
$\mathbf{I_2}$	initiator
ICP-MS	inductively coupled plasma mass spectrometry
IR	infrared
J	coupling constant (NMR)
k	observed polymer length per molar mass
κ	shape factor for nanoparticle polarizability
$k_{\mathbf{theo}}$	theoretical polymer length per molar mass
KIT	Karlsruhe Institute of Technology
l	measure for the extent of elongation of a polymer brush
λ	wavelength
$\lambda_{\mathbf{long}}$	wavelength of the longitidunal LSPR of AuNRs
$\lambda_{\mathbf{LSPR}}$	wavelength of the LSPR of an isolated metal nanoparticle
$\Delta\lambda_{\mathbf{LSPR}}$	wavelength shift of coupled metal nanoparticles
$\lambda_{\mathbf{trans}}$	wavelength of the transverse LSPR of AuNRs
LCST	lower critical solution temperature
LSPR	localized surface plasmon resonance
M	monomer
M	molar mass
[**M**]	monomer concentration

m	multiplett
m	mass
$m_{\mathbf{e}}$	mass of an electron
$\mu_{\mathbf{ads}}$	chemical potential of an adsorbate metal
$\mu_{\mathbf{bulk}}$	chemical potential of a bulk metal
$M_{\mathbf{M}}$	molecular weight of the monomer
M_n	avarage molecular weight
$M_{n,\mathbf{theo}}$	theoretical, average molecular weight of a RAFT-polymerization
$M_{\mathbf{RAFT}}$	molecular weight of a RAFT-agent
MA	methyl acrylate
MCM-41	Mobil Composition of Matter No. 41
MeCN	acetonitrile
MeOH	methanol
MOF	metal–organic framework
MS	mass spectrometry
m**Si**	mesoporous silica
m/z	mass-per-charge ratio
n	amount of a substance
N	electron density
ν	frequency
$\nu_{\mathbf{plasma}}$	plasma frequency
NC	nanocrystal

NCube nanocube

NIPAM *N*-isopropyl acrylamide

NIR near-infrared

NMP nitroxide-mediated polymerization

NMR nuclear magnetic resonance

NP nanoparticle

NR nanorod

OAm oleylamine

Φ work function

$\mathbf{P_m^\bullet}$ short-chain, polymeric radical

$\mathbf{P_n^\bullet}$ long-chain, polymeric radical

P3HT poly(3-hexylthiophene)

PBS phosphate buffer solution

PE polyethylene

pH *potentia hydrogenii*

PEG poly(ethylene glycol)

PMA poly(methyl acrylate)

PMMA poly(methyl methacrylate)

PP polypropylene

ppm parts per million

PS polystyrene

PSPP propagating surface plasmon polaritions

PTFE polytetrafluoroethylene

PTT photothermal therapy

PVCL poly(*N*-vinylcaprolactam)

PVME poly(vinyl methyl ether)

PVP poly(*N*-vinylpyrrolidone)

q quartet

R nanoparticle radius

$\mathbf{R^{\bullet}}$ propagating radical in RDRP

r^* critical radius in the *LaMer–Dinegar* model

$r_{\mathbf{p\text{-}p}}$ Surface-to-surface distance of particles in DLVO-theory

R-group leaving group of a RAFT-agent

RAFT reversible addition-fragmentation chain-transfer

[**RAFT**] RAFT-agent concentration

RDRP reversible-deactivation radical polymerization

RI refractive index

r.u. repeating unit

s singlet

s spacing between two nanoparticles

$\sigma_{\mathbf{ext}}$ extinction cross-section

$\Delta S_{\mathbf{mix}}$ mixing entropy

SAED selected area electron diffraction

SAXS small-angle X-ray scattering

SBF	simulated blood fluid
SEC	size-exclusion chromatography
T	temperature
t	triplet
t	time
θ	orientation angle between two nanorods
τ	exponential coupling decay length of a nanoparticle dimer
$\tau_{\mathbf{rot}}$	rotational diffusion-time
$T_{\mathbf{cloud}}$	cloud point temperature
$T_{\mathbf{LCST}}$	lower critical solution temperature
Tab.	table
TMOS	tetramethyl ortho silicate
TEA	triethanolamine
TEM	transmission electron microscopy
TEOS	tetraethyl ortho silicate
TERS	tip-enhanced Raman spectroscopy
TGA	thermogravimetric analysis
THF	tetrahydrofuran
TOAB	tetraoctylammonium bromide
TTC	trithiocarbonate
UCST	upper critical solution temperature
UPD	underpotential deposition

$\Delta U_{\mathbf{p}}$	underpotential deposition shift
UV	ultraviolet
vis	visible
vs.	versus
XANES	X-ray absorption near-edge structure spectroscopy
XPS	X-ray photoelectron spectroscopy
Y•	persistent radical in RDRP
z	electric charge
Z-group	stabilizing group of a RAFT-agent

10.2 Units

°	degrees
°C	degrees Celsius
Å	Ångström
g	gram
h	hours
Hz	Hertz
J	Joule
K	Kelvin
L	liter
m	meter
min	minutes
mol	mole
Ω	Ohm
Pa	Pascal
s	seconds
W	Watt

11 Acknowledgements

Aller erst möchte ich Prof. Dr. Philipp Vana danken, an diesem äußerst interessanten Thema geforscht haben zu dürfen und dass er mir stets die Möglichkeit gab, meine eigenen Ideen und Ziele einbringen zu können. Außerdem möchte ich ihm für die herausragende Betreuung über die gesamte Studienzeit angefangen von der Bachelor- über die Masterarbeit hinzu der Promotion danken und vor allem auch für die Vermittlung an die Clarkson University zu Prof. Dr. Devon Shipp. Die Erfahrungen, die ich so im Ausland sammeln konnte, haben mich sowohl als Wissenschaftler aber auch als Mensch weiterentwickelt.

Außerdem möchte ich Prof. Dr. Alec Wodtke für die Übernahme des Co-Referats dieser Arbeit und die hilfreichen Tipps und Anregungen danken, die ich in den *Thesis Committee Meetings* erhalten habe.

Prof. Dr. Michael Buback, Prof. Dr. Burkhard Geil, Prof. Dr. Thomas Zeuch, und Prof. Dr. Dietmar Stalke möchte ich meinen Dank als Mitglieder der Prüfungskommission aussprechen.

Für die technische Unterstützung am TEM möchte ich mich bei Matthias Hahn bedanken, der jederzeit ein offenes Ohr für aufkommende Probleme hatte. Außerdem danke ich den Werkstätten für Elektronik und Feinmechanik und dabei besonders Reinhard Hildebrandt und Andreas Knorr für den perfekte Umsetzung meiner Vorstellung bezüglich des Baus des Licht-induzierten Heizgeräts. Für die ICP-MS Messungen möchte ich mich bei Prof. Dr. Willbold und Dr. Hoffmann aus der Isotopengeologie Abteilung bedanken. Zudem danke ich Torsten Fornefeld für die Aufnahme der AFM Bilder und Stella Weber für die Durchführung der Wasser-GPC Analysen.

Dann möchte ich mich noch für die herausragende Arbeitsatmosphäre im Büro bei Enno Meyer, Annika Nitschke und Stella Weber und im gesamten

Arbeitskreis bei allen aktuellen und ehemaligen Mitglieder der MMC-Gruppe bedanken, mit denen ich eine großartige Zeit während meiner Promotion verbracht habe. In diesem Zuge möchte ich auch meiner Bachelorstudentin Valentina Andreevna Giniatoulline Moya für die tolle Zusammenarbeit während ihrer Abschlussarbeit danken, in der wir beide viel lernen konnten.

Mein aller größter Dank geht an meine Freundin Stella für ihre Liebe, den Spaß, den wir zusammen haben und vor allem für ihre riesige Geduld. Sie ist mein Ruhepol und hat es auch in frustrierenden Zeiten auf der Arbeit immer wieder geschafft mich aufzubauen.

Am Ende möchte ich noch meinen Eltern und meiner Schwester Tabea danken, die mich stets in all meinen Vorhaben unterstützen und mir so die Sicherheit geben meine Ziele verfolgen zu können. Ohne sie wäre das Studium und die Promotion nicht zu bewältigen gewesen.